



Calhoun: The NPS Institutional Archive
DSpace Repository

Theses and Dissertations

1. Thesis and Dissertation Collection, all items

2021-06

**ORIENTATION DEPENDENT MECHANICAL
PROPERTIES OF 3D PRINTED POLYMER
MATRIX COMPOSITES**

Hodgkins, Charles L.

Monterey, CA; Naval Postgraduate School

<http://hdl.handle.net/10945/67739>

This publication is a work of the U.S. Government as defined in Title 17, United States Code, Section 101. Copyright protection is not available for this work in the United States.

Downloaded from NPS Archive: Calhoun



Calhoun is the Naval Postgraduate School's public access digital repository for research materials and institutional publications created by the NPS community. Calhoun is named for Professor of Mathematics Guy K. Calhoun, NPS's first appointed -- and published -- scholarly author.

Dudley Knox Library / Naval Postgraduate School
411 Dyer Road / 1 University Circle
Monterey, California USA 93943

<http://www.nps.edu/library>



**NAVAL
POSTGRADUATE
SCHOOL**

MONTEREY, CALIFORNIA

THESIS

**ORIENTATION DEPENDENT MECHANICAL
PROPERTIES OF 3D PRINTED POLYMER MATRIX
COMPOSITES**

by

Charles L. Hodgkins

June 2021

Thesis Advisor:
Co-Advisor:

Andy Nieto
Young W. Kwon

Approved for public release. Distribution is unlimited.

THIS PAGE INTENTIONALLY LEFT BLANK

REPORT DOCUMENTATION PAGE			<i>Form Approved OMB No. 0704-0188</i>
Public reporting burden for this collection of information is estimated to average 1 hour per response, including the time for reviewing instruction, searching existing data sources, gathering and maintaining the data needed, and completing and reviewing the collection of information. Send comments regarding this burden estimate or any other aspect of this collection of information, including suggestions for reducing this burden, to Washington headquarters Services, Directorate for Information Operations and Reports, 1215 Jefferson Davis Highway, Suite 1204, Arlington, VA 22202-4302, and to the Office of Management and Budget, Paperwork Reduction Project (0704-0188) Washington, DC, 20503.			
1. AGENCY USE ONLY (Leave blank)	2. REPORT DATE June 2021	3. REPORT TYPE AND DATES COVERED Master's thesis	
4. TITLE AND SUBTITLE ORIENTATION DEPENDENT MECHANICAL PROPERTIES OF 3D PRINTED POLYMER MATRIX COMPOSITES		5. FUNDING NUMBERS NPS-20-N076-A	
6. AUTHOR(S) Charles L. Hodgkins			
7. PERFORMING ORGANIZATION NAME(S) AND ADDRESS(ES) Naval Postgraduate School Monterey, CA 93943-5000		8. PERFORMING ORGANIZATION REPORT NUMBER	
9. SPONSORING / MONITORING AGENCY NAME(S) AND ADDRESS(ES) Naval Postgraduate School, Monterey, CA, 93943		10. SPONSORING / MONITORING AGENCY REPORT NUMBER	
11. SUPPLEMENTARY NOTES The views expressed in this thesis are those of the author and do not reflect the official policy or position of the Department of Defense or the U.S. Government.			
12a. DISTRIBUTION / AVAILABILITY STATEMENT Approved for public release. Distribution is unlimited.		12b. DISTRIBUTION CODE A	
13. ABSTRACT (maximum 200 words) The use of composite materials for 3D printing is a promising area of study that is largely under-researched. Traditionally manufactured composites are known to have superior mechanical qualities, yet characteristics of 3D printed composite materials are not well documented. In this study, polylactic acid composite filaments with both bronze and stainless-steel reinforcements were characterized using optical microscopy, X-ray powder diffraction, energy dispersive X-ray spectrometry, scanning electron microscope, and nanoindentation to determine reinforcement concentration and elemental composition of the filaments. Samples of each composite were printed with a fused deposition modeling 3D printer for compression and tensile testing in accordance with ASTM standards. Specimens with varying print patterns, build directions, and layer heights were tested to determine the efficacy of each material reinforcement and the effect these user-defined parameters have on the overall mechanical characteristics of the composite. Samples were subjected to 500 hours of accelerated weathering according to ASTM standards. Degradation was due largely to the ultraviolet exposure of the test, and the metallic reinforcements showed reduced crystallinity and resistance to physical deformation. This research provides the Navy and Department of Defense with qualitative data to determine the applicability of 3D printed parts for use in structural and load-bearing components onboard submarines.			
14. SUBJECT TERMS 3D printing, additive manufacturing, composite filament, reinforced polylactic acid, mechanical properties, orientation dependent, graphene reinforced, bronze reinforced, steel reinforced, raster pattern		15. NUMBER OF PAGES 101	
		16. PRICE CODE	
17. SECURITY CLASSIFICATION OF REPORT Unclassified	18. SECURITY CLASSIFICATION OF THIS PAGE Unclassified	19. SECURITY CLASSIFICATION OF ABSTRACT Unclassified	20. LIMITATION OF ABSTRACT UU

THIS PAGE INTENTIONALLY LEFT BLANK

Approved for public release. Distribution is unlimited.

**ORIENTATION DEPENDENT MECHANICAL PROPERTIES OF 3D PRINTED
POLYMER MATRIX COMPOSITES**

Charles L. Hodgkins
Lieutenant, United States Navy
BSME, Old Dominion University, 2015

Submitted in partial fulfillment of the
requirements for the degree of

MASTER OF SCIENCE IN MECHANICAL ENGINEERING

from the

**NAVAL POSTGRADUATE SCHOOL
June 2021**

Approved by: Andy Nieto
Advisor

Young W. Kwon
Co-Advisor

Garth V. Hobson
Chair, Department of Mechanical and Aerospace Engineering

THIS PAGE INTENTIONALLY LEFT BLANK

ABSTRACT

The use of composite materials for 3D printing is a promising area of study that is largely under-researched. Traditionally manufactured composites are known to have superior mechanical qualities, yet characteristics of 3D printed composite materials are not well documented. In this study, polylactic acid composite filaments with both bronze and stainless-steel reinforcements were characterized using optical microscopy, X-ray powder diffraction, energy dispersive X-ray spectrometry, scanning electron microscope, and nanoindentation to determine reinforcement concentration and elemental composition of the filaments. Samples of each composite were printed with a fused deposition modeling 3D printer for compression and tensile testing in accordance with ASTM standards. Specimens with varying print patterns, build directions, and layer heights were tested to determine the efficacy of each material reinforcement and the effect these user-defined parameters have on the overall mechanical characteristics of the composite. Samples were subjected to 500 hours of accelerated weathering according to ASTM standards. Degradation was due largely to the ultraviolet exposure of the test, and the metallic reinforcements showed reduced crystallinity and resistance to physical deformation. This research provides the Navy and Department of Defense with qualitative data to determine the applicability of 3D printed parts for use in structural and load-bearing components onboard submarines.

THIS PAGE INTENTIONALLY LEFT BLANK

TABLE OF CONTENTS

I.	INTRODUCTION.....	1
A.	MOTIVATION	1
B.	CURRENT STATE OF THE ART	1
	1. Introduction to Additive Manufacturing.....	1
	2. Fused Deposition Modeling.....	3
	3. FDM Material Selection	4
	4. Mechanical Characterization of 3D Printed PLA.....	4
C.	MECHANICAL CHARACTERISTICS OF 3DP PLA COMPOSITES.....	10
D.	THESIS OBJECTIVES.....	12
II.	MATERIALS AND METHODS	13
A.	COMPOSITE PRINTING	13
	1. Print Pattern.....	14
	2. Build Direction	15
	3. Layer Thickness	15
	4. Printer Settings.....	15
B.	MECHANICAL TESTING.....	16
	1. Compression Testing	16
	2. Tensile Testing.....	17
C.	ACCELERATED WEATHERING	19
D.	CHARACTERIZATION	20
	1. Optical Microscopy.....	20
	2. X-Ray Diffraction (XRD)	20
	3. Scanning Electron Microscope (SEM).....	21
	4. Energy Dispersive X-Ray Spectroscopy (EDS).....	21
	5. Nano Indentation	22
III.	RESULTS AND DISCUSSION	25
A.	MICROSTRUCTURAL CHARACTERIZATION OF STARTING FIBERS	25
	1. Optical Micrograph Analysis of Metal Particulate Volume Fraction.....	25
	2. XRD.....	29
	3. Scanning Electron Microscopy Analysis of Filaments	33
	4. EDS Analysis of Bronze PLA Filament	37

B.	NANOSCALE MECHANICAL PROPERTIES OF FILAMENTS.....	41
C.	MECHANICAL BEHAVIOR OF 3D PRINTED COMPOSITES	45
1.	Compression Testing	45
2.	Tensile Testing.....	49
3.	Analysis of Printed Specimen Particulate Concentration.....	51
4.	Estimation of Composite Elastic Modulus Based on Volume Fraction.....	56
5.	SEM Analysis of Layer Thickness Impact on Porosity	58
D.	ACCELERATED WEATHERING	64
1.	Optical Imaging.....	67
2.	XRD.....	67
IV.	CONCLUSIONS	71
V.	POTENTIAL DIRECTIONS FOR FUTURE WORK.....	73
	LIST OF REFERENCES.....	75
	INITIAL DISTRIBUTION LIST	79

LIST OF FIGURES

Figure 1.	(a) CAD model versus STL approximation. Source: [2]. (b) Model slicing using Cura software.....	2
Figure 2.	(a) General FDM 3D printer design. Source: [7]. (b) FDM nozzle detail view. Source: [8]......	3
Figure 3.	Sketch of ISO-527 specimens. Types 1A & 1B and ISO-37 specimens Type 2. Source: [10]......	5
Figure 4.	Tensile Stress-Strain curves of PLA and TPU95A with 20%,60%,100% infill. Source: [10]......	6
Figure 5.	Compression Stress-Strain curves of PLA with 20%,60%,100% infill. Source: [10]......	6
Figure 6.	PLA tensile specimen geometry. Source: [6].	7
Figure 7.	Ultimate tensile strength as a function of the number of perimeters (left) and layer thickness (right). Source: [6]......	8
Figure 8.	Top surface microstructure of 3D printed (a) PLA and (b) PLA-Graphene. Fractured cross-sectional microstructure of 3D printed (c) PLA and (d) PLA-graphene. Source [11].	9
Figure 9.	Compression test results for stainless-steel PLA composites compared to pure PLA. Source [12].	10
Figure 10.	SEM images of PLA with 316 stainless steel reinforcements. (a) PLA filament with 5% (PLA5) 316 stainless reinforcement. (b) PLA5 scaffold showing particles covered with PLA. (c) PLA10 showing the formation of voids. (d) PLA15 showing particle agglomeration and the formation of voids and inter-bead gaps. Source [12]......	11
Figure 11.	Lulzbot Mini 3D printer. Source [13].	13
Figure 12.	Infill patterns printed in the XYZ direction. (a) 0-degree lines, (b) 90-degree lines, (c) $\pm 45^\circ$ lines, (d) concentric.....	14
Figure 13.	Bronze PLA printed compression test specimens. Foreground samples are printed in the XYZ direction. Samples in the back of the image are printed in the ZXY direction.	17

Figure 14.	(a) ASTM D368 tensile test standard dog-bone geometry. Source: [15]. (b) Detail of stress concentrations at the termination of print beads in the fillet region of dog-bone. Source: [16]. (c) Rectangular tensile specimen geometry used printed with stainless steel and bronze PLA composites.	18
Figure 15.	Cura schematic showing infill raster pattern of test sample geometry.	19
Figure 16.	Q-Lab QUV/se Accelerated Weathering Tester	20
Figure 17.	Load-displacement curve displaying the slope of the unloading section used to determine the stiffness value. Source: [21].	23
Figure 18.	Filament sections. Side cut left, end cut right. Bronze PLA top, stainless-steel PLA bottom.	25
Figure 19.	Bronze PLA filament side cut images. (a) Image taken at low magnification. (b) Intermediate magnification showing bronze particles. (c) high magnification image of nanoindentation point taken of bronze particle. (d) High magnification image showing semi-circular bronze particles and partial voids.	26
Figure 20.	Bronze PLA side cut concentration analysis of optical images using ImageJ software. (a) initial image taken at 2.5x magnification, (b) image converted to greyscale (8-bit), (c) image threshold scaling to identify Cu-Sn particles. (d) summation of the area of all particles accounted for approximately 15.1%.	27
Figure 21.	Stainless steel PLA side cut imaging. (a) 2.5x magnification, (b) 10x magnification, (c) 20x magnification.....	28
Figure 22.	Stainless Steel PLA side cut concentration image analysis. (a) initial image taken at 2.5x magnification, (b) image converted to greyscale (8-bit), (c) image threshold scaling to identify Cu-Sn particles. (d) summation of the area of all particles accounted for approximately 14.9%.	29
Figure 23.	XRD Pattern for bronze PLA sample (included Miller indices of the various peaks)	30
Figure 24.	XRD pattern identification of stainless steel sample.	31
Figure 25.	XRD Pattern for stainless steel PLA filament (included Miller indices of the various peaks).....	32
Figure 26.	XRD pattern of 304L stainless steel. Source: [22].	33

Figure 27.	SEM images of bronze PLA filament. (a) side cut of filament at 1000x magnification showing bronze particle and adjacent void in the PLA matrix. (b) detail view at 5000x magnification of the interface between bronze particle and PLA matrix. (c) 2000x magnification detail of bronze particle with evidence of grinding scratches on two surfaces. (d) 2000x magnification of partially dislodged particle. (e) end cut of filament at 1.81Kx magnification, showing particles covered in PLA.	35
Figure 28.	SEM images of stainless steel PLA filament. (a) end cut of filament at 795k magnification. (b) end cut of filament at 111x magnification. (c) side cut of filament showing reinforcement particle and void in the PLA matrix.....	36
Figure 29.	Bronze PLA filament end-cut EDS spectrum.	37
Figure 30.	Bronze PLA filament side-cut EDS spectrum.	38
Figure 31.	(a) End-cut section of bronze PLA filament showing particles covered with PLA whose primary constituent is carbon. (b) Side-cut section showing exposed bronze particles evidenced by the copper circles.	39
Figure 32.	EDS elemental maps for bronze PLA filament (end-cut). (a) carbon, (b) tin, (c) oxygen, (d) copper.	40
Figure 33.	EDS elemental color contrast for bronze PLA filament (side-cut). (a) carbon, (b) tin, (c) oxygen, (d) copper.	40
Figure 34.	Bronze filament bimodal distribution. Group 1 represents bronze reinforcement particles. Group 2 represents bronze particles that experienced slippage through the PLA matrix during testing.	43
Figure 35.	Nano-hardness loading curves for PLA regions of 3D printed composites and composite filaments.	44
Figure 36.	Nano-hardness loading curves for metallic reinforcement particles of 3D printed composites and composite filaments.	45
Figure 37.	PLA composite failure mechanisms with 0.2 mm layer heights. (a) Bronze PLA sample with 90° line pattern printed in XYZ direction. (b) Bronze PLA sample with ±45° lines printed in XYZ direction. (c) Stainless steel PLA sample with ±45° lines printed in ZXY direction.	46
Figure 38.	PLA composite compression test results. (a) Bronze ±45° line pattern, (b) Bronze concentric infill pattern, (c) Bronze 0° and 90°	

	line infill patterns. (d) Stainless steel $\pm 45^\circ$ line pattern, (e) Stainless steel concentric infill pattern, (f) Stainless steel 0° and 90° line infill patterns.....	48
Figure 39.	Bronze and stainless-steel PLA composite compression test results summary for Young's Modulus. (a) $\pm 45^\circ$ line pattern, (b) Concentric infill pattern, (c) 0° and 90° line infill patterns.....	49
Figure 40.	Tensile test summary for bronze and stainless steel PLA printed with $\pm 45^\circ$ and 0° lines and a layer height of 0.1mm. Data is representative of the average of the five samples from each test sample.....	50
Figure 41.	Modes of failure of PLA composites printed with $\pm 45^\circ$ lines under tensile loading. (a) Brittle failure of stainless steel PLA. (b) Ductile failure of bronze PLA.	51
Figure 42.	Image processing of stainless steel PLA $\pm 45^\circ$ lines printed in the ZXY direction with 0.2mm layer height.....	52
Figure 43.	Image processing of stainless steel PLA $\pm 45^\circ$ lines printed in the ZXY direction with 0.1mm layer height.....	53
Figure 44.	(a) Stainless steel PLA $\pm 45^\circ$ line infill pattern with 0.1mm layer height printed in ZXY direction. (b) Detail view showing the edge of a region of increased porosity.	54
Figure 45.	Image processing of bronze PLA $\pm 45^\circ$ lines printed in the ZXY direction with 0.2mm layer height.....	54
Figure 46.	Image processing of stainless steel PLA $\pm 45^\circ$ lines printed in the ZXY direction with 0.1mm layer height.....	55
Figure 47.	Bronze PLA: $\pm 45^\circ$ lines printed in ZXY direction with 0.1mm layer height. (a) Bronze particle dislodged from PLA matrix and dragged from left to right during sample preparation. (b) Semi-circular bronze particle with polishing scratches on two sides leaving behind a half-circle void.	56
Figure 48.	Stainless steel PLA composite printed with $\pm 45^\circ$ line infill pattern in the ZXY direction and a layer height of 0.2mm. (a) 100x magnification showing uniformity of porosity across surface. (b) higher mag image showing good particle to substrate adhesion.....	60
Figure 49.	Stainless steel PLA composite printed with $\pm 45^\circ$ line infill pattern in the ZXY direction and a layer height of 0.1mm. (a) 100x magnification showing inconsistent porosity. (b) higher mag image	

	of particle separation and crack propagation due to a difference in thermal conductivity.	60
Figure 50.	Stainless steel PLA composite printed with concentric infill pattern in the ZXY direction and a layer height of 0.2mm. (a) 200x magnification showing good inter-bead adhesion. (b) 1000x detail of an area of porosity near print bead interface.....	61
Figure 51.	Stainless steel PLA composite printed with concentric infill pattern in the ZXY direction and a layer height of 0.1mm. (a) low magnification showing separation between print beads. (b) detail showing PLA separation at print bead interface.	62
Figure 52.	Bronze PLA composite printed with concentric infill pattern in the ZXY direction and a layer height of 0.1mm. (a) low magnification showing the homogeneous distribution of particles and porosity. (b) detail showing porosity and particles with good adhesion with PLA matrix.	63
Figure 53.	Side images of samples printed in the ZXY direction with concentric infill pattern. (a) bronze PLA with 0.1mm layer height. (b) bronze PLA with 0.2mm layer height. (c) stainless steel PLA with 0.1mm layer height. (d) stainless steel PLA with 0.2mm layer height.	64
Figure 54.	Specimens subjected to 200 hours accelerated weathering. Control sample is the upper left image in each figure: (a) Neat PLA, (b) Bronze PLA, (c) Stainless steel PLA.	66
Figure 55.	Visual comparison of white chalky surface on stainless steel PLA samples at different stages of accelerated weathering: (a) control, (b) 200 hours and (c) 500 hours.....	66
Figure 56.	Stainless steel reinforced PLA surface of control (a) and after 200 hours (b). Bronze reinforced PLA control (c) and after 200 hours (d). Optical images were taken at 20x magnification.	67
Figure 57.	PLA specimen mounted in 24mm open tray and Rigaku Miniflex 600 XRD (inset).....	68
Figure 58.	XRD data overlay for control samples.....	69
Figure 59.	XRD data for 500-hour samples.	70

THIS PAGE INTENTIONALLY LEFT BLANK

LIST OF TABLES

Table 1.	Stainless steel and bronze reinforced PLA printer parameters.	16
Table 2.	Summary of XRD analysis for bronze PLA	30
Table 3.	Summary of XRD analysis for stainless steel PLA	32
Table 4.	Bronze PLA bimodal data separation	42
Table 5.	Nanoindentation test results.....	45
Table 6.	Summary of calculated results compared to experimentally measured results for bronze and stainless steel printed composites with $\pm 45^\circ$ lines built in the <i>ZXY</i>	58

THIS PAGE INTENTIONALLY LEFT BLANK

LIST OF ACRONYMS AND ABBREVIATIONS

3DP	3D printing
ABS	acrylonitrile butadiene styrene
AM	additive manufacturing
CAD	computer-aided design
COMSUBPAC	Commander, Submarine Force, U.S. Pacific Fleet
DOD	Department of Defense
EDS	energy dispersive X-ray spectrometry
FDM	fused deposition modeling
PLA	polylactic acid
SEM	scanning electron microscope
SLA	stereolithography
SLM	selective laser melting
SLS	selective laser sintering
TPU	thermoplastic polyurethane
UTS	ultimate tensile strength
UV	ultraviolet
XRD	X-ray powder diffraction

THIS PAGE INTENTIONALLY LEFT BLANK

ACKNOWLEDGMENTS

For my children Olivia, Owen, and Emily.

THIS PAGE INTENTIONALLY LEFT BLANK

I. INTRODUCTION

A. MOTIVATION

Over the last decade, 3D printing has become a rapidly growing field of study. The Navy and DOD have recently been interested in implementing 3D printing on ships and submarines as a low-cost alternative to obtaining parts that may be difficult to obtain due to long lead times or perhaps be obsolete and impossible to procure entirely. The ability to create replacement parts of complex geometries on the spot will greatly benefit the Navy by saving money and time and ultimately improving mission readiness by helping ships stay at sea.

While a 3D printed replacement part may have the same geometry as the original, the mechanical characteristics could be quite different. Conventionally manufactured composite materials are known to deliver superior mechanical properties compared to their polymeric material counterparts. It would follow logic that 3D printing with composites would yield similar benefits. The development of composite filaments for 3D printing is a recent one, and therefore the study of 3D printed composites is in the earliest stages of research and development.

With 3D printing, there are several variables that the user can modify, such as raster patterns, layer thickness, build directions, in addition to many others. In making changes to such print variables, it is essential first to understand the material's properties and then the role each variable has on the overall mechanical characteristics.

B. CURRENT STATE OF THE ART

A literature review was conducted to gain an understanding of the current state of the art in the research of 3D printed composite materials. This review was used to gain a base understanding and guide the research conducted.

1. Introduction to Additive Manufacturing

The process of additive manufacturing (AM) is, in the simplest terms, the manufacturing of something layer by layer. This process was formally referred to as rapid

prototyping and is now more commonly referred to as AM or 3D printing (3DP), which is actually a subset of AM. AM contrasts with traditional techniques such as milling or grinding that are subtractive in nature. The first obvious advantage of AM is that there is very little wasted material. Secondly, AM has the unique advantage of being able to create complex geometries that would otherwise require the use of numerous types of traditional manufacturing techniques or perhaps be impossible to develop altogether [1].

The 3DP process begins virtually with computer-aided design (CAD) modeling. Once the designer has the desired geometry modeled in CAD software, the CAD file must then be converted to an STL file. STL stands for “Standard Triangle Language” and in effect, converts curved surfaces into a series of triangles [2]. A depiction of this concept is illustrated in Figure 1a.

With the use of 3D printing software such as Cura, the STL file is uploaded, and printer parameters are set. The software then converts the STL file with the selected print parameters into a G-code, which is used to control the 3D printer and breaks the print into a series of slices [3], as depicted in Figure 1b. There are many parameters that the user defines based on the final design criteria. The process of going from design to physically printing a part is very quick, allowing design changes to easily be made and implemented, which makes 3DP an ideal method of prototyping. Conventional processes such as injection molding or extruding are more time-consuming and costly due to the need to create new molds for each design iteration while prototyping.

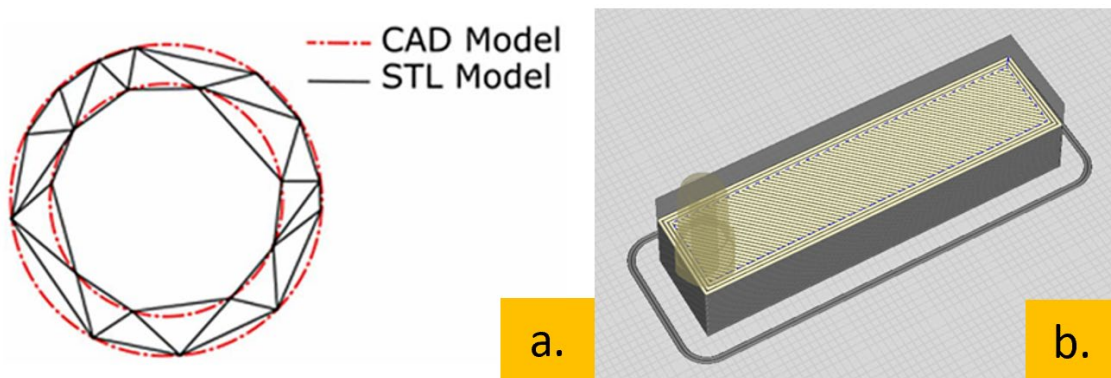


Figure 1. (a) CAD model versus STL approximation. Source: [2]. (b) Model slicing using Cura software.

2. Fused Deposition Modeling

There are many different types of 3D printers, such as selective laser melting (SLM), selective laser sintering (SLS), stereolithography (SLA), and fused deposition modeling (FDM), to name a few. A wide range of materials can be used depending on the printing method, with the most common being polymers [4]. This study will focus on the use of FDM printing.

With the expiration of S. Scott Crump's FDM patent in 2009 (U.S. Patent 5121329A), the use of FDM printers has become increasingly popular in the last decade due to the ease of use, affordability, and availability of 3D printers to the general public [4]-[6]. FDM printers use a continuous filament feedstock that is fed through a heated nozzle where the filament is heated to a molten state. The molten material is first deposited onto a heated print bed then built up in layers. The printer builds in 3 directions, namely the X, Y, and Z directions, as seen in Figure 2a [7]. The printer bed and nozzle are both free to move in the X-Y plane, depositing material to form the first 'slice' of the product. After each layer is complete, the printer head or bed is then raised or lowered accordingly in the Z direction to build each subsequent layer (Figure 2b) [8]. Since the print material must be heated to a molten state, there are obvious limitations to the types of materials that can be printed with FDM.

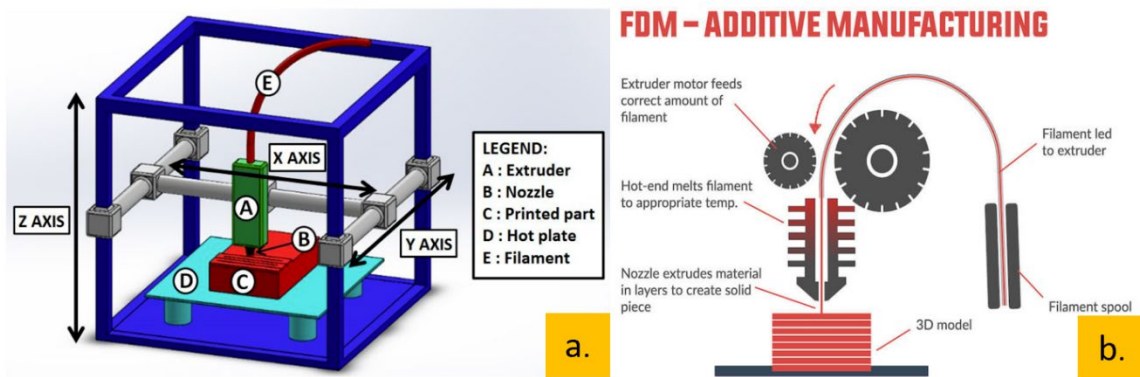


Figure 2. (a) General FDM 3D printer design. Source: [7]. (b) FDM nozzle detail view. Source: [8].

3. FDM Material Selection

Thermoplastics such as poly-lactic acid (PLA) and acrylonitrile butadiene styrene (ABS) have relatively low melting temperatures making them popular for FDM applications. Properties of PLA, such as high strength, and biocompatibility, make it a good candidate for applications such as food packaging and biomedicine applications. Unlike most plastics, PLA is a plant-based thermoplastic that is biodegradable, thereby making it both an environmentally friendly and sustainable material [9].

PLA has long been used for rapid prototyping with 3D printers; however, real-world applications have been limited when a high level of mechanical, thermal, and flame retardant properties are required [9]. In addition, PLA is considered a brittle material with low impact strength and flexibility [10]. Over the last several years, many new composite materials have been introduced to the commercial market that could improve the mechanical characteristics of pure thermoplastics.

4. Mechanical Characterization of 3D Printed PLA

It is no secret that the mechanical characteristics of 3D printed parts will have different mechanical characteristics from those created by traditional methods. With 3D printing, there is a litany of parameters the user can modify, which may, in turn, affect other mechanical characteristics of the print. Several studies have been conducted to see what impacts changing specific parameters has on printing PLA and its composites. The majority of studies focus on neat PLA and tensile properties. However, the information presently available for PLA composites and especially compressive properties of PLA composites is minimal.

a. PLA and TPU in Tension and Compression

Elmrabet and Siegkas [10] tested PLA and TPU according to ISO tensile and compression testing standards to examine the impact print parameters have on mechanical characteristics. Samples were printed with 20%, 60%, and 100% infill densities, while other parameters such as layer height, print speed, and temperature were held constant. Besides infill density, specimen size was varied. The tensile specimens had three different

sample geometries, as seen in Figure 3. The compressive specimens had diameters of 5 and 10 mm [10].

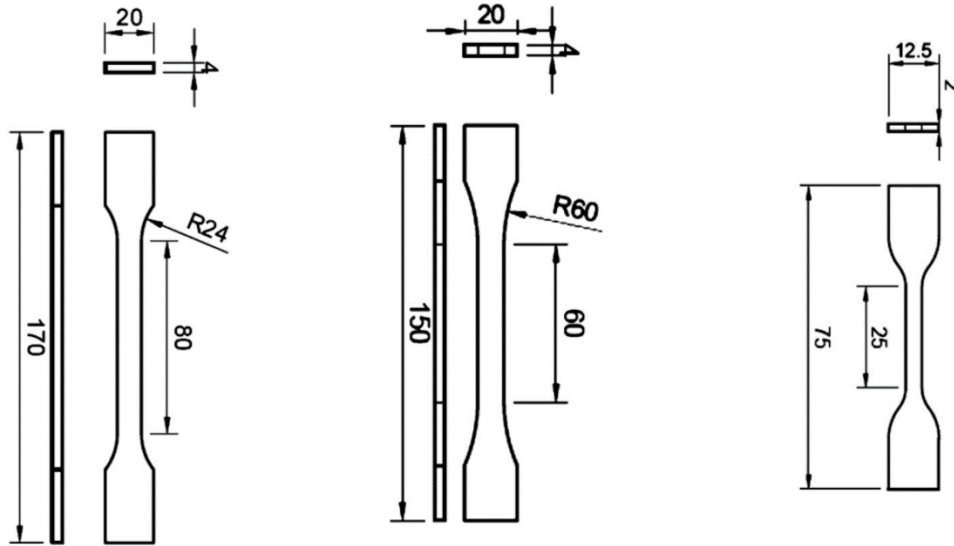


Figure 3. Sketch of ISO-527 specimens. Types 1A & 1B and ISO-37 specimens Type 2. Source: [10].

Tensile testing in this study showed that the relationship between ultimate tensile strength (UTS) and infill density is not linear. The increase in strength from 20% to 60% was less than the improved strength obtained when going up to 100% infill from 60%. In Figure 4, the smallest sample (PLA-37-2 in red) at 20% behaved comparably with the larger specimens (PLA-527-1A&B in teal and yellow) at 100% infill [10].

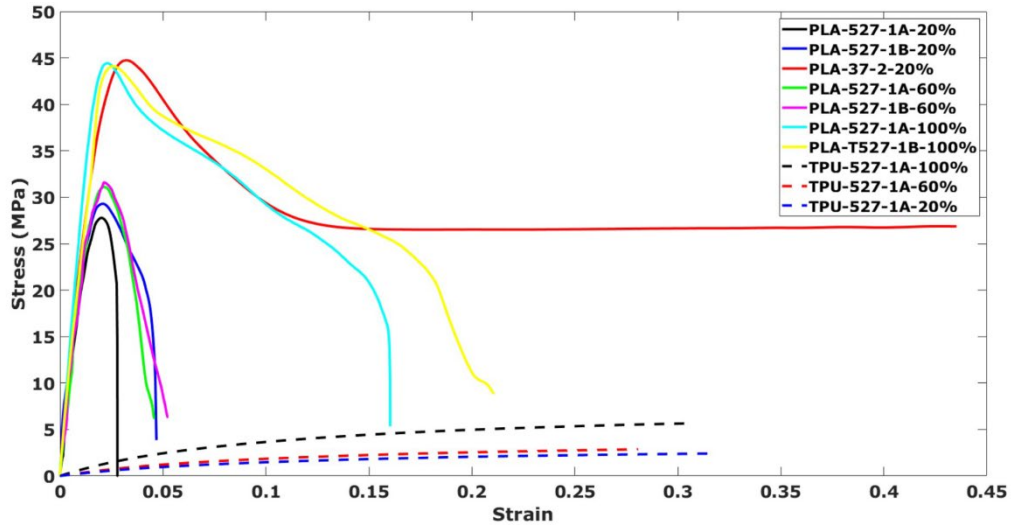


Figure 4. Tensile Stress-Strain curves of PLA and TPU95A with 20%,60%,100% infill. Source: [10].

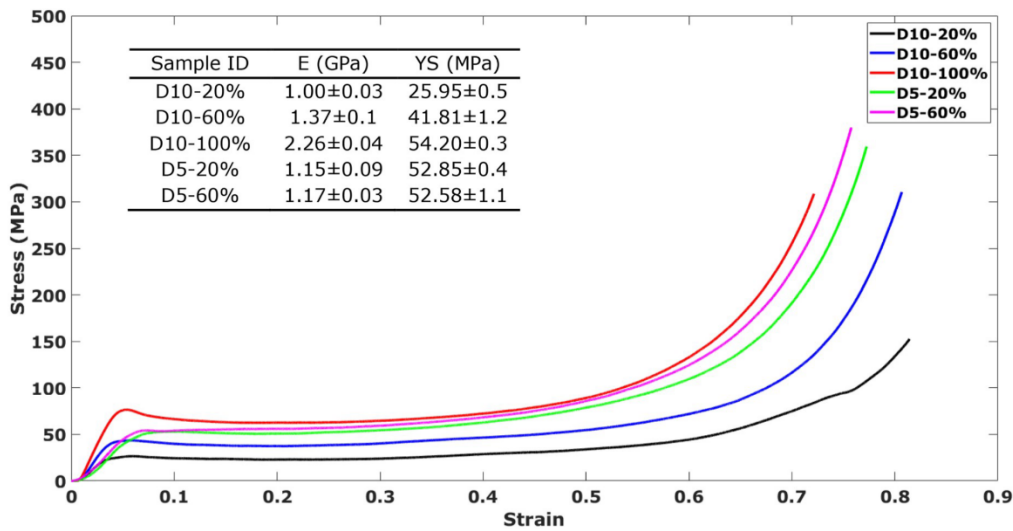


Figure 5. Compression Stress-Strain curves of PLA with 20%,60%,100% infill. Source: [10].

In [10], it was shown that infill percentage plays a significant role in the mechanical characteristics. It was found that density had the most significant effect on both tensile (Figure 4) and compressive (Figure 5) performance. Testing suggests that smaller geometry can lead to an increase in density, even with lower infill settings. This may be due in part

to the accuracy of the 3D printer being used, as lower-end printers will have less print resolution [10].

b. Layer Thickness, Infill Orientation, and Shell Perimeters Impact on Ultimate Tensile Strength

Lanzotti et al. [6] investigated the influence of the print parameters layer thickness, infill orientation, and the number of shell perimeters has on mechanical properties. Test specimens were printed with varying line angle orientations of 0, 18, 45, 72, and 90 degrees relative to the load direction, as depicted in Figure 6 [6].

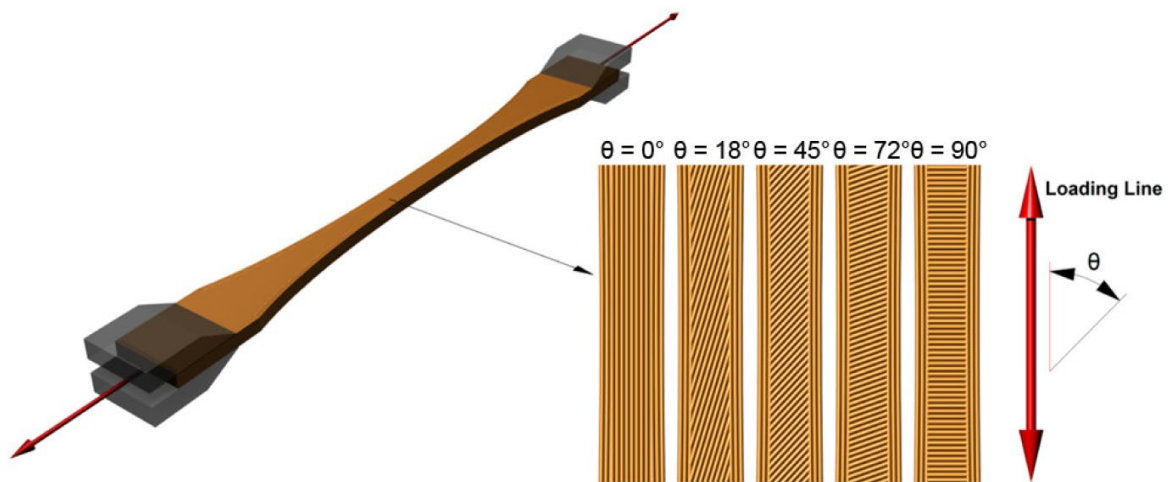


Figure 6. PLA tensile specimen geometry. Source: [6].

Printing tensile test specimens in strict accordance with testing standards such as ASTM 638 is known to have inconsistent points of fracture due to stress concentrations caused by the variation of curvature. Lanzotti et al. modified the standard geometry using a parabolic curvature to ensure fracture occurred consistently in the area of the minimum cross-section. This geometry modification resulted in consistent breakage in the minimum cross-section area in all 60 samples tested in this study [6].

Lanzotti et al. [6]. found that tensile strength increased as the print angle approached the line of the applied load. This is due to the load being carried solely by the fibers at an angle of 0 degrees from longitudinal. As the angle increased, the load begins

to be taken by the inter-fiber bonding increasingly up to the point of 90 degrees where the load is carried solely by fiber-to-fiber bonding. Strength was improved as the layer thickness and the number of perimeter layers was increased. With fibers printed in line with the load, the number of perimeter layers becomes insignificant. As the layer thickness increased, there will first be a drop in UTS followed by a rise as the thickness is further increased (Figure 7). This is due to the initial increase in air gaps between fibers. Interestingly, as the thickness is increased, the flowing polymer material will fill these gaps in the previous layer, thereby increasing the bonded surface area and improving the fiber bond strength. As the layer thickness is increased further, the UTS then begins to drop [6].

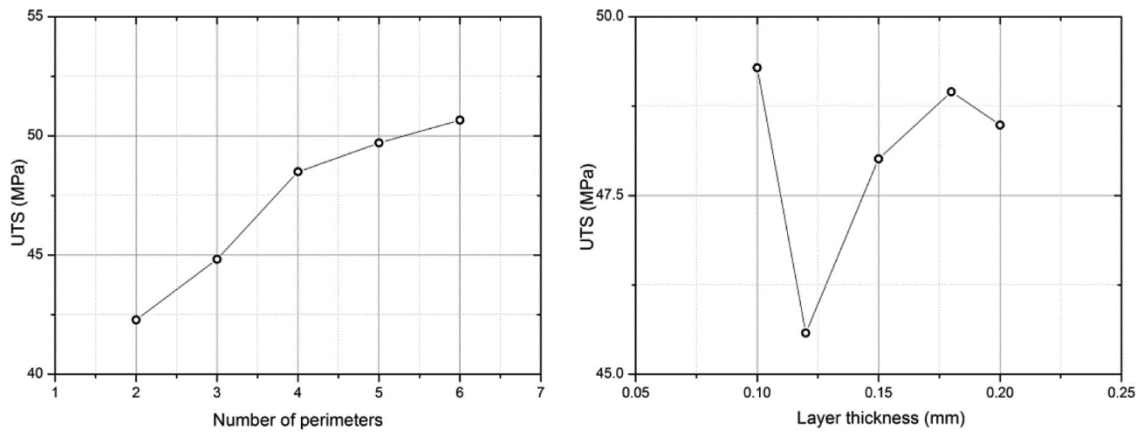


Figure 7. Ultimate tensile strength as a function of the number of perimeters (left) and layer thickness (right). Source: [6].

c. PLA and PLA-Graphene Nano-Hardness and Tribological Wear Testing Characterization.

Bustillos et al. [11]. tested PLA and PLA-graphene composite filaments for nano-hardness and tribological characteristics. PLA-graphene composite was shown to have a lower density yet improved mechanical characteristics when compared to pure (neat) PLA. Improvements were seen in the areas of elastic modulus, tensile strength, conductivity, and wear resistance.

Nozzle sizes of both 0.4mm and 0.6mm were used for the samples. A larger nozzle size was necessary to prevent clogging when printing the graphene reinforced PLA. It was

determined that the clogging was not due to the agglomeration of graphene flakes but rather to the thermal expansion of the PLA filament due to the increased thermal conductivity as a result of the graphene reinforcements. The higher thermal conductivity of the graphene additives resulted in the weak interlayer and intralayer bonding seen in Figure 8. This is due to the creation of voids resulting from the thermal strain mismatch between the graphene and PLA substrate caused by the rapid cooling rate of the PLA-graphene [11].

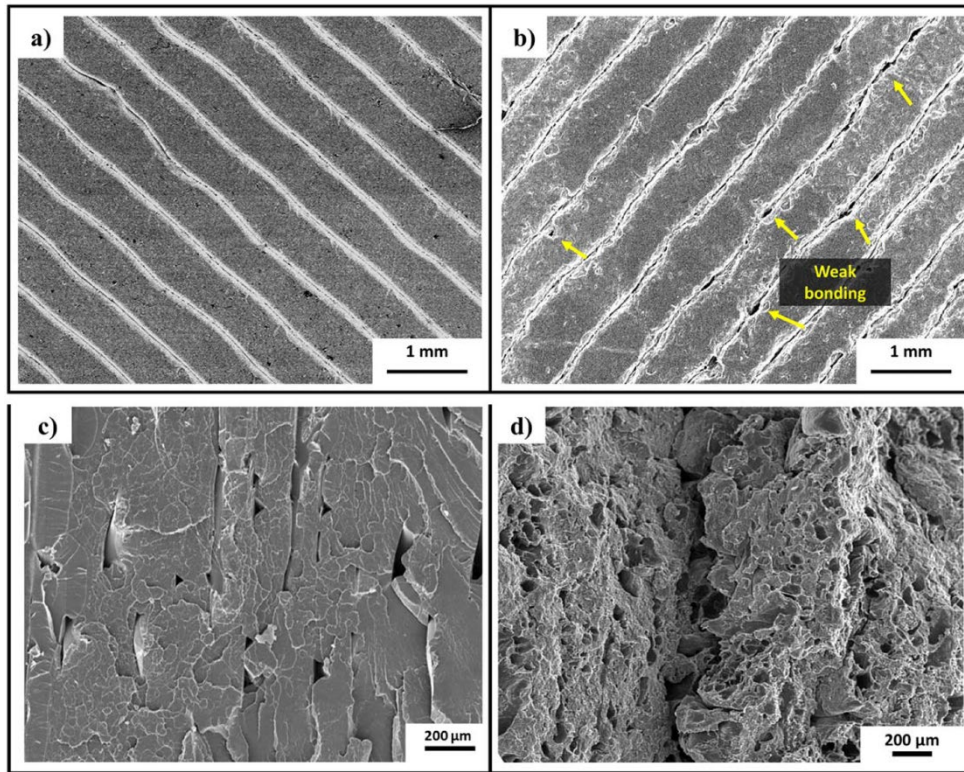


Figure 8. Top surface microstructure of 3D printed (a) PLA and (b) PLA-Graphene. Fractured cross-sectional microstructure of 3D printed (c) PLA and (d) PLA-graphene. Source [11].

The addition of graphene flakes resulted in an overall improvement in mechanical characteristics over neat PLA. For example, the elastic modulus was improved by 37%, while tensile strength saw a 75% improvement and resistance to plastic deformation improved by 25%. Such improvements are due to the orientation process the graphene flakes undergo when being pushed through the printer nozzle. This structure allows applied

stress to be transferred to the graphene reinforcement particles resulting in increased overall hardness and resistance to deformation [11].

The overall weight percentage of graphene reinforcements was limited to about 5.6% to prevent clogging of the printer nozzle. This can also be alleviated with the use of a larger printer nozzle diameter [11].

C. MECHANICAL CHARACTERISTICS OF 3DP PLA COMPOSITES

In [12], 316 stainless-steel PLA composite filaments were studied for use in medical scaffolds. The reason for using stainless instead of other metals such as titanium is due to the human body's increased tolerance for iron absorption compared to titanium. Three sample filaments were made consisting of 5, 10, and 15% concentrations of 316 stainless steel by weight. The stainless particle sizes varied between 20 and 50 μm . Samples were printed with a Lulzbot TAZ 6 3D printer [12].

The compressive performance of each was compared to that of pure PLA in Figure 9. It was found that there was an increase in compressive modulus of elasticity with the addition of stainless steel reinforcements. The best performance came not from the sample with the highest concentration but from the PLA10 sample [12].

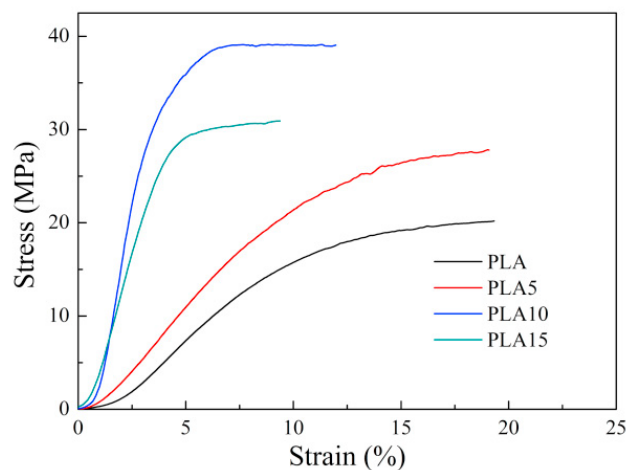


Figure 9. Compression test results for stainless-steel PLA composites compared to pure PLA. Source [12].

Jiang and Ning found that as the concentration was further increased to 15%, a decrease in performance was experienced. With an increase in particle concentration, a corresponding increase in porosity is seen in the SEM images in Figure 10. This is due partly to particle agglomeration. While the diameter of the filament is relatively large (2.85mm) relative to the particle size, the layer height of 0.2mm is much closer to the size of the stainless steel particles. With low concentrations of stainless steel particles, there was a homogeneous distribution of the particles [12]. As the concentration is increased, the steel particles, which are 0.02-0.05 mm, will begin to agglomerate, thereby impeding the flow of the bead, which is only 0.2 mm. Additionally, as the particles agglomerate, there is a possibility that they will stack, making contact with one another. The contact between particles leads to the formation of gaps between the beads and can potentially cause stress concentrations.

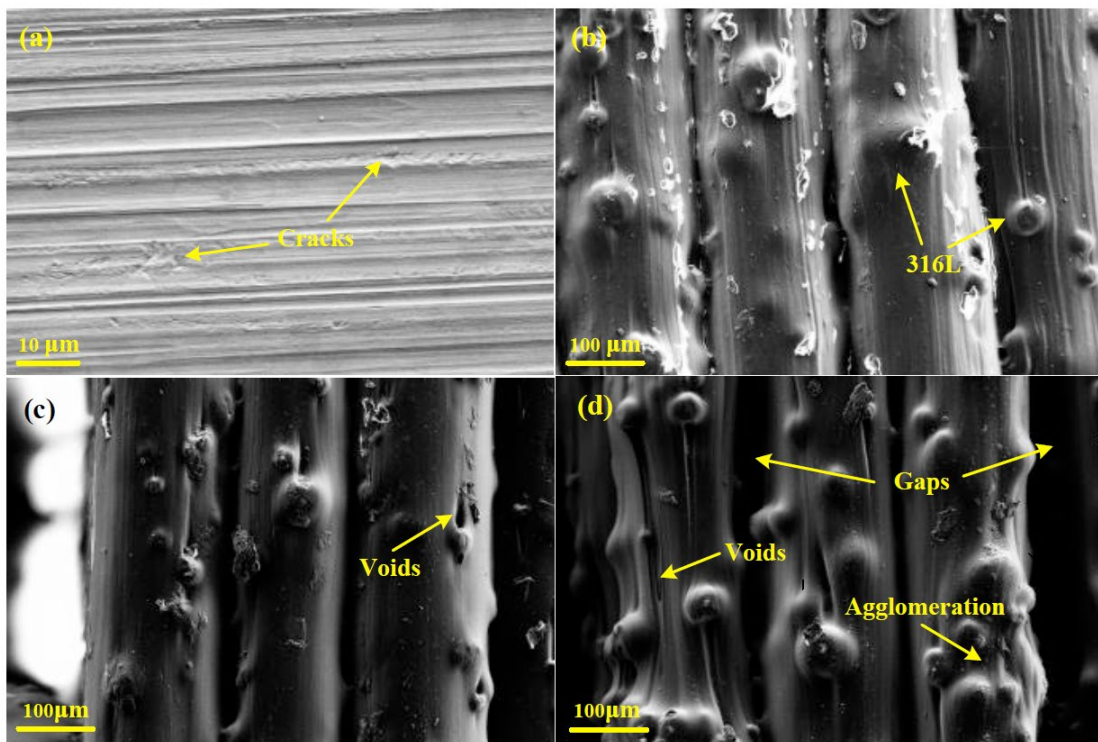


Figure 10. SEM images of PLA with 316 stainless steel reinforcements. (a) PLA filament with 5% (PLA5) 316 stainless reinforcement. (b) PLA5 scaffold showing particles covered with PLA. (c) PLA10 showing the formation of voids. (d) PLA15 showing particle agglomeration and the formation of voids and inter-bead gaps. Source [12].

D. THESIS OBJECTIVES

This study will provide the Navy and DOD with quantitative data to determine the applicability of 3D printed parts for use in structural and load-bearing components. The availability of low-cost 3D printed parts provides a means to rapidly make parts that may otherwise be unavailable from the manufacturer or have extended lead times. This is of great benefit to the Navy as it allows units to make replacement parts on the spot, shorten repair times, and keep ships at sea. Ultimately, the aim of this study is two-fold:

- Understand the impact that changing printer parameters have on the compressive and tensile mechanical behavior. Parameters investigated will include layer height (0.1mm and 0.2mm), infill pattern ($\pm 45^\circ$, concentric, 0° and 90° lines), and build direction (flat and vertical).
- Evaluate the efficacy of bronze and stainless-steel particulate reinforcements in a PLA matrix in enhancing compressive mechanical properties.

II. MATERIALS AND METHODS

A. COMPOSITE PRINTING

This research aims to determine the feasibility of utilizing 3D printed parts for structural load-bearing components, that could for example, be used onboard submarines, which is of interest to COMSUBPAC. Of course, it goes without saying that space is of utmost concern for these vessels. For this reason, the Lulzbot Mini 3D printer (Figure 11) was chosen to print all samples. The only significant difference between the standard and mini versions is the reduction in print size imposed by the machine's compactness. The printer head is otherwise the same, and therefore print parameters such as nozzle temperature or speed are unchanged.

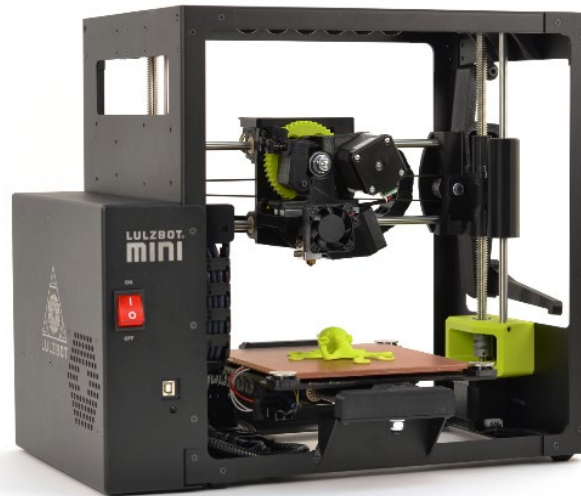


Figure 11. Lulzbot Mini 3D printer. Source [13].

There are many new filament materials available, and this research will focus on two metal-reinforced PLA composite filaments, both measuring 2.85mm in diameter. The stainless steel reinforced PLA made by ProtoPasta (Vancouver, WA, US) and ColorFabb's (Belfeld, Netherlands) Bronzefill PLA were studied. While many parameters can be

modified by the user when 3D printing, this research aims to determine the effects print pattern, build direction, and layer thickness have on overall mechanical characteristics.

1. Print Pattern

A 3DP model consists of a series of slices or layers built on top of one another. Each layer comprises two regions: an outer shell, also referred to as the wall, and the infill. A wall width of 1.5 mm, which equates to 3 wall layers of 0.5 mm, was the default size used by the Cura software and was held constant throughout. The infill is measured as a percentage of fill, with 100% having the highest density. Many patterns can be chosen for the infill of 3D printed parts. For this research, four infill patterns were chosen. Two orientations of line patterns were selected along with a concentric and zig-zag pattern. Longitudinal lines are 0° or in line with load direction, while the transverse lines are 90° or perpendicular to the applied load. The concentric pattern is a series of circles of decreasing size starting from the shell. The final infill pattern is a zig-zag pattern with alternating layers of $\pm 45^\circ$ layers. The infill patterns are illustrated in Figure 12. For illustrative purposes, the layer thickness and bead width are exaggerated.

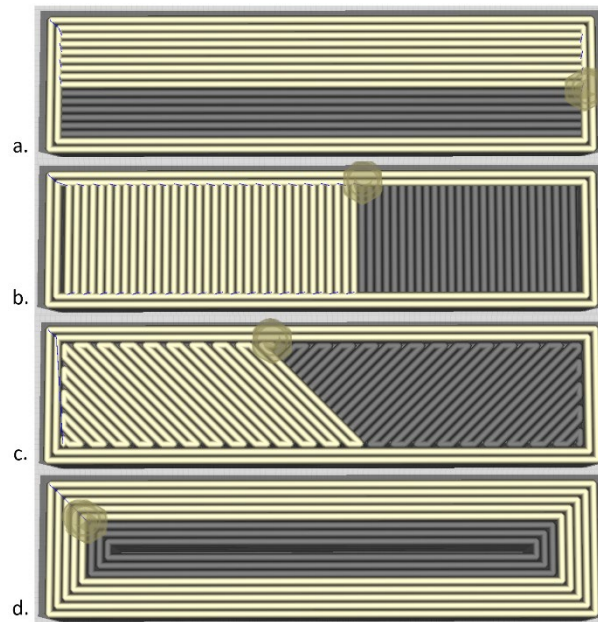


Figure 12. Infill patterns printed in the XYZ direction. (a) 0-degree lines, (b) 90-degree lines, (c) $\pm 45^\circ$ lines, (d) concentric.

2. Build Direction

The next variable investigated was the build direction. There are three directions that the printer uses to generate a part. The printer bed itself is the X-Y plane, and it is in this plane each slice is generated in Cura. The layers are built by adjusting the printer nozzle vertically in the Z direction. Generally, there would be three directions that a part can be printed. Parts are printed flat, on the side, or vertically. For the rectangular prism, two directions can be printed because flat and on the side are the same by geometry. In this test, the side print is referred to as the XYZ direction, and vertical prints are the ZXY direction.

3. Layer Thickness

The final user-defined parameter tested was layer thickness. Cura will take the defined layer thickness and use this parameter to determine the total number of layers (or slices) necessary to obtain the final geometry of the model. Thus, a reduction in layer thickness increases the total number of layers and yields a finer overall appearance and increased geometric precision.

4. Printer Settings

3D printing is highly customizable, with a vast amount of printer settings that the user can modify. This research aimed to see the impact changing layer height, print pattern, and build direction had on the mechanical characteristics. Cura has many of the commonly used filaments available for selection. The following table summarizes the printer setting adjustments. The rest of the printer settings were taken mainly as manufacturer recommendations or default settings in Cura.

Table 1. Stainless steel and bronze reinforced PLA printer parameters.

Parameters	Stainless Steel-PLA	Bronze-PLA
Print Temp (°C)	225	220
Infill (%)	100	100
Wall Thickness (mm)	1.5	1.5
Line Width (mm)	.5	0.5
Layer Height (mm)	0.1/0.2	0.1/0.2
Build Plate Temp (°C)	60	50
Print Speed (mm/sec)	60	25

B. MECHANICAL TESTING

1. Compression Testing

There has been very little research conducted on the compressive characteristics of 3D printed polymers and even less on composites specifically. The area of study is relatively new, and thus a specific testing standard has yet to be created. The test standard that best suited this study was ASTM D695: Compressive Properties of Rigid Plastics. This testing standard is designed for unreinforced and reinforced plastics with a modulus of elasticity less than or equal to 41,370 MPa. It is stated that test specimens can be either compression molded or machined to obtain the desired test geometry [14]. The use of 3D printing is not mentioned and thus is a deviation from the testing standard.

a. Test Specimen Geometry

Test samples must be in the shape of either a right cylinder or rectangular prism. There is some flexibility in the choice of test specimen geometry as long as there is a “sufficient slenderness ratio.” ASTM D695 specifies that a length that is two times the principal diameter or width is sufficient. In cases where the elastic modulus is desired, the stated preferred specimen dimensions of 12.7mm x 12.7mm x 25.4mm (0.50” x 0.5” x 2.0”) were chosen [14]. Due to the nature of 3D printing, the rectangular prism was chosen with the preferred dimensions stated and shown in Figure 13. The cylindrical geometry, while possible, would have resulted in wasted material used for required support when printing in the XYZ direction. Before testing, the dimensions of each test specimen were recorded.



Figure 13. Bronze PLA printed compression test specimens. Foreground samples are printed in the XYZ direction. Samples in the back of the image are printed in the ZXY direction.

b. Compressive Test

Compression tests were carried out using the INSTRON (INSTRON Corp., Norwood, USA) testing machine. This machine can apply load to the sample at a constant rate of 1.5 mm/min (0.050 in/min) as required by ASTM D695 [14]. Compressive strength can be somewhat vague, and tests are generally stopped after a desired amount of strain. In this study, the samples were allowed to go longer than they otherwise would in order to get an idea of the overall toughness and failure mechanisms the different print orientations experienced.

2. Tensile Testing

Similar to compression testing, a testing standard for tensile properties of 3DP materials has not yet been determined. For this study, ASTM D368: Standard Test Method for Rigid Plastics was chosen. This test standard is acceptable for use with both unreinforced and reinforced rigid plastics and was administered using an INSTRON test machine at a constant loading rate of 2.0 mm/min (0.079 in/min)[15].

a. Test Specimen Geometry

It is stated that the test specimen geometry shall be of a bar-bell shape. This geometry is to ensure breakage within the gauge-length section, G (Figure 14a) [15]. While this geometry is sufficient for molded or machined specimens, 3D printing poses difficulties due to the nature of 3D printing. The curved area contains stress concentrations where the infill layers terminate as they meet the wall layer shown with the arrows in Figure 14b [16]. A purely rectangular geometry would be a sufficient deviation to mitigate these potential stress concentrations. Therefore, rectangular bar specimens can be used to minimize stress concentrations and ensure consistent data, as Rankouhi et al. showed [16].

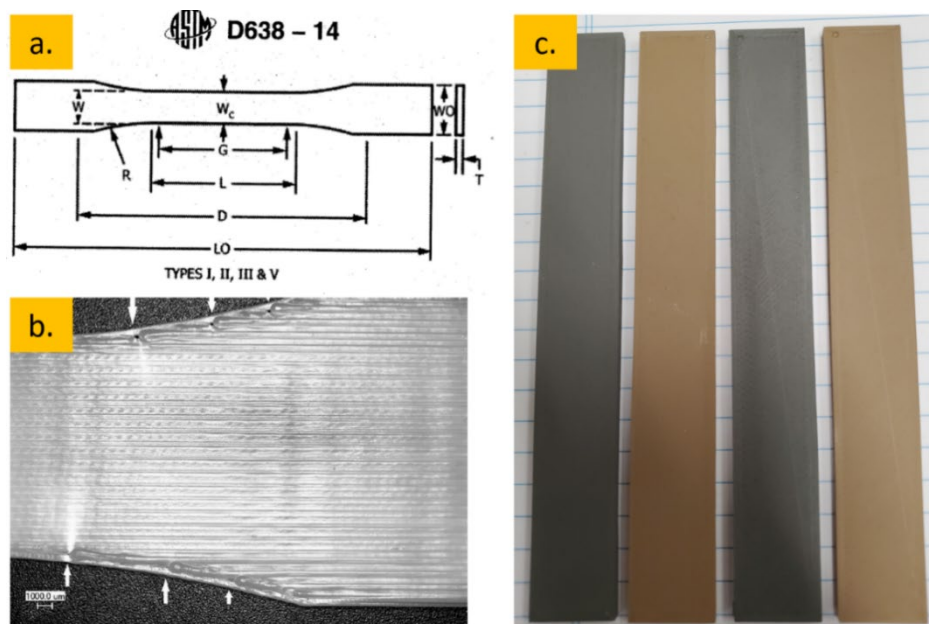


Figure 14. (a) ASTM D368 tensile test standard dog-bone geometry. Source: [15]. (b) Detail of stress concentrations at the termination of print beads in the fillet region of dog-bone. Source: [16]. (c) Rectangular tensile specimen geometry used printed with stainless steel and bronze PLA composites.

b. Tensile Test

ASTM D368 states that five samples shall be tested, and any abnormalities shall be thrown out. Two patterns were tested for each material: $\pm 45^\circ$ lines and 0° lines, both printed

with 0.1mm layer height built in the XYZ direction. Rectangular shaped bar specimens shown in Figure 14c, with dimensions 139.7mm x 19mm x3.2mm (5.5" x 0.75" x 0.126") were used to minimize stress concentrations and ensure consistent data. The choice of rectangular bars is a deviation from the standard dog-bone shape detailed by the test standard.

C. ACCELERATED WEATHERING

The bronze and stainless steel PLA composites, in addition to pure PLA samples, were subjected to 500 hours of accelerated weathering testing according to ASTM G154: Cycle 6. Rectangular samples (Figure 15) were printed with dimensions of 70 mm (l) x 50 mm (w) x 3 mm (t) (2.756" x 1.969" x 0.118") to fit within the sample holder trays of the accelerated weathering machine. For each material, three test samples were printed in addition to one control.

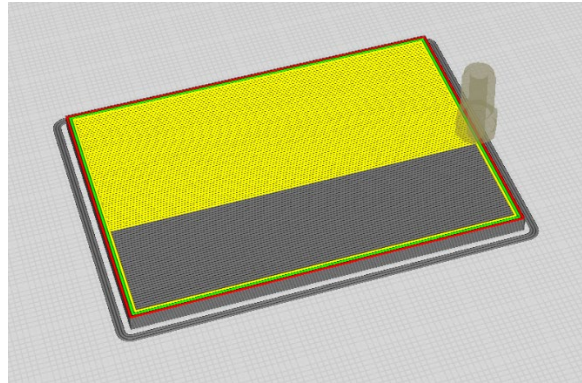


Figure 15. Cura schematic showing infill raster pattern of test sample geometry.

The accelerated weathering testing was conducted using a Q-Lab QUV/se Accelerated Weathering Tester, shown in Figure 16. Based on the standard test cycle ASTM G154: Cycle 6, the UV exposure was set to an irradiance of 1.55 W/m² and 60°C, and the condensation was set to 50°C [17]. Specimen dimensions and weights were measured and recorded before testing. Additionally, measurements were taken at 200 hours and finally after the completion of 500 hours of accelerated weathering testing.



Figure 16. Q-Lab QUV/se Accelerated Weathering Tester

D. CHARACTERIZATION

1. Optical Microscopy

In order to conduct optical microscopy, the specimens were prepared by mounting samples of the stainless steel PLA and bronze PLA in an epoxy disc. The mounted samples were ground with a series of 600, 800, and 1200 grit SiC paper to get rid of a majority of the scratches on the surface. The samples were then polished with a 1-micron diamond suspension. The optical images were taken from various magnifications and captured with the Nikon Epiphot 200 (Tokyo, Japan) software. Once the images were captured, they were processed using ImageJ to determine the concentration of reinforcement particles in the PLA matrix.

2. X-Ray Diffraction (XRD)

The use of a Rigaku Miniflex 600 XRD (Tokyo, Japan) machine was utilized to determine the composition of the 3D-printed composite materials. The XRD samples were

prepared using a hand file to create a fine powder from the printed samples. The powder is then easily packed into the sample tray for the XRD analysis. The machine settings used were 40 mV and 15 mA. A scanning rate of $7.0^\circ/\text{min}$ was used over a 2θ range of 10° to 100° [18].

The XRD parameters for the accelerated weathering test samples consisted of the standard 40kV/15mA aging and a 2θ scan range of 10° to 120° , at a scan speed of $4^\circ/\text{min}$ with a step size of 0.01° . PDF-4+ 2020 RDB, a product of the International Centre for Diffraction Data was used for a XRD database reference. The PDF's used as reference for this research were: 04-001-1512 (Cu_{0.9} Sn_{0.1}), 04-003-7057 (Cu_{0.97} Sn_{0.03}), 01-086-2722 (Chromium Iron), 00-064-1623 (PLA, semi-crystalline), and 00-064-1622 (PLA, amorphous).

3. Scanning Electron Microscope (SEM)

Samples were examined using a Zeiss NEON 40 Dual-beam SEM/FIB. The SEM uses a focused beam of electrons to scan the surface of interest, producing high-resolution images of topography and composition [19]. After the samples were ground and polished, they were sputter-coated with 4.2 nm of palladium using a Cressington (Watford, UK) 208HR sputter coater. Sputter coating works to increase the signal-to-noise ratio during SEM imaging due to its high conductivity, which results in better-quality images. Images were obtained using the 30 μm aperture with an accelerating voltage of 5–7kV at a working distance of 4.7mm.

4. Energy Dispersive X-Ray Spectroscopy (EDS)

Energy dispersive X-ray spectroscopy (EDS) was used to determine the elemental composition of the bronze PLA filament. EDS is another capability of the SEM where materials are characterized by the X-rays emitted when the surface is subjected to a beam of electrons. As the electron beam impacts an atom, one of its electrons is ejected, creating a vacancy in the valence shell. As electrons drop from higher shells to fill these voids, X-rays characteristic to the element are ejected to maintain an overall energy balance [20]. For the EDS analysis, the aperture of the SEM was increased to 120 μm in order to collect more electrons, with an accelerating voltage of 20kV at a working distance of 5mm.

5. Nano Indentation

Traditional hardness tests such as microhardness testing use a four-sided indenter tip of known geometry such as the Vickers geometry. With Vicker's hardness testing, a known force is applied, driving the tip into the surface, leaving behind an indent of a specific shape. Knowing the shape of the indenter and the force applied, the hardness can be obtained by measuring the indent. In the nanoscale, the applied force is much less, making it impossible to accurately measure such small areas. With nanoindentation testing, a sharper three-sided Berkovich style tip is necessary and is commonly used to measuring nano hardness by the Oliver-Pharr method [21].

In the Oliver-Pharr method [21], the values of stiffness, S , and indenter displacement height is measured directly to deduce other desired values using mathematical relationships. Stiffness is measured as the slope of the unloading curve seen in Figure 17. The indenter penetration height, h_c is directly measured and is proportional to the indentation section area A_c . For Berkovich tip, the proportional relationship is $A_c = 24.5h_c^2$. With the area known, hardness is calculated by simply dividing the applied force by A_c . With the values of A_c and S known, the effective modulus of elasticity, E_r is calculated as follows:

$$E_r = \left(\frac{\sqrt{\pi}}{2}\right) * \left(\frac{S}{\sqrt{A_c}}\right)$$

A couple of other values are necessary for the Oliver-Pharr calculations. For the indenter diamond tip, the values of elastic modulus, E , and Poisson's ratio, ν are known to be 1140 GPa and 0.07, respectively. Lastly, given the Poisson's ratio for the material the modulus can be found using the equation below. Subscript 1 represents the material being tested, while subscript 2 represents the indenter tip [21].

$$E_r = \left[\frac{(1 - \nu_1^2)}{E_1} + \frac{(1 - \nu_2^2)}{E_2}\right]^{-1}$$

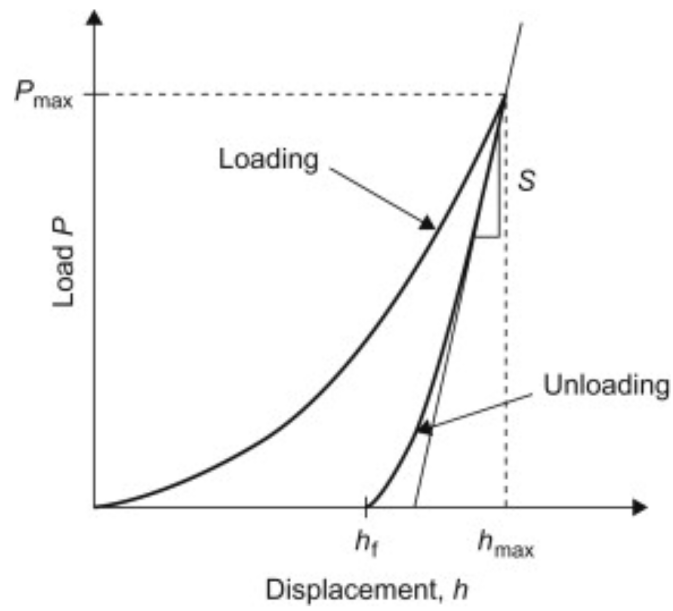


Figure 17. Load-displacement curve displaying the slope of the unloading section used to determine the stiffness value. Source: [21].

THIS PAGE INTENTIONALLY LEFT BLANK

III. RESULTS AND DISCUSSION

A. MICROSTRUCTURAL CHARACTERIZATION OF STARTING FIBERS

1. Optical Micrograph Analysis of Metal Particulate Volume Fraction

Two commercially available composite filaments were obtained for analysis. The first of which was BronzeFill made by ColorFabb, and the second of which was Proto Pasta's stainless steel PLA filament. Both companies lack detailed information on the composition and fabrication of their products. To understand the applicability a material has for real-world uses, one must first understand the properties of the base material being used. The first step was to determine the concentration of reinforcement materials present. The filaments were sectioned in two directions, as shown in Figure 18.

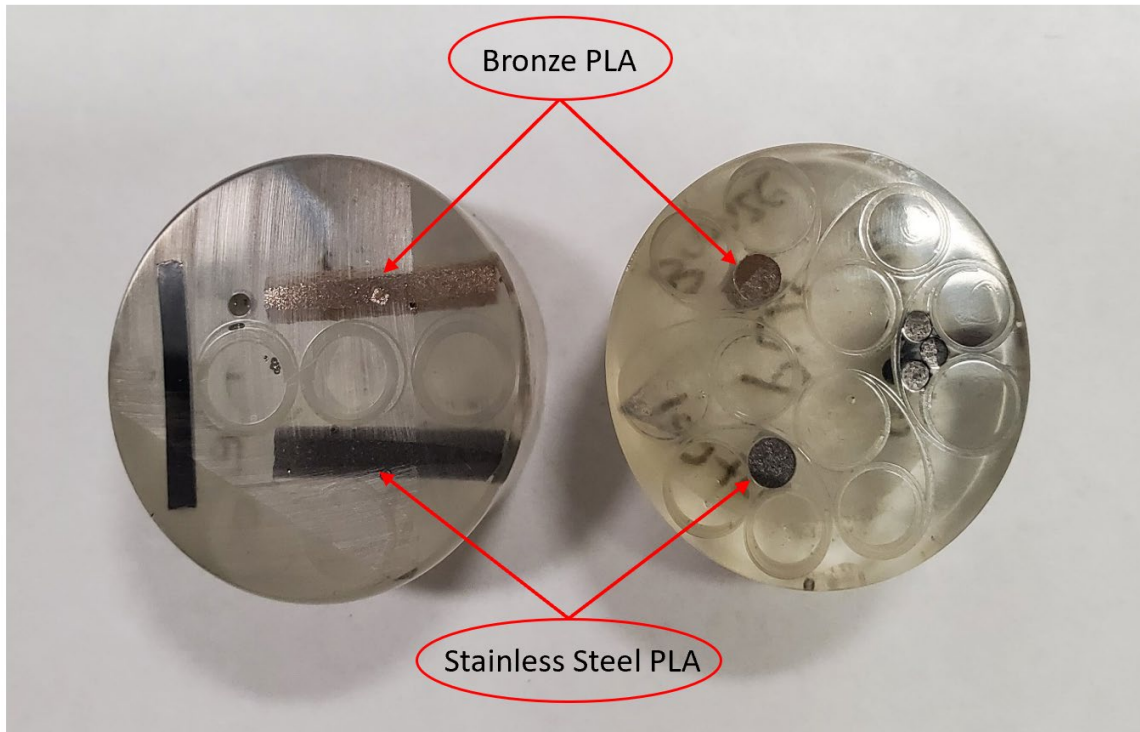


Figure 18. Filament sections. Side cut left, end cut right. Bronze PLA top, stainless-steel PLA bottom.

a. Side Cut Bronze Compositional Analysis

Three optical images were taken for the “side-cut” bronze PLA at various magnifications, as shown in Figure 19. The white particles are the Cu and Cu₃Sn intermetallic compound particles, while the darker grey substrate is the PLA matrix. Optical micrographs (Fig 19d) display metal particles that are semi-circular coupled with partial voids; this feature will be further explained in the SEM analysis segment.

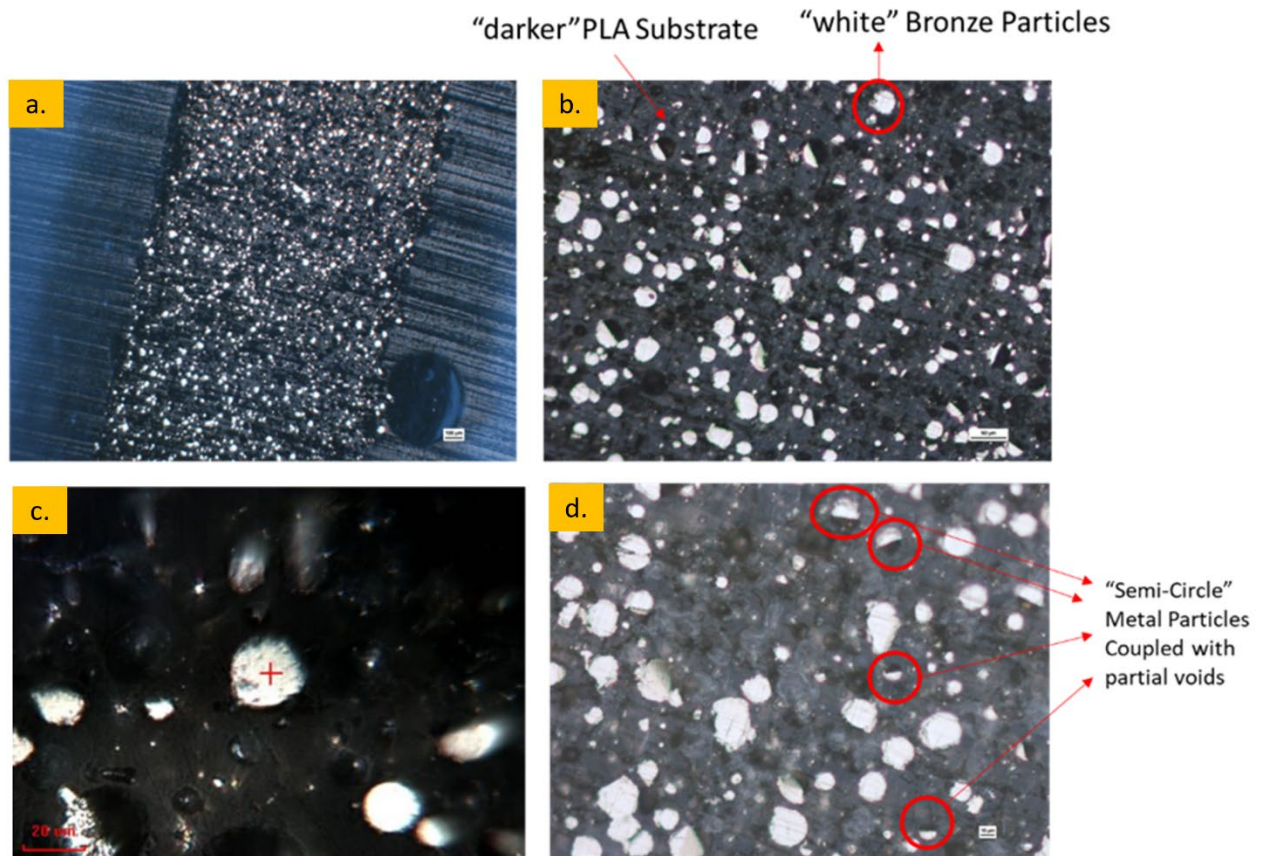


Figure 19. Bronze PLA filament side cut images. (a) Image taken at low magnification. (b) Intermediate magnification showing bronze particles. (c) high magnification image of nanoindentation point taken of bronze particle. (d) High magnification image showing semi-circular bronze particles and partial voids.

Images taken at low magnification (2.5x) were analyzed using ImageJ software to determine the area/volume fraction of the bronze particles against the PLA matrix in Figure

20. The analysis showed that the white particles of the bronze are estimated to be 15.1% while PLA occupying the darker grey regions is 84.9%. Refer to Figure 20 for the ImageJ analysis.

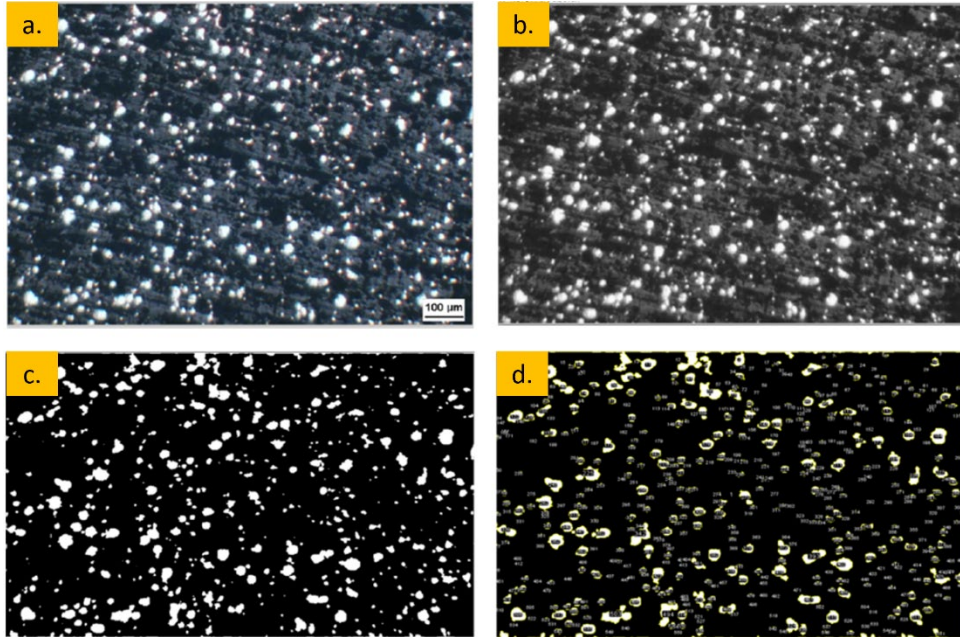


Figure 20. Bronze PLA side cut concentration analysis of optical images using ImageJ software. (a) initial image taken at 2.5x magnification, (b) image converted to greyscale (8-bit), (c) image threshold scaling to identify Cu-Sn particles. (d) summation of the area of all particles accounted for approximately 15.1%.

b. Side Cut Stainless Steel PLA Compositional Analysis

Three optical images were taken for the stainless steel PLA “side cut” at various magnifications, as shown in Figure 21. The white particles are stainless steel compounds, while the darker grey substrate is the PLA matrix.

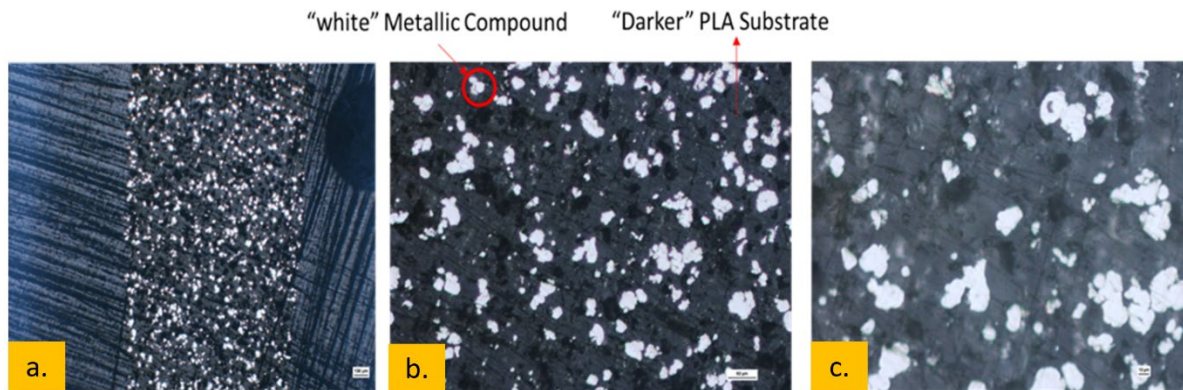


Figure 21. Stainless steel PLA side cut imaging. (a) 2.5x magnification, (b) 10x magnification, (c) 20x magnification.

The area/volume fraction of the stainless steel against the PLA matrix was determined by processing images taken at 2.5x magnification using the ImageJ software to determine the area occupied by the stainless steel. It was assumed that cross-sections were an accurate representation of the filament structure, and the cross-sectional area analysis was taken to be representative of the volumetric content of each phase. Analysis has shown that the particles of stainless steel are estimated to account for 14.9%. Refer to Figure 22 for the ImageJ analysis.

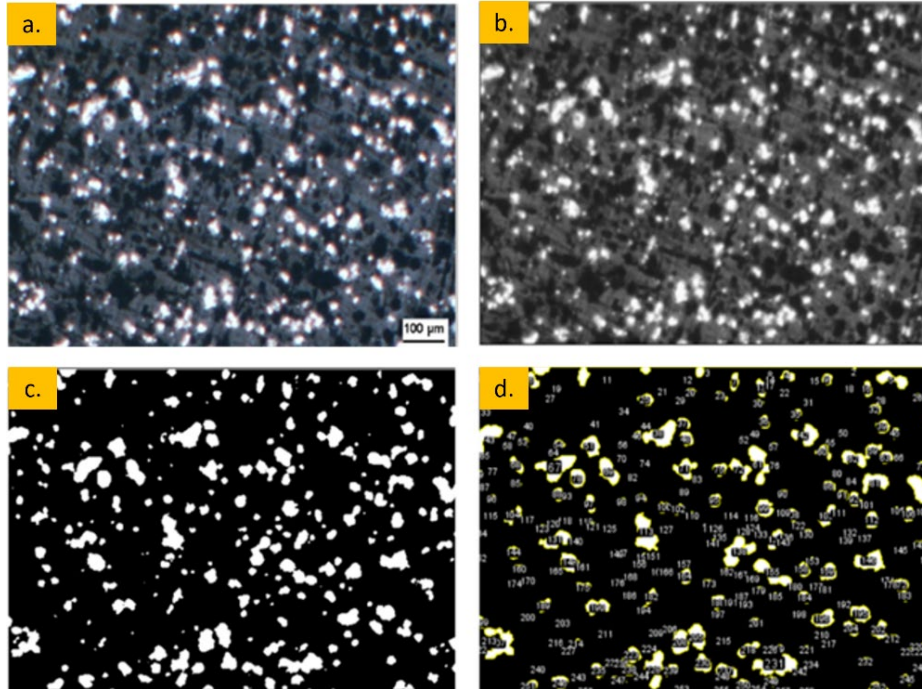


Figure 22. Stainless Steel PLA side cut concentration image analysis. (a) initial image taken at 2.5x magnification, (b) image converted to greyscale (8-bit), (c) image threshold scaling to identify Cu-Sn particles. (d) summation of the area of all particles accounted for approximately 14.9%.

2. XRD

The manufacturers of the composite filaments tested do not provide specific information as to the composition of their products. XRD analysis was used to gain knowledge about the chemical phase makeup of the filaments.

a. PDXL Analysis of Bronze PLA

The XRD analysis yielded Copper and Tin as the primary elements constituting the sample. PDXL (database) identified two different compositions of copper-tin: (1) 90 wt% Cu - 10 wt% Sn, (2) 97 wt% Cu – 3 wt% Sn. Both of which matched the peaks of the XRD pattern generated from the tested sample.

As shown in Figure 23, the original XRD pattern is superimposed with details such as the Miller indices of the various peaks at the respective 2θ angles. Peaks identified close

together had the same miller indices but at slightly different 2θ angles. This is due to the other component composition of Cu-Sn found in the sample. 2θ angles related to the miller indices, and d-spacings can be found in Table 2.

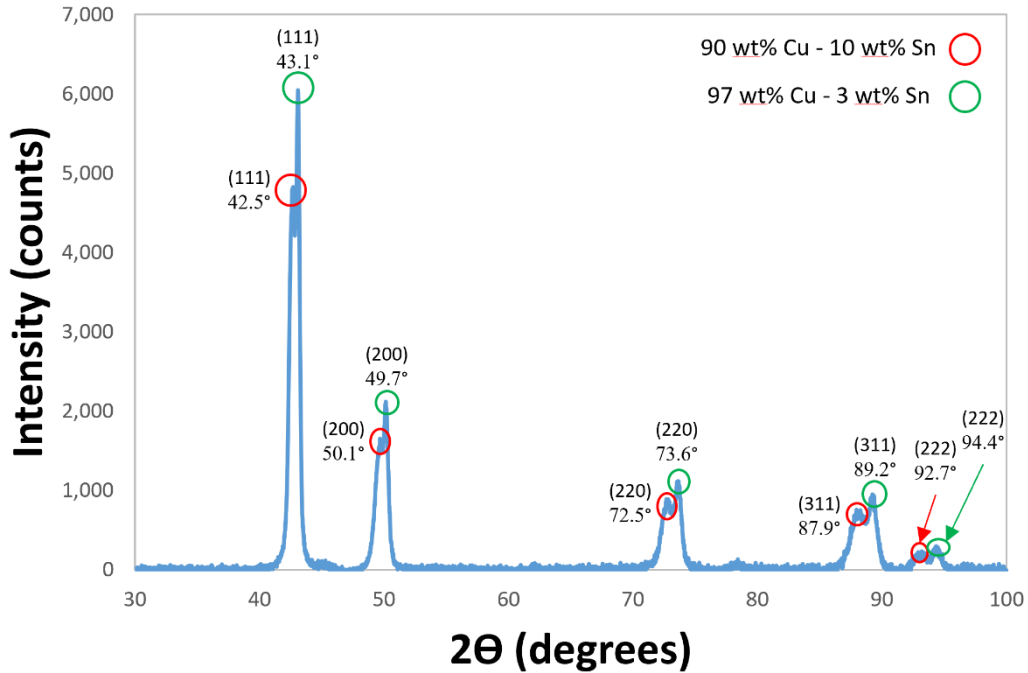


Figure 23. XRD Pattern for bronze PLA sample (included Miller indices of the various peaks)

Table 2. Summary of XRD analysis for bronze PLA

Bronze PLA XRD Summary				
No.	2-theta (deg)	d (angle)	Phase Name	DB Card No.
1	42.552	2.12286	CuSn (1,1,1)	04-001-1512
2	43.062	2.09888	CuSn (1,1,1)	04-003-7057
3	49.692	1.8333	CuSn (2,0,0)	04-001-1512
4	50.105	1.819	CuSn (2,0,0)	04-003-7057
5	72.542	1.3020	CuSn (2,2,0)	04-001-1512
6	73.571	1.28635	CuSn (2,2,0)	04-003-7057
7	78.45	1.2181	Unknown	0
8	87.955	1.10933	CuSn (3,1,1)	04-001-1512
9	89.167	1.09737	CuSn (3,1,1)	04-003-7057
10	92.69	1.0647	CuSn (2,2,2)	04-001-1512
11	94.42	1.0497	CuSn (2,2,2)	04-003-7057

b. PDXL Analysis of Stainless Steel PLA

The XRD analysis yielded iron and chromium as the primary elements constituting the sample. The PDXL database identified the compound Fe_3Cr (blue plot), which matched the original peaks of the XRD pattern generated from the tested sample (red plot), as shown in Figure 24.

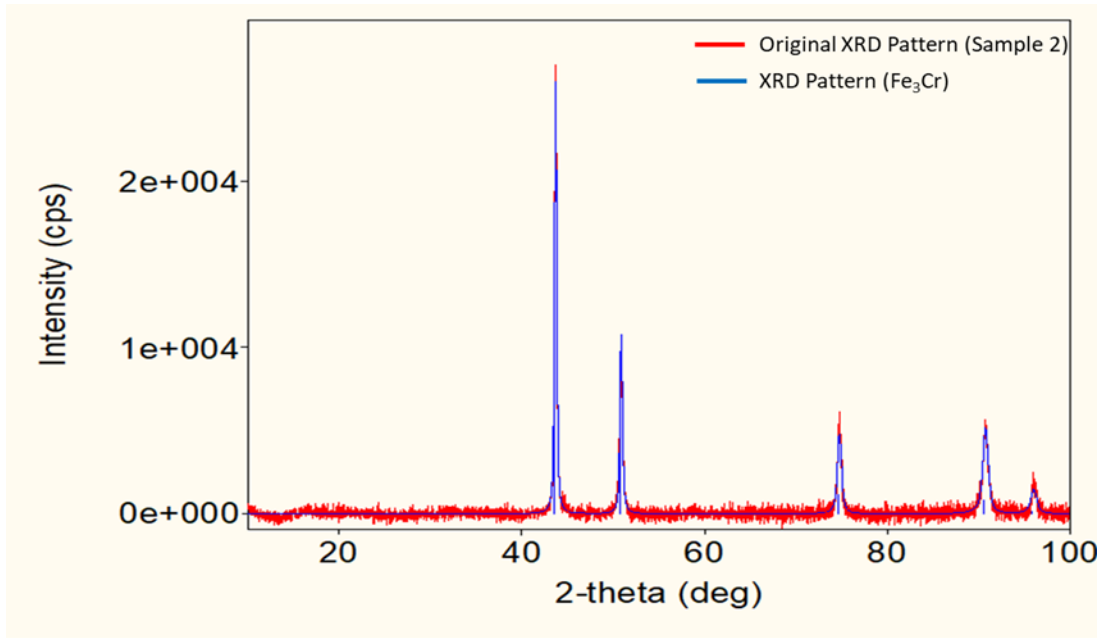


Figure 24. XRD pattern identification of stainless steel sample.

The original XRD pattern (sample2), as shown in Figure 25, superimposed with details such as the Miller indices of the various peaks at the respective 2θ angles. 2θ angles related to the miller indices and d-spacings can be found in Table 3.

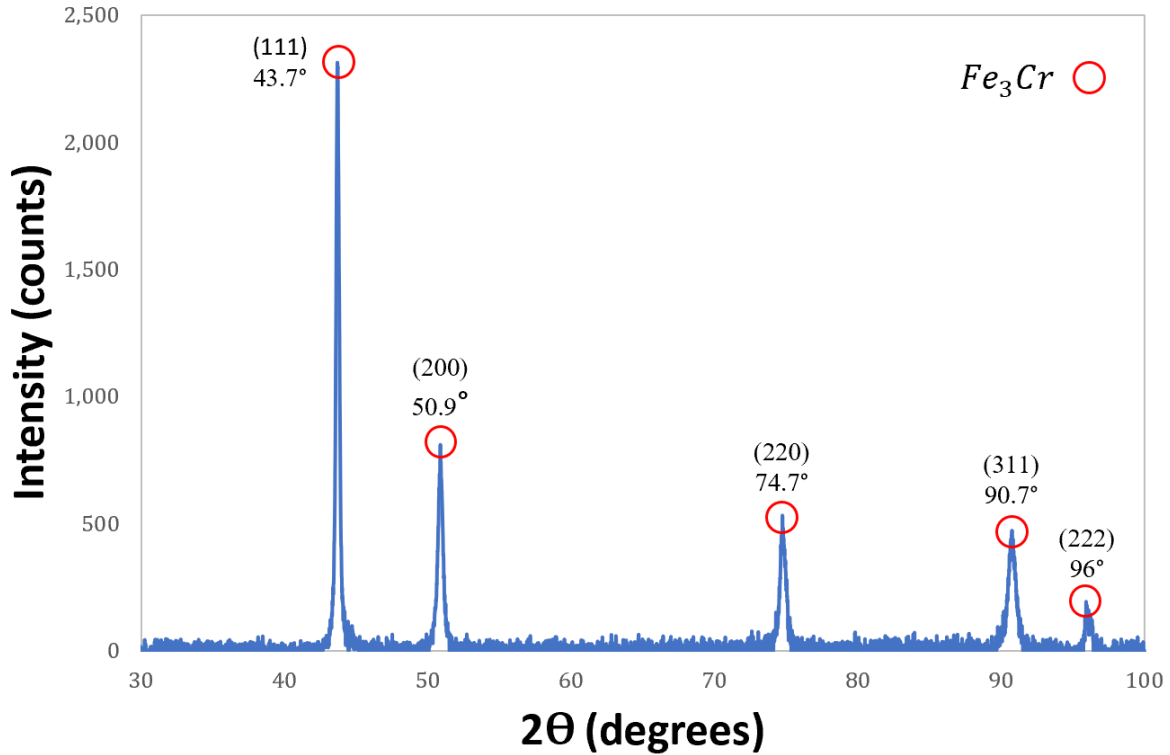


Figure 25. XRD Pattern for stainless steel PLA filament (included Miller indices of the various peaks).

Table 3. Summary of XRD analysis for stainless steel PLA

Stainless Steel PLA XRD Summary				
No.	2-Theta (deg)	d (angle)	Phase Name	DB Card No.
1	43.675	2.07084	CrFe (1,1,1)	01-086-2722
2	50.862	1.7938	CrFe (2,0,0)	01-086-2722
3	74.709	1.26955	CrFe (2,2,0)	01-086-2722
4	90.676	1.08300	CrFe (3,1,1)	01-086-2722

Additionally, the XRD pattern exhibited by the sample coincides with the XRD pattern (miller indices & 2θ) Lee et al. displayed in their study of fatigue crack growth of 304L stainless steel as shown in Figure 26 [22].

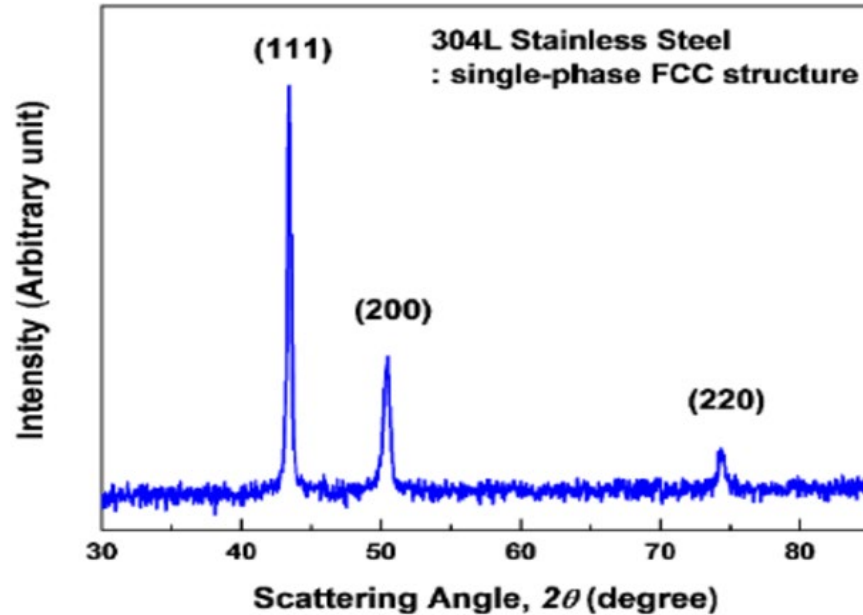


Figure 26. XRD pattern of 304L stainless steel. Source: [22].

3. Scanning Electron Microscopy Analysis of Filaments

The scanning electron microscope was used to investigate the particle reinforcements and bond with the PLA substrate.

a. Analysis of Bronze PLA Filament

The sample's side-cut and cross-sectional cuts were put through the SEM for analysis, and the following images were captured. Figure 27 are images captured by the In-lens detector, thus collecting primarily SE electrons, and therefore the images showed good topographic features and depth. In comparison, Figure 27e. was an image captured by the Everhart-Thornley Detector (ETD).

Figure 27a shows an exposed bronze particle embedded in the PLA matrix. The nearby voids (darker in color) were likely to be previously filled by metal particles that were dislodged during the sample preparation process

Figure 27b. shows the interface between the PLA and bronze of the exposed bronze particle. Some of the PLA matrix could be seen “peeling off” with bits of PLA material still attached to the bronze particle

Figure 27c. is an SEM image of the “semi-circular” metal particle that was observed and discussed during the optical microscope analysis. It is interesting because, in optical imaging, it had seemed like the bronze particle had sheared in half (taking the shape of a “semi-circle”). However, upon further investigation, it was concluded that it was likely due to the sanding/grinding down of the bronze surface, which was subsequently rotated/shifted within the PLA (during sample preparation), and creating the partial void in the process. This is evidenced by the grinding marks on both flat sides of the particle.

Figure 27d. is another image of the bronze particle that was slightly detached from the PLA matrix. The nearby void (darker in contrast) was likely to be previously filled by a metal particle that was dislodged

Figure 27e. is a cross-sectional cut image taken by the EHT detector, imaging the PLA matrix covering and “wrapping” the bronze particles.

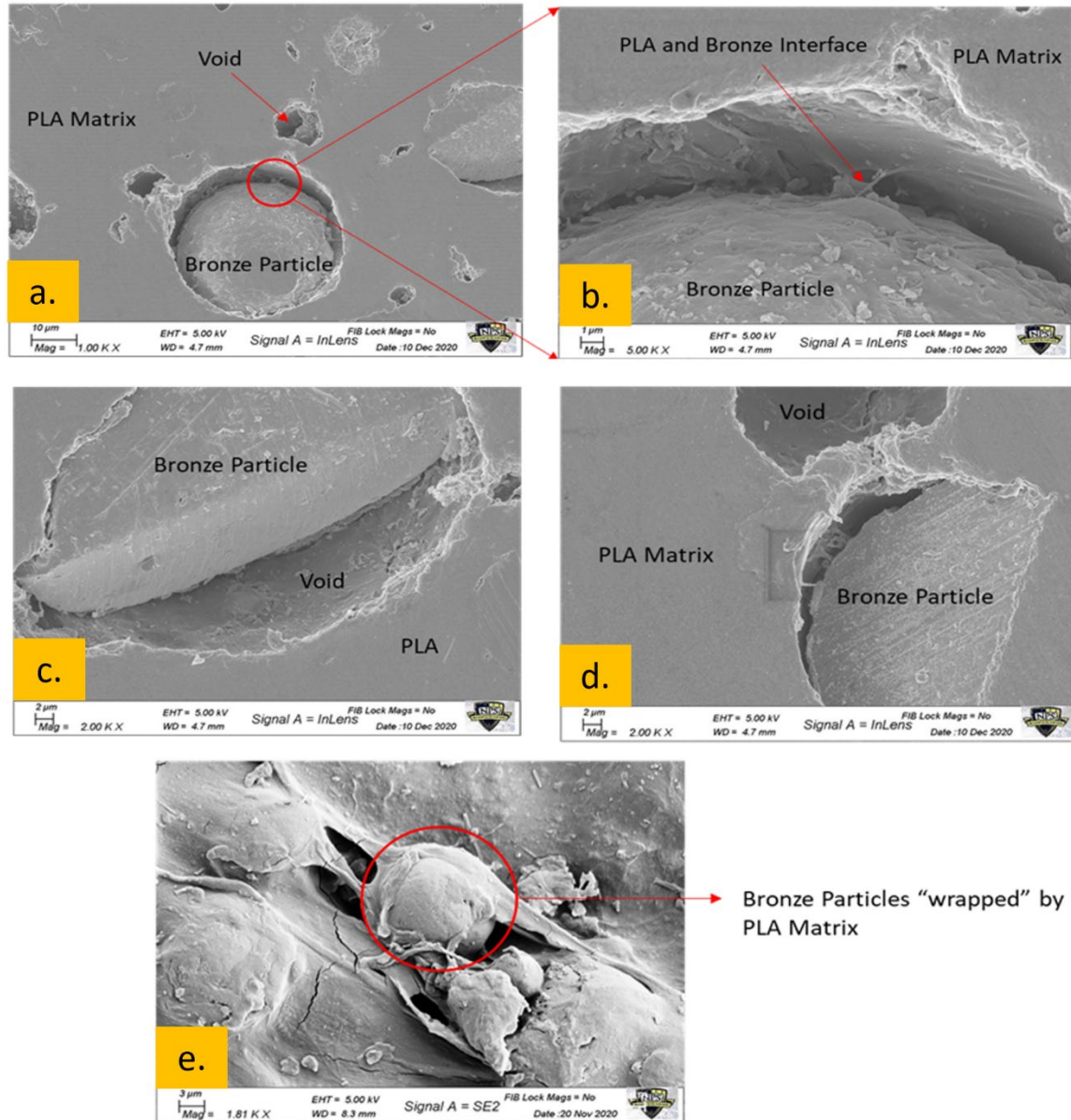


Figure 27. SEM images of bronze PLA filament. (a) side cut of filament at 1000x magnification showing bronze particle and adjacent void in the PLA matrix. (b) detail view at 5000x magnification of the interface between bronze particle and PLA matrix. (c) 2000x magnification detail of bronze particle with evidence of grinding scratches on two surfaces. (d) 2000x magnification of partially dislodged particle. (e) end cut of filament at 1.81Kx magnification, showing particles covered in PLA.

b. Analysis of Stainless Steel Filament

The side-cut and cross-sectional cut of the sample were put through the SEM for analysis capturing the following images. Figure 28a. and 28b. shows the Everhart-Thornley detector image of the cross-sectional cut of the sample. In this cut, it is observed that the PLA matrix mostly covered the metal filler. While in Figure 28c, the side cut sample shown displays a stainless steel particle exposed with a nearby void.

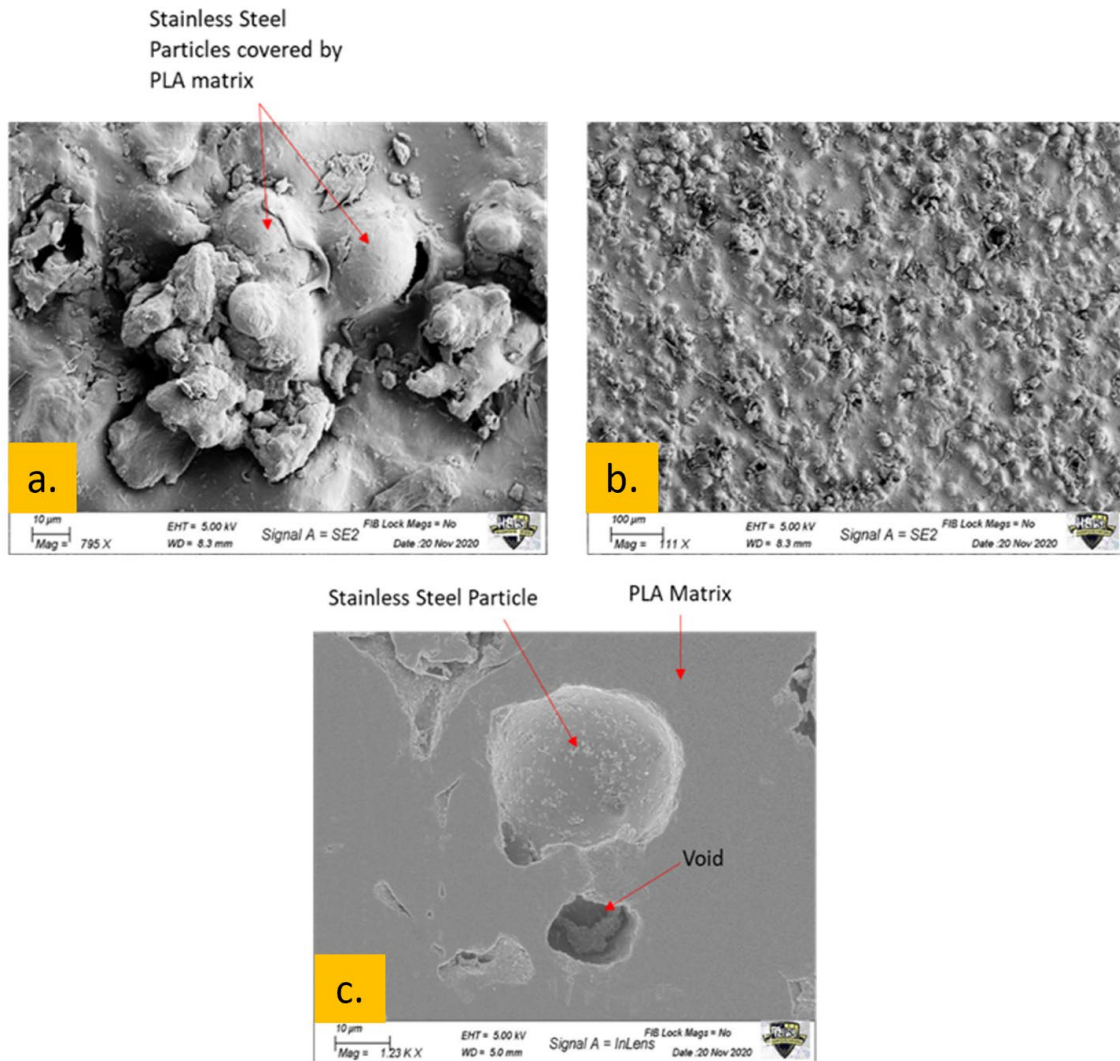


Figure 28. SEM images of stainless steel PLA filament. (a) end cut of filament at 795k magnification. (b) end cut of filament at 111x magnification. (c) side cut of filament showing reinforcement particle and void in the PLA matrix.

4. EDS Analysis of Bronze PLA Filament

From the XRD experiment, the basic elements such as copper and tin were identified as metal fillers in the PLA matrix. The elements: copper, tin, carbon, and oxygen were selected for EDS compositional analysis. The overall EDS spectrum for the bronze PLA composite is shown in Figure 29 (end-cut) and Figure 30 (side-cut). It contains the peak energies for the various identified elements and the respective intensity counts. The palladium detected was due to the sputter coat, and hence it was not explicitly labeled.

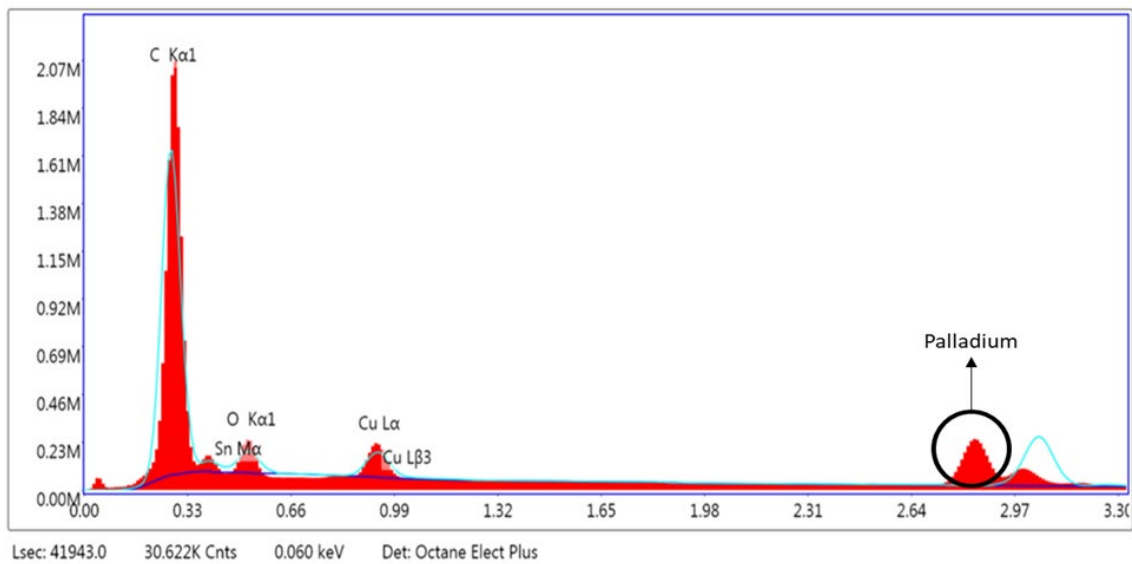


Figure 29. Bronze PLA filament end-cut EDS spectrum.

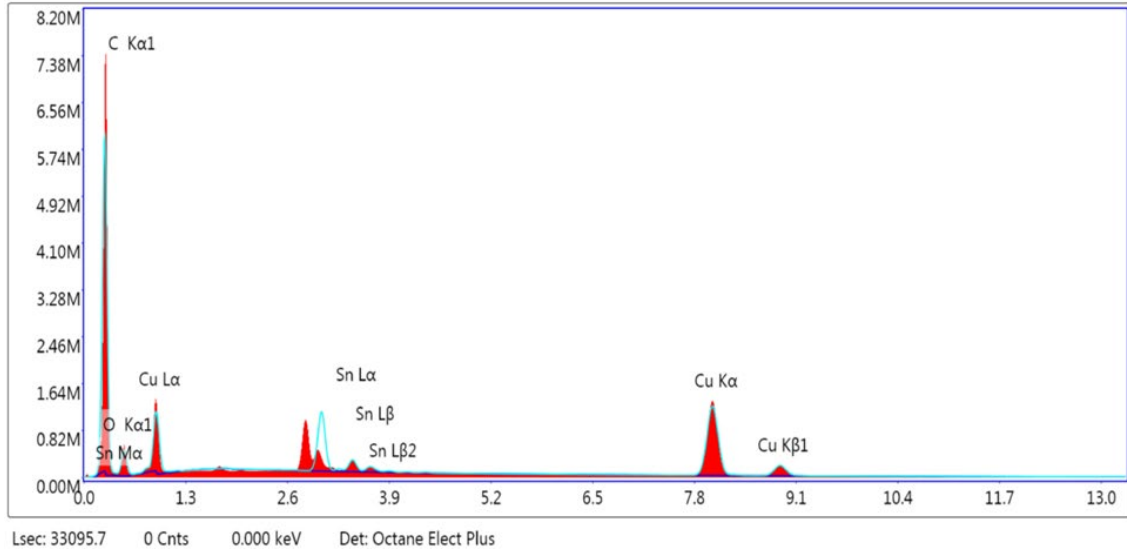


Figure 30. Bronze PLA filament side-cut EDS spectrum.

The following selected sample surfaces were analyzed to determine the elemental type and percentage composition. For the end-cut, Figure 31a shows the elemental overlay for atomic concentration accounting for the unique X-ray energies emitted by the following elements: carbon: 71%, copper: 12%, oxygen: 10%, and tin: 7%. Figure 31b shows the elemental overlay of the side-cut accounting for the unique X-ray energies emitted by the following elements: carbon: 64%, copper: 26%, oxygen: 5%, and tin: 5%.

The approximate elemental composition is an indication that the sample is primarily dominated by PLA (a more prominent presence of carbon detected). At the same time, the remaining elements are copper and tin, which comprise bronze compounds. EDS analysis also confirmed the element/compound present in the sample as predicted by XRD analysis. Bronze particles were detected in the side-cut sample, as shown by the fully rounded spheres with good color contrast in Figure 31b. In the cross-sectional cut, as shown in Figure 31a, the bronze particles were essentially covered by the PLA; hence fewer Cu X-rays were detected.

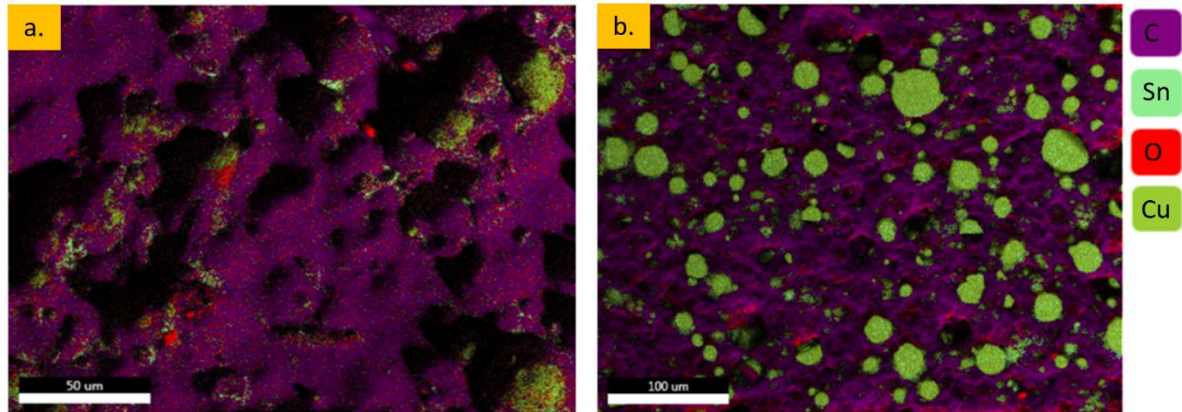


Figure 31. (a) End-cut section of bronze PLA filament showing particles covered with PLA whose primary constituent is carbon. (b) Side-cut section showing exposed bronze particles evidenced by the copper circles.

The elements identified were analyzed for % composition, and colored images showed the contrast between the brighter and darker regions, with the brighter spots identified as the presence of the identified element. Figure 32 (end-cut) and Figure 33 (side-cut) show the elemental contrast of carbon, tin, copper, and oxygen.

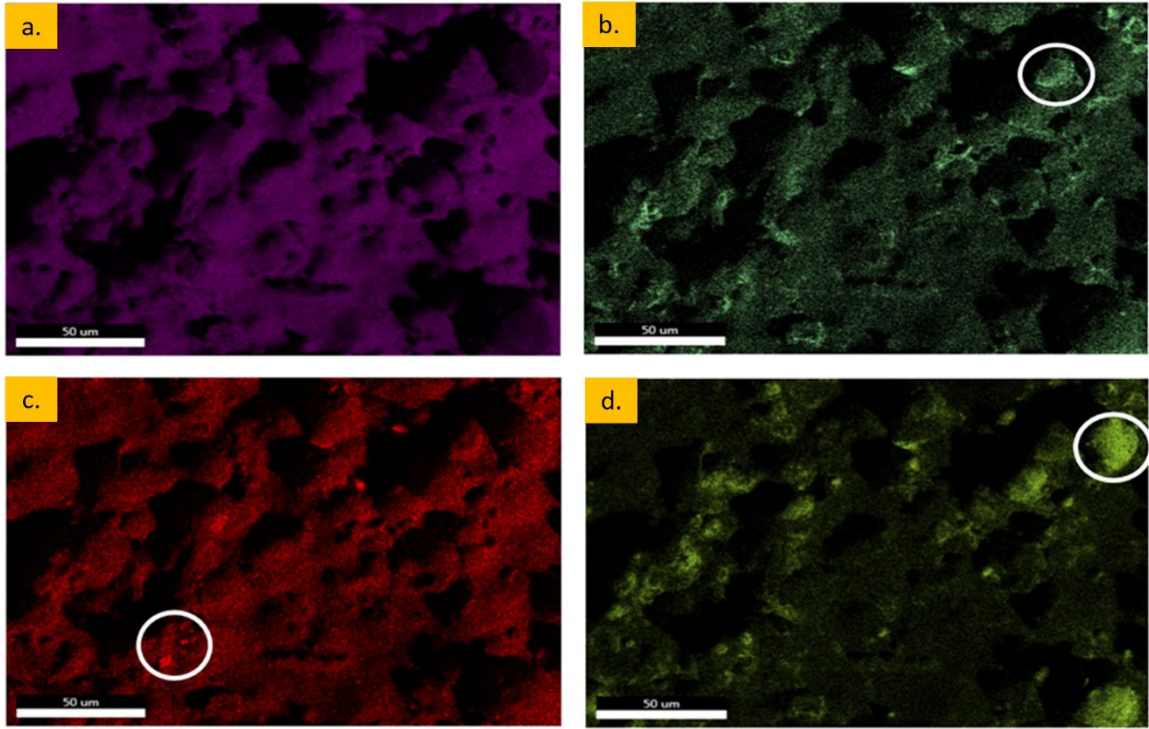


Figure 32. EDS elemental maps for bronze PLA filament (end-cut). (a) carbon, (b) tin, (c) oxygen, (d) copper.

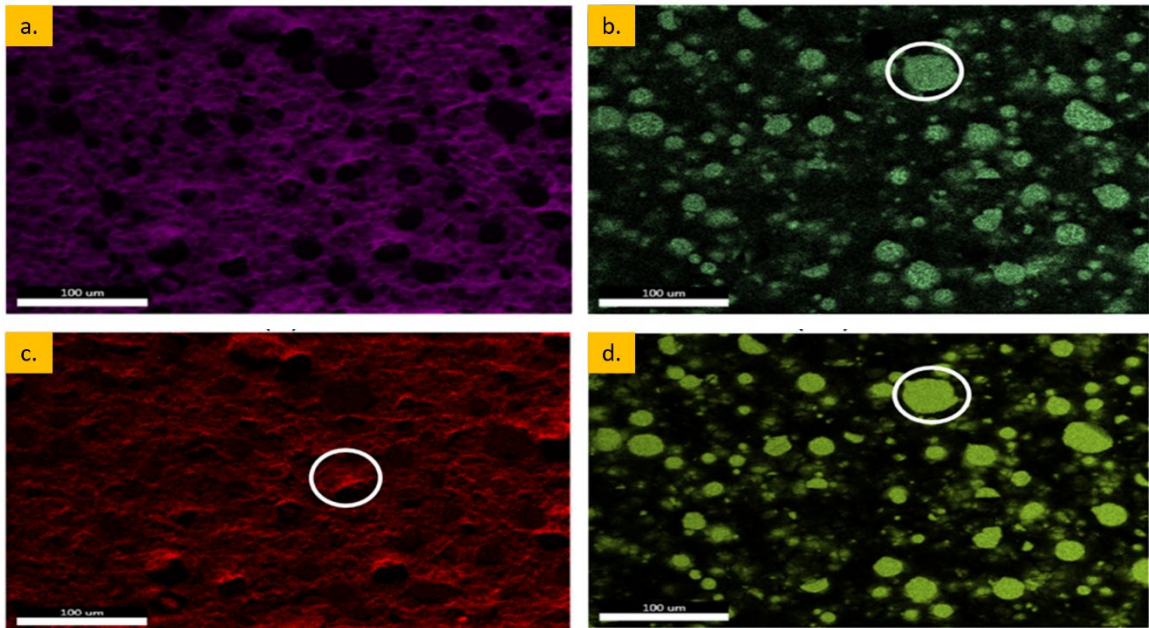


Figure 33. EDS elemental color contrast for bronze PLA filament (side-cut). (a) carbon, (b) tin, (c) oxygen, (d) copper.

B. NANOSCALE MECHANICAL PROPERTIES OF FILAMENTS

The nanoindentation machine was used to test the side cut orientation of the bronze PLA sample. Two batches were created with 21 test points each, one batch for PLA regions, and the other 21 were individual bronze particles.

The test points in the PLA region were chosen to be away from bronze particles and voids. An effort was made to ensure the sample region had minimal polishing scratches. The average modulus of elasticity was determined to be 4.396 ± 0.668 GPa, higher than the published value of 3.5 GPa for purely PLA [23]. This result is as expected due to the bronze particle reinforcements.

The modulus of elasticity for bronze is expected to be around 100 GPa [24]. None of the 21 sample locations came close to the expected value. Furthermore, there was a large standard deviation of 17% for the bronze locations. In the results, there appears to be a bimodal distribution. This data was separated into two categories based on maximum indentation depth in Table 4. The first group consisted of depths between 100–150 nm. The second data set was the remaining locations. With this separation, it was found that the first group had an average of 38.99 GPa and 6.01 GPa for group 2. As seen in the corrected Table 4, the standard deviation was improved for both groups. The significant difference between the two distributions is better conveyed in the load distribution curve in Figure 34.

Group one has higher modulus values corresponding to the shallower indentation depth. This is a more accurate representation of the bronze particles; however, these modulus values are less than half of the expected value. The most likely contributing factor to this behavior is that the surrounding PLA cushions the bronze particles in group 1. This will cause some of the applied force to be absorbed by the surrounding PLA. The machine would have a falsely large displacement due to some of the strain being within the PLA and not carried by the bronze particle. In the group 2 results, it appears the entire particle is slipping or otherwise being displaced by the indenter into the PLA matrix with little resistance. Hence, the actual metal particles are not physically penetrated by the indenter, so the measurements are not an accurate representation of the metal particulate's properties.

Table 4. Bronze PLA bimodal data separation

Bronze Particles Group 1					Bronze Particles Group 2				
Location	Max Modulus	Max Hardness	Max Disp	Max Load	Location	Max Modulus	Max Hardness	Max Disp	Max Load
#	Gpa	Gpa	nm	mN	#	Gpa	Gpa	nm	mN
6	55.707	3.714	107.703	0.966	1	7.031	0.223	439.609	0.958
10	41.18	2.759	126.121	0.953	2	4.851	0.186	493.659	0.964
11	36.666	2.87	127.18	0.952	3	9.986	1.132	230.838	0.961
12	30.285	2.113	146.866	0.95	4	8.065	0.654	285.836	0.963
14	31.604	2.168	144.756	0.954	5	8.181	0.364	350.543	0.948
15	44.416	3.368	116.554	0.965	7	4.11	0.223	466.959	0.959
16	35.24	3.261	123.101	0.953	8	4.546	0.204	476.937	0.958
17	35.186	2.625	133.488	0.967	9	4.375	0.193	486.96	0.949
20	40.859	2.976	123.201	0.957	13	4.694	0.227	456.047	0.96
21	38.786	3.069	123.142	0.956	18	5.5	0.259	424.721	0.96
					19	4.81	0.191	484.444	0.949
MEAN	39.0	2.9	127.2	0.957		6.0	0.4	417.9	1.0
STD DEV	7.3	0.5	11.9	0.006		2.0	0.3	89.3	0.0

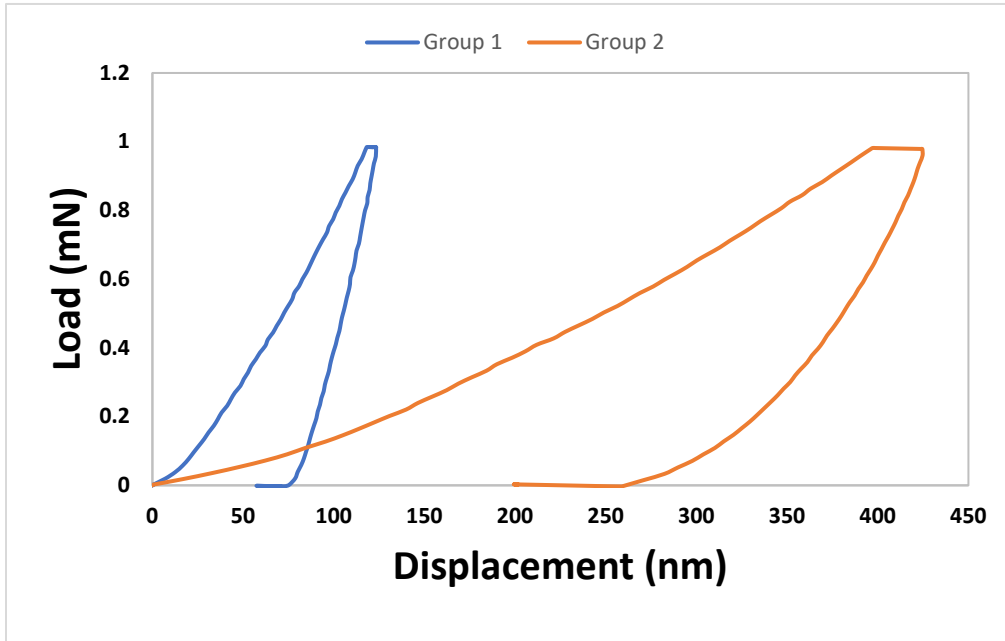


Figure 34. Bronze filament bimodal distribution. Group 1 represents bronze reinforcement particles. Group 2 represents bronze particles that experienced slippage through the PLA matrix during testing.

Additional nanoindentation testing was conducted to compare the characteristics of the raw filament against that of the 3D printed composite samples. Figure 35 shows the nano-hardness loading curves of the PLA regions for the filaments and samples printed with a $\pm 45^\circ$ pattern in the ZXY direction with a 0.2mm layer height for each composite material. There is an increase in the elastic modulus for the printed samples in both composites compared to the raw filaments. This increase in elastic modulus is evidenced by the shift to the left of the curve.

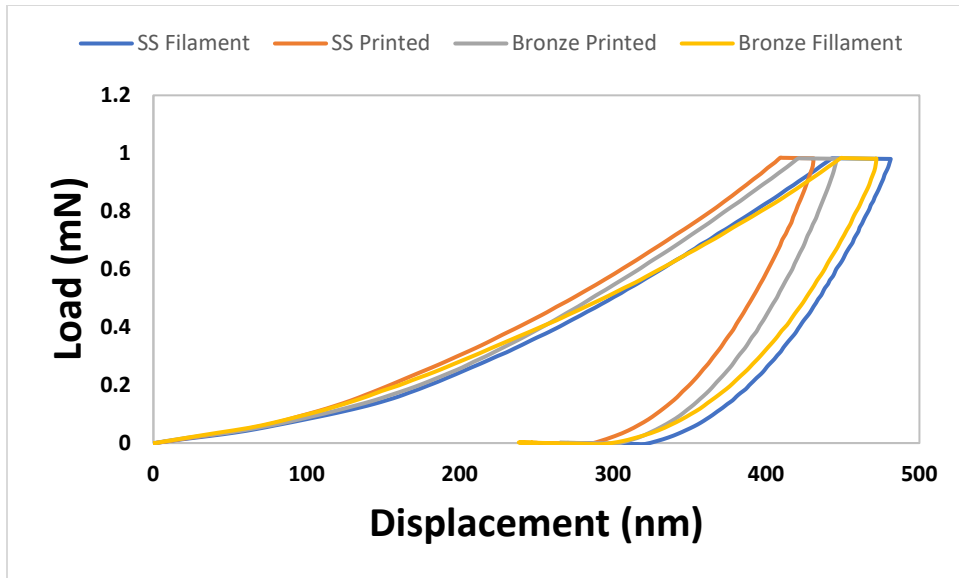


Figure 35. Nano-hardness loading curves for PLA regions of 3D printed composites and composite filaments.

In Figure 36, the nanoindentation testing of the individual metallic reinforcement particles for each composite material is shown. Due to the higher elastic modulus of stainless steel, it is expected that the particles would yield higher results compared to the bronze samples. This expected trend is seen in the raw filaments tested; however, after printing, the differences between the two become negligible. The results of nanoindentation are displayed in Table 5.

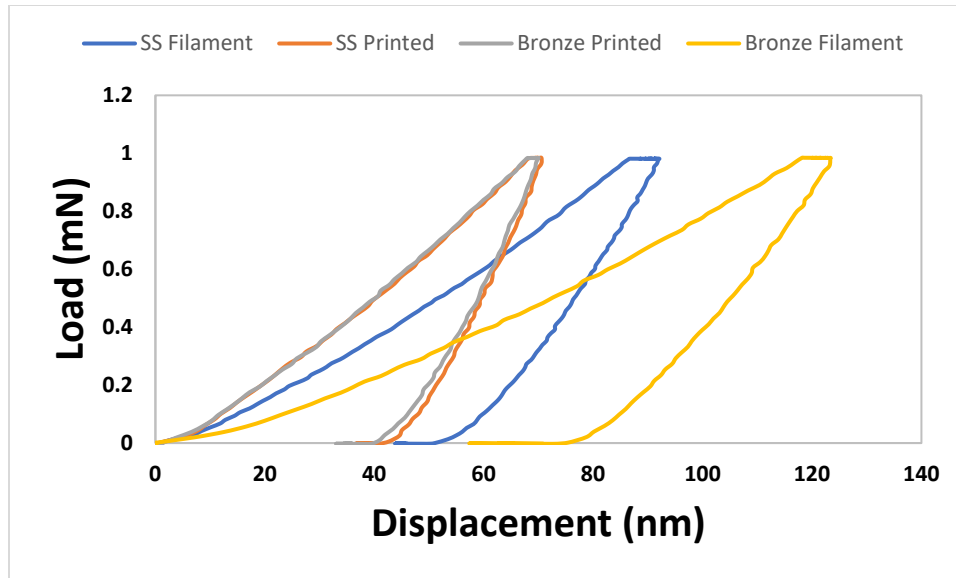


Figure 36. Nano-hardness loading curves for metallic reinforcement particles of 3D printed composites and composite filaments.

Table 5. Nanoindentation test results.

Material	Modulus (Gpa)	STD Dev (%)	Hardness (Gpa)	STD Dev (%)	Disp (nm)	STD Dev (%)	Load (mN)	STD Dev (%)
PLA:SS filament	4.43	0.37	0.211	0.02	476.0	24.3	0.963	0.003
PLA:SS printed	5.65	0.19	0.262	0.02	420.2	9.8	0.957	0.006
PLA:Bronze filament	4.40	0.67	0.217	0.04	471.3	37.9	0.957	0.008
PLA:Bronze printed	5.49	0.97	0.237	0.04	444.7	46.5	0.957	0.007
SS: filament	64.1	23.8	4.3	1.74	112.6	42.1	0.967	0.004
SS: printed	124.6	39.6	7.9	0.64	71.4	5.1	0.965	0.002
Bronze: filament	39.0	7.3	2.9	0.50	127.2	11.9	0.957	0.006
Bronze: printed	121.9	25.2	8.4	2.38	70.2	9.7	0.965	0.004

C. MECHANICAL BEHAVIOR OF 3D PRINTED COMPOSITES

1. Compression Testing

Tests were performed for the bronze and stainless steel reinforced PLA composites to determine the efficacy of each material for load-bearing applications in compression following ASTM D695. In total, 60 specimens of each material comprised of various print patterns, build directions, and layer heights were tested.

The specimens were tested until visible cracking occurred to gain insight into the overall toughness of the composite in each print configuration. Three different patterns of

failure were observed repeatedly, as depicted in Figure 37. The most common failure is inter-layer separation. This type of failure occurred in both XYZ and ZXY directions. There was vertical splitting between layers in the XYZ printed samples, as seen in Figure 37b. The splitting occurred horizontally between layers in the specimens printed vertically or in the ZXY direction (Figure 37c). This layer separation results from the tensile forces due to the buckling of the specimen under load. The third and less common mode of failure is seen in Figure 37a. This failure type is a shearing failure in a plane 45 degrees from the axis of applied force.

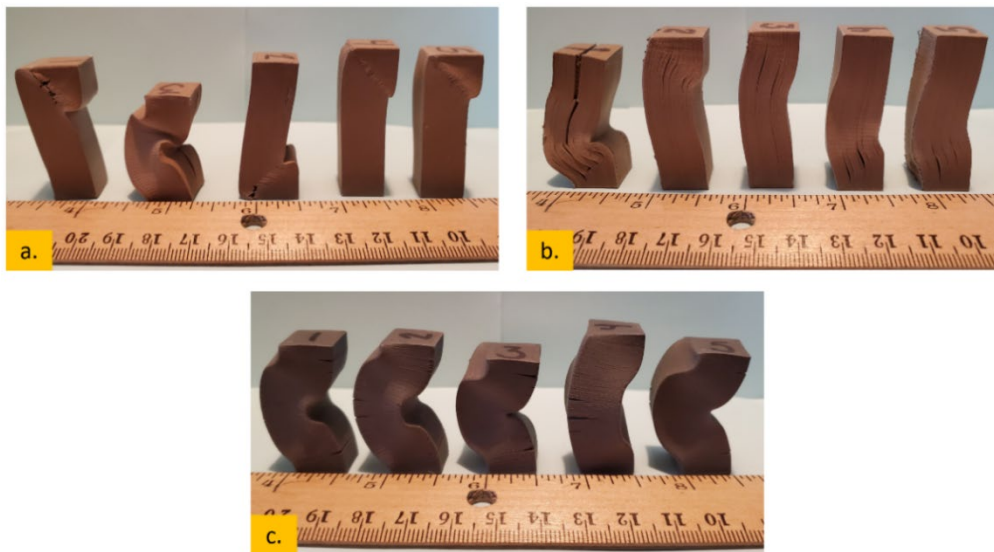


Figure 37. PLA composite failure mechanisms with 0.2 mm layer heights. (a) Bronze PLA sample with 90° line pattern printed in XYZ direction. (b) Bronze PLA sample with $\pm 45^\circ$ lines printed in XYZ direction. (c) Stainless steel PLA sample with $\pm 45^\circ$ lines printed in ZXY direction.

a. Compression Test Results

In both the $\pm 45^\circ$ lines and the concentric infill patterns, the ZXY build direction provided improved compression test results over the XYZ direction. For the $\pm 45^\circ$ line pattern, the two build directions did not display a noticeable difference in ultimate compressive strength; however, the overall toughness of the ZXY pattern was improved,

as seen in Figure 38a. This same trend was seen with the concentric pattern, but the improvement in toughness had significant gains, as displayed in Figure 38b.

It was expected that the stainless steel reinforced PLA would perform better than bronze under compression due to the superior mechanical characteristics of stainless steel. Across all samples, stainless steel showed a significant improvement in ultimate compressive strength (Figure 38d-38f). In the previous section, the 0.1mm layer height consistently performed better than the 0.2mm layer height. Looking at Figure 38a, one will notice this pattern was reversed for the $\pm 45^\circ$ line steel-reinforced pattern. The reason for this difference will be explored in the following sections. Figure 39 conveniently summarizes the effects each test specimen had on the compressive modulus of elasticity.

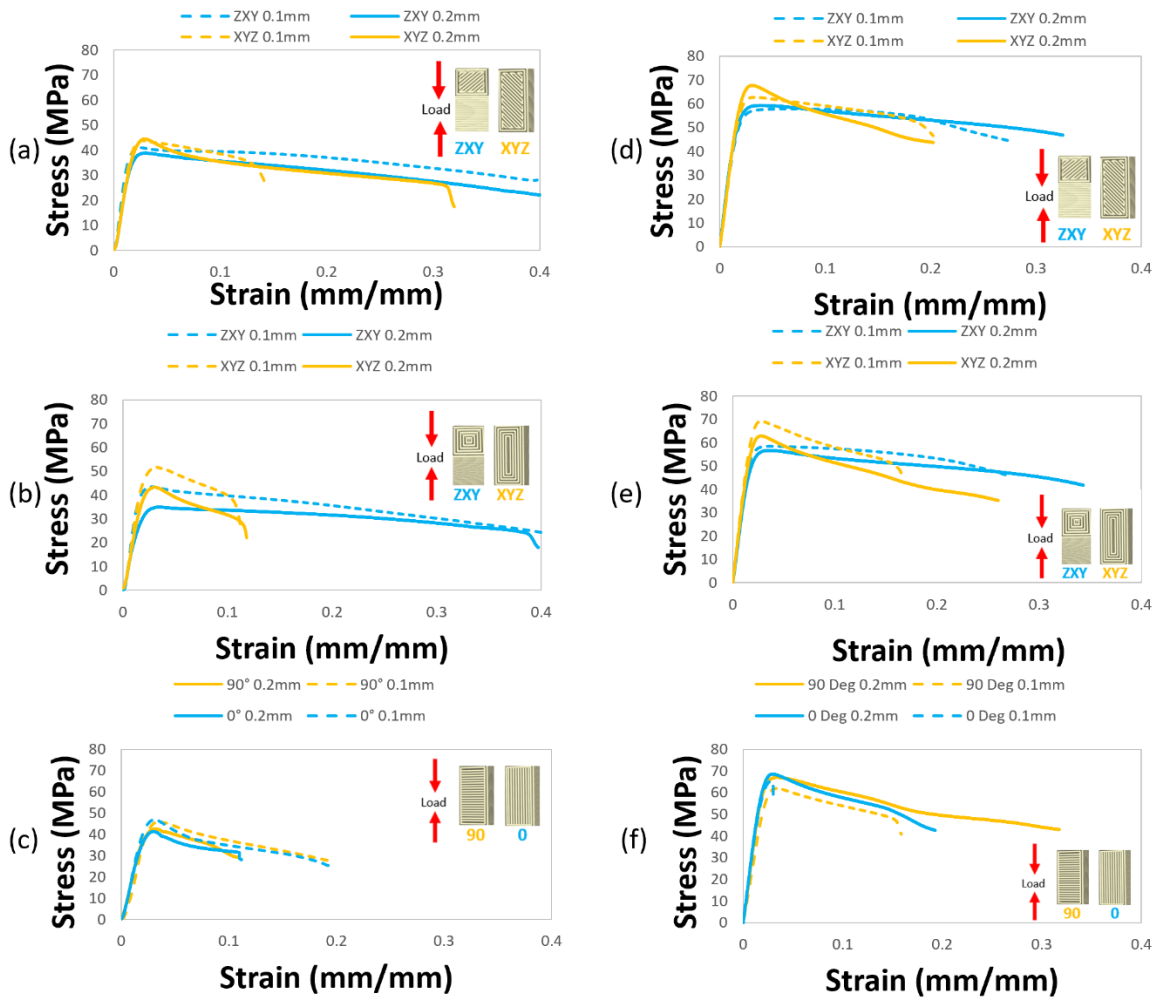


Figure 38. PLA composite compression test results. (a) Bronze $\pm 45^\circ$ line pattern, (b) Bronze concentric infill pattern, (c) Bronze 0° and 90° line infill patterns. (d) Stainless steel $\pm 45^\circ$ line pattern, (e) Stainless steel concentric infill pattern, (f) Stainless steel 0° and 90° line infill patterns

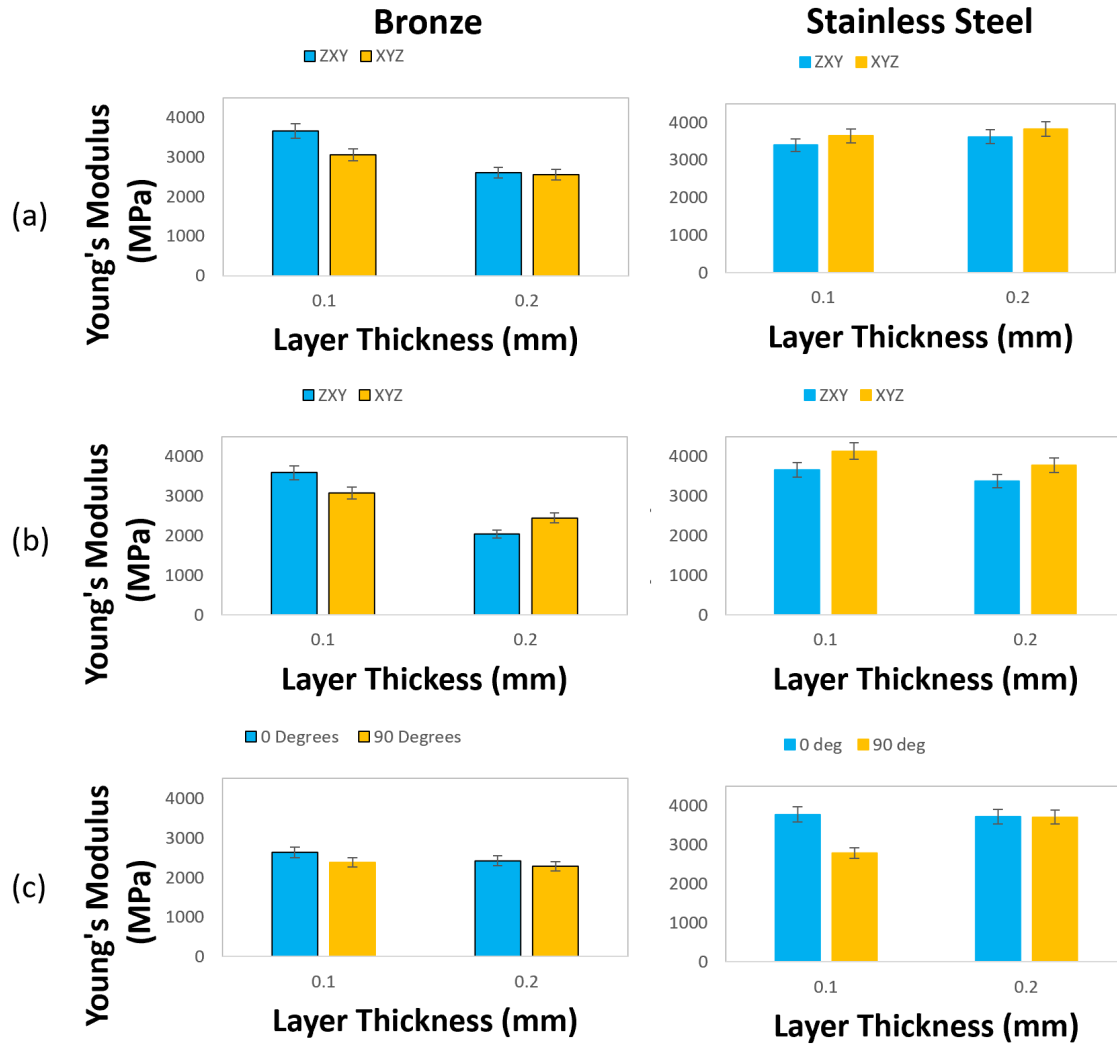


Figure 39. Bronze and stainless-steel PLA composite compression test results summary for Young's Modulus. (a) $\pm 45^\circ$ line pattern, (b) Concentric infill pattern, (c) 0° and 90° line infill patterns.

2. Tensile Testing

Tests were performed for the bronze and stainless steel reinforced PLA composites to determine the efficacy of each material for load-bearing applications in tension following ASTM D638. Two infill print patterns were chosen based on the results of the compression tests. The concentric and $\pm 45^\circ$ patterns performed similarly in compression, so it was decided, based on limited remaining material, only to choose one pattern. The concentric pattern was not tested because, in the gauge length of the test specimen, it is

effectively a series of lines. Therefore, the second test pattern was the 0° line pattern. In total, 20 samples were tested (5 for each pattern), all of which used a layer height of 0.1 mm.

In the case of both the ±45° and 0° line patterns, the bronze and stainless steel performed quite differently under tension. As anticipated, due to the higher elastic modulus of stainless, the ultimate tensile strength (UTS) was greater than that of the bronze reinforced PLA. It was expected that the 0° lines would have improved performance under tension because the print beads are in the direction of the applied force. This pattern displayed significant improvements in UTS for the stainless steel PLA; however, the difference in UTS due to the infill pattern was negligible for the bronze PLA. In Figure 40, the average stress-strain curves for each test are summarized. While bronze reinforced PLA had a significantly lower UTS, the composite had improved ductility over the stainless steel reinforced PLA. The brittle failure of stainless steel PLA is displayed in Figure 41a. The bronze PLA showed visible signs of ductile failure, evidenced by the horizontal stretch marks on the sample's surface in Figure 41b.

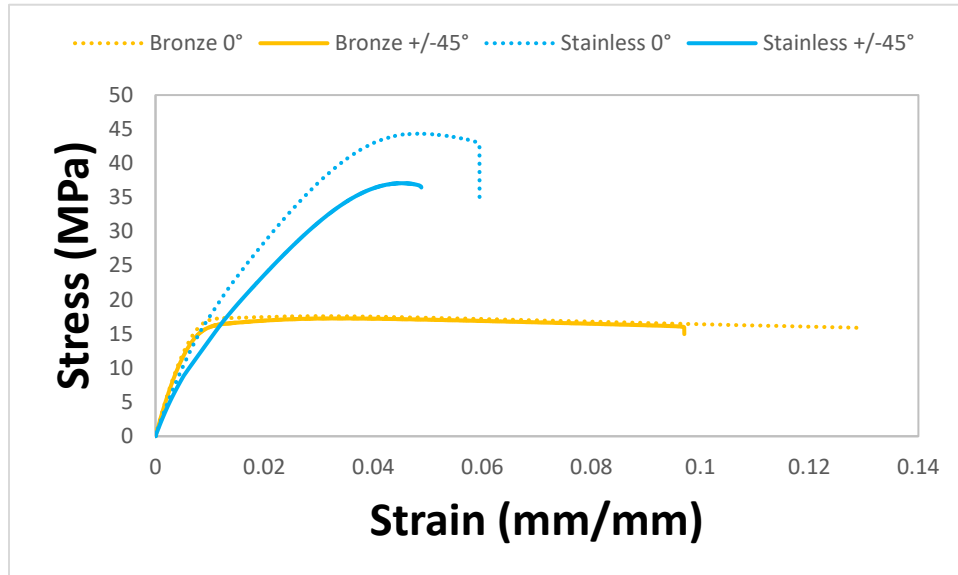


Figure 40. Tensile test summary for bronze and stainless steel PLA printed with ±45° and 0° lines and a layer height of 0.1 mm. Data is representative of the average of the five samples from each test sample.

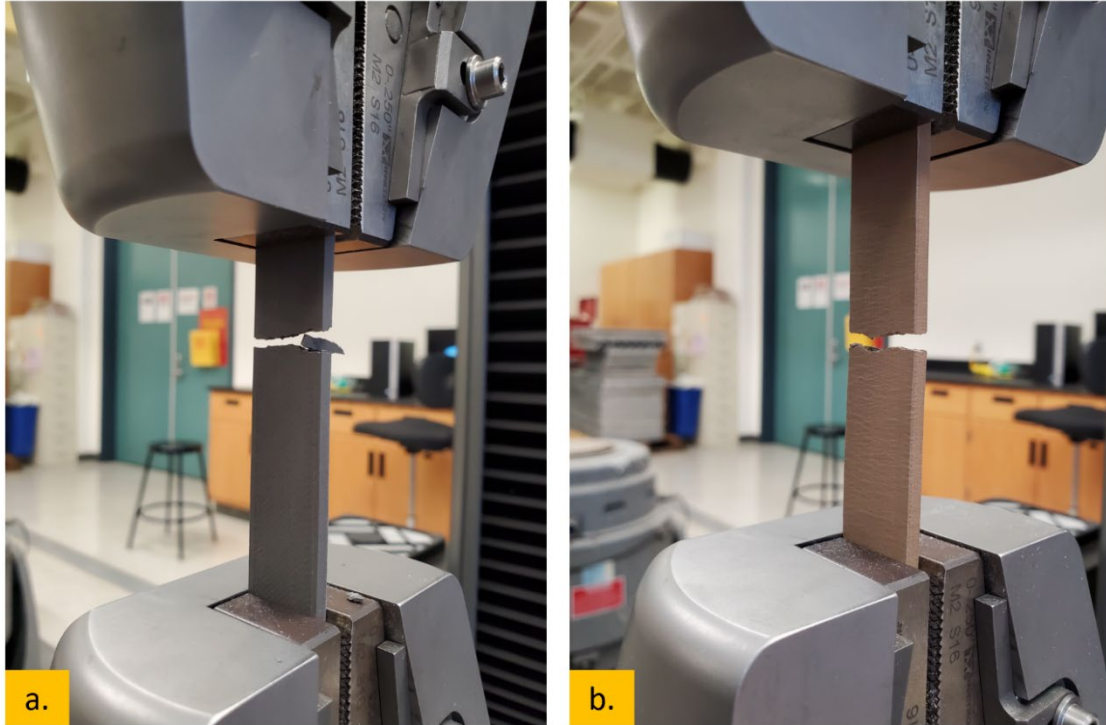


Figure 41. Modes of failure of PLA composites printed with $\pm 45^\circ$ lines under tensile loading. (a) Brittle failure of stainless steel PLA. (b) Ductile failure of bronze PLA.

3. Analysis of Printed Specimen Particulate Concentration

With the raw filaments characterized and theoretical composite material strength properties calculated, the printed samples were characterized. The purpose of this is to see what impact the 3D printing process has on the final sample.

Figures 42–43 and 45–46 illustrate the image processing steps taken using Image J software in the following sections. In each of these figures, image (a) is the 2.5x magnification image converted to 8-bit. Image (b) is the threshold adjustment to account for only the metal reinforcement particles. Image (c) is composed of only reinforcement particles and associated area fractions. Image (d) is the threshold adjustment to account for the porosity. Image (e) displays only the porosity and related area fraction

a. ***Optical Imaging of Stainless Steel $\pm 45^\circ$ Pattern Printed in the ZXY direction***

Optical microscopy images were captured at a minimum magnification of 2.5x to calculate the area/volume fraction of reinforcement material. This magnification was chosen to have a sufficient overall area to ensure an accurate representation of reinforcement concentration. The images were processed as seen in Figure 42, and the following volume fractions were found for stainless steel PLA with a layer height of 0.2mm: stainless steel particles-12.2%, porosity-15.1%, and the remaining 72.7% comprised of the PLA matrix.

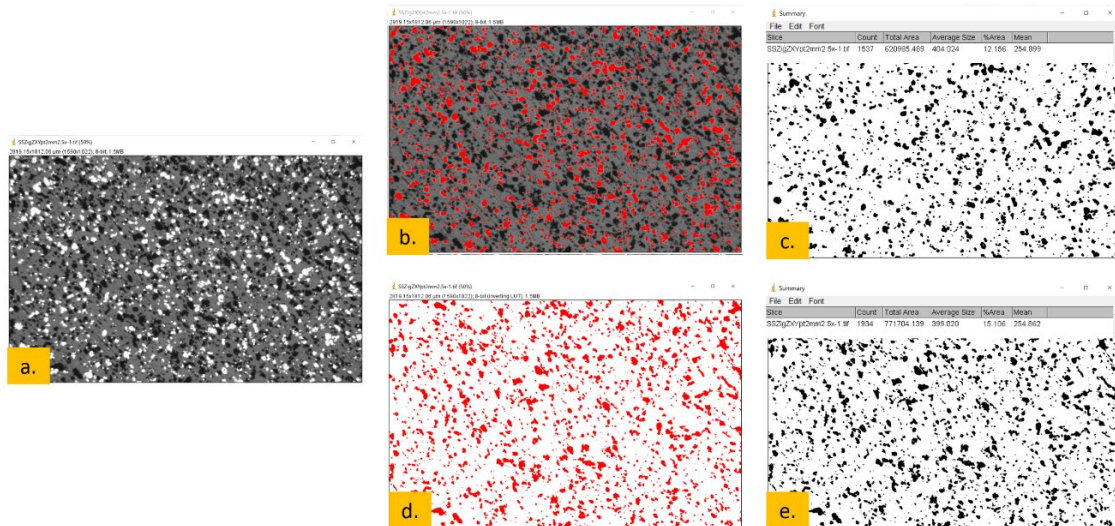


Figure 42. Image processing of stainless steel PLA $\pm 45^\circ$ lines printed in the ZXY direction with 0.2mm layer height.

The concentration of particles in Figure 43 was calculated in the same way as the previously calculated 0.2mm sample. The decrease in reinforcement particles corresponded precisely to the rise in porosity. In the 0.1mm sample, the following area fractions were determined using Image J image processing: stainless steel reinforcement-8.2%, porosity-19.3%, the remaining 72.4% is the PLA substrate.

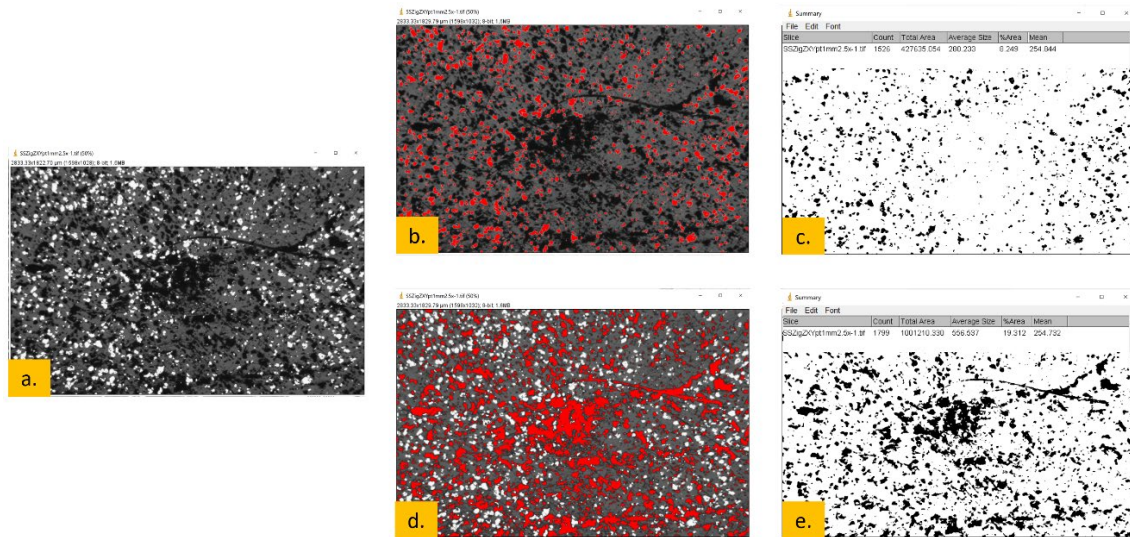


Figure 43. Image processing of stainless steel PLA $\pm 45^\circ$ lines printed in the ZXY direction with 0.1mm layer height.

With the 0.1mm layer height sample, there appeared to be large dark areas lacking in steel particles. The large dark region evidences this in the middle of the 2.5x magnification image in Figure 44a. Upon further investigation with higher magnification (Figure 44b), it is apparent that this dark region is porosity. The voids in the magnified image are roughly the size of the stainless particles. Therefore, it is concluded that they were dislodged either during the printing process or during sample preparation. Due to the increased porosity being located in the center of the sample, it is likely due to the printing process from the print nozzle repeatedly passing over the center with the raster pattern chosen.

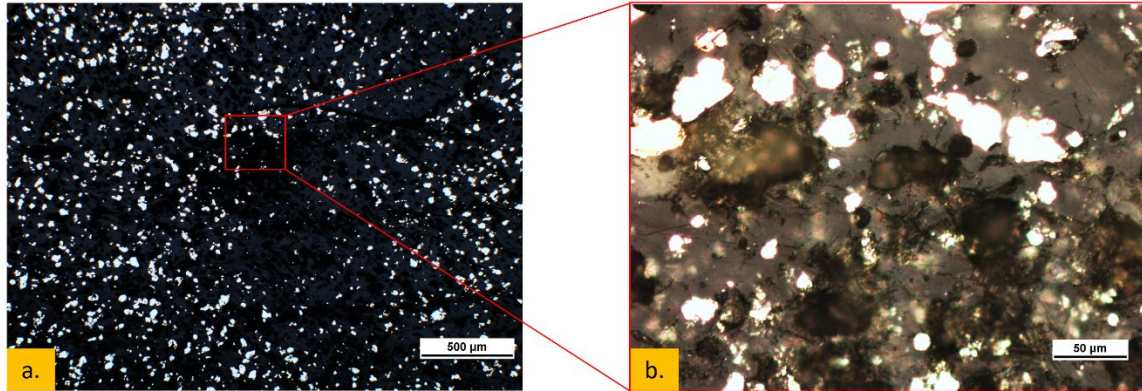


Figure 44. (a) Stainless steel PLA $\pm 45^\circ$ line infill pattern with 0.1mm layer height printed in ZXY direction. (b) Detail view showing the edge of a region of increased porosity.

b. Optical Imaging of Bronze $\pm 45^\circ$ Pattern Printed in the ZXY direction

As with the stainless steel samples in the preceding section, the bronze sample images were processed using Image J at a magnification of 2.5x in Figures 45–46. This magnification was chosen to ensure a large enough area was selected to represent area fraction calculations accurately.

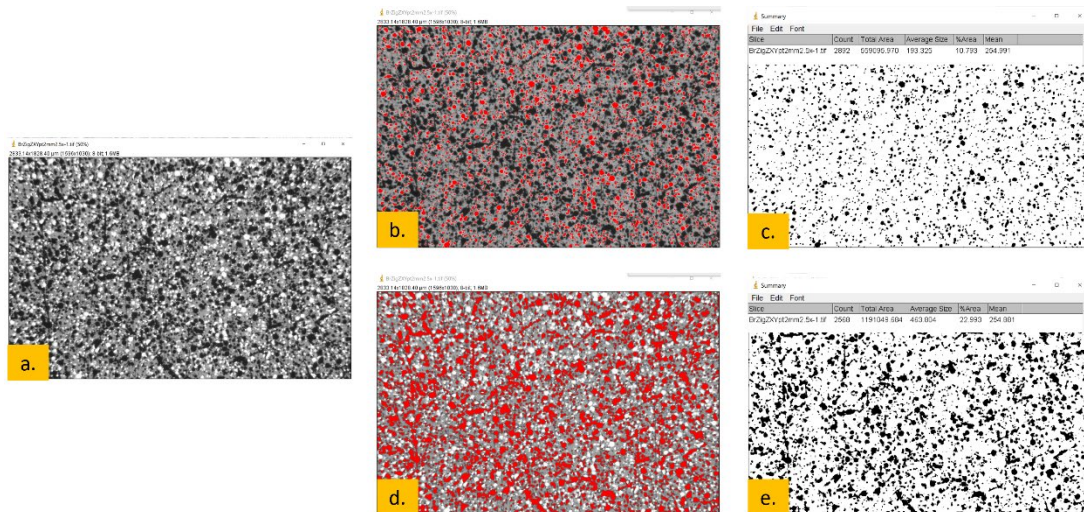


Figure 45. Image processing of bronze PLA $\pm 45^\circ$ lines printed in the ZXY direction with 0.2mm layer height.

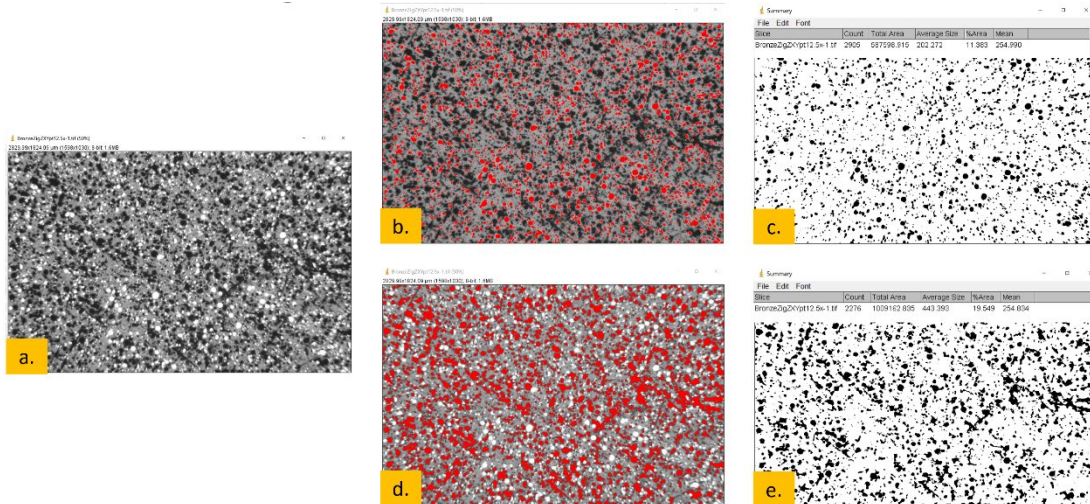


Figure 46. Image processing of stainless steel PLA $\pm 45^\circ$ lines printed in the ZXY direction with 0.1mm layer height.

At first glance, the images of the 0.1mm and 0.2 mm samples above appear the same. Both have a very homogenous mixture of bronze particles and porosity, and they both have nearly identical concentrations of reinforcement particles. Where they differ is the 0.2 mm layer specimen has 7.3% more porosity than its 0.1 mm layer counterpart. This even mixture of porosity is unlike that seen in the stainless steel specimens, where porosity was concentrated in the sample center.

The even increase in porosity across the 0.2mm sample is likely a result of the sample preparation. In Figure 47, a particle can be seen dislodged from the PLA substrate leaving behind a void circled in red. If one looks closely, moving to the right of the void, two indentations can be seen on the surface of the PLA before the particle reaches its resting place, as shown. The bronze particle lies on the surface of the polished plane, as evidenced by the shallow depth of field having the particle in question in focus while the rest of the image is slightly out of focus.

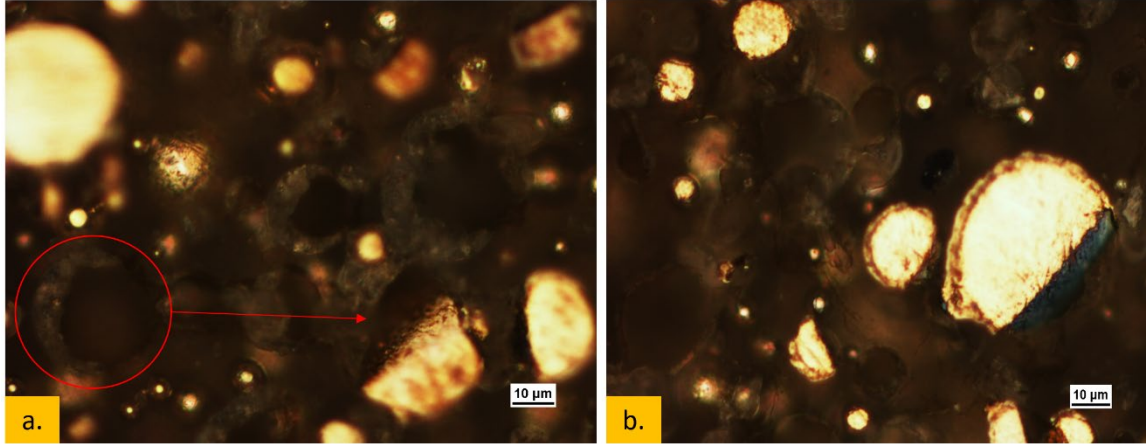


Figure 47. Bronze PLA: $\pm 45^\circ$ lines printed in ZXY direction with 0.1mm layer height. (a) Bronze particle dislodged from PLA matrix and dragged from left to right during sample preparation. (b) Semi-circular bronze particle with polishing scratches on two sides leaving behind a half-circle void.

4. Estimation of Composite Elastic Modulus Based on Volume Fraction

Theoretical values for the composite modulus of elasticity were calculated using the Halpin-Tsai model for the rule of mixtures. This model is intended to estimate the overall modulus of elasticity of a composite based on the volume fraction of reinforcement materials present and their known modulus [25]. The Halpin-Tsai model is designed for reinforcement fibers.

$$E_C = E_M \left(\frac{1 + \xi \eta V_f}{1 + \eta V_f} \right)$$

$$\eta = \frac{\frac{E_f}{E_M} - 1}{\frac{E_f}{E_M} + \xi}$$

$$\xi = \frac{2l}{d}$$

In the above equations, the elastic modulus is represented by the variable E. The subscript “c” represents the overall composite. The subscript “f” describes the reinforcement fiber, while “m” describes the bulk material. The Halpin-Tsai model is

designed for long fiber reinforcements and requires the parameter “ ξ ” to account for fiber geometry. As the value of ξ approaches infinity, the model simplifies to the well-known Rule of Mixtures equation. The inverse rule of mixtures is a lower bound representation and is appropriate when ξ approaches zero [25].

$$ROM: E_C = E_m V_m + E_f V_f$$

$$Inverse\ ROM: E_C = \frac{E_f E_m}{E_f V_m + E_m V_f}$$

In the case of the bronze reinforced PLA, the particles are spherical. The stainless steel particles are more irregular, yet they were approximated as having a spherical geometry. Two calculations were carried out for each composite. The calculations used a 1 to 1 length to diameter ratio representative of a sphere, in which case the value of ξ reduces to 2. The elastic modulus of stainless steel is 193 GPa [26]. The exact type of bronze is unknown; however, the elastic modulus of bronze generally lies between 72 and 137 GPa [24]. For calculations, a lower value of 72 GPa was used. For the PLA matrix, a value of 3.5 GPa was used [23]. The area fraction of each reinforcement was determined using optical images processed using Image J software, as discussed earlier. Due to the homogeneous distribution of the particles in the PLA substrate, it can be assumed that the area fraction can be used as an approximation of the volume fraction. The following equations will show the calculations for the stainless steel and bronze PLA samples printed with a $\pm 45^\circ$ degree pattern in the ZXY direction with a 0.2 mm layer height.

$$\eta_{stainless} = \frac{\frac{193}{3.5} - 1}{\frac{193}{3.5} + 2} = 0.9475$$

$$E_{C-stainless} = 3.5 \left(\frac{1 + 2 * 0.9475 * 0.12156}{1 + 0.9475 * 0.12156} \right) = 3.86149\ GPa$$

$$\eta_{bronze} = \frac{\frac{72}{3.5} - 1}{\frac{72}{3.5} + 2} = 0.8671$$

$$E_{C-bronze} = 3.5 \left(\frac{1 + 2 * 0.8671 * 0.10793}{1 + 0.8671 * 0.10793} \right) = 3.79935\ GPa$$

For comparison, the theoretical values for elastic modulus were also calculated using the inverse Rule of Mixtures model. This model is expected to be less accurate due to the elimination of the geometry factor, ξ .

$$E_{C-stainless} = \frac{193 * 3.5}{193 * 0.72738 + 3.5 * 0.12156} = 4.79725 \text{ GPa}$$

$$E_{C-bronze} = \frac{72 * 3.5}{72 * 0.66214 + 3.5 * 0.10793} = 5.24434 \text{ GPa}$$

The Halpin-Tsai model resulted in theoretical values of elastic modulus that were much closer to the experimentally measured values than the inverse Rule of Mixtures approximation. As expected, the use of the geometry parameter, ξ resulted in results that were much more accurate, and so the Halpin-Tsai model was chosen for remaining theoretical approximations. Table 6 summarizes the remaining Halpin-Tsai calculations compared to the experimental results for bronze and stainless steel specimens.

Table 6. Summary of calculated results compared to experimentally measured results for bronze and stainless steel printed composites with $\pm 45^\circ$ lines built in the ZXY.

Theoretical vs. Experimentally Measured Compressive Modulus of Elasticity				
	Bronze		Stainless Steel	
Layer Height (mm)	0.2	0.1	0.2	0.1
Particle %	10.8	11.4	12.2	8.2
Porosity %	23	15.7	15.1	19.3
PLA %	66.2	72.9	72.7	72.4
Calculated (MPa)	3799.7	3814.4	3861.5	3753.7
Measured (MPa)	2601.4	3663.12	3621.5	3397
% Difference	-31.5	-4.0	-6.2	-9.5

5. SEM Analysis of Layer Thickness Impact on Porosity

The apparent correlation between porosity content and its impact on overall mechanical performance was investigated using SEM analysis. In addition, the interface

between the reinforcement particles and the PLA matrix was an area of focus due to the discovery of dislodged particles and sites of increased porosity found using optical microscopy. Figure 48 shows the surface of a stainless steel reinforced PLA composite printed with a $\pm 45^\circ$ pattern and a 0.2mm layer height. In Figure 48a, there is a seemingly homogeneous distribution of porosity voids across the surface. At higher magnification in Figure 48b, the detail of the interface between a stainless steel particle and the surrounding PLA substrate shows good adhesion between the two materials.

During compression testing, it was found that in the $\pm 45^\circ$ sample of stainless steel PLA, strength suffered as the layer height decreased. Optical images showed increased porosity concentrated toward the middle of the printed sample. The surface of a sample built with a 0.1mm layer height is shown in Figure 49a. It is readily apparent that the porosity does not have the same uniformity across the surface as seen with the 0.2mm layer height. When viewed at increased magnification in Figure 49b, there is a noticeable separation between the stainless particle and the surrounding PLA.

Additionally, there is a crack in the PLA matrix propagating from the steel particle. The difference in thermal conductivity between the two materials is likely the cause of such a phenomenon. With the decreased layer height, the heated nozzle is closer to the previous layers as it makes each pass. This will cause heat to be more readily transferred to the last layer with subsequent nozzle passes. Due to the difference in thermal conductivity between the materials, stainless steel and PLA will absorb and release heat at different rates. The repeated passes of the nozzle in the $\pm 45^\circ$ infill pattern will cause cyclic periods of heating and cooling and thus cyclic thermal expansion and contraction. Figure 49b shows separation between the stainless steel particle and the surrounding PLA due to this difference in thermal conductivity. This would have the additional negative effect of making the stainless steel particle, which was meant to reinforce the composite, act as an area of stress concentration.

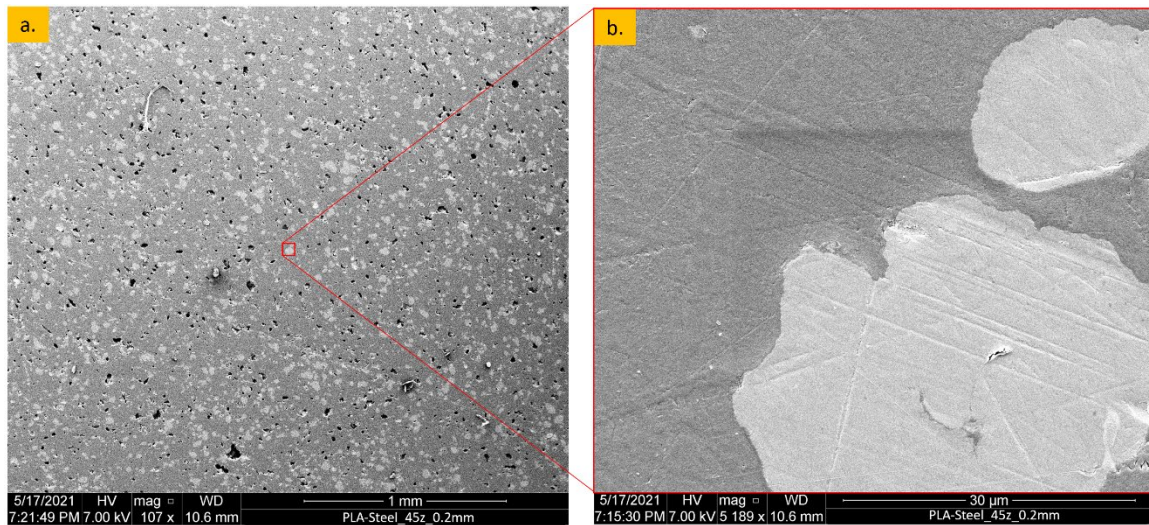


Figure 48. Stainless steel PLA composite printed with $\pm 45^\circ$ line infill pattern in the ZXY direction and a layer height of 0.2mm. (a) 100x magnification showing uniformity of porosity across surface. (b) higher mag image showing good particle to substrate adhesion.

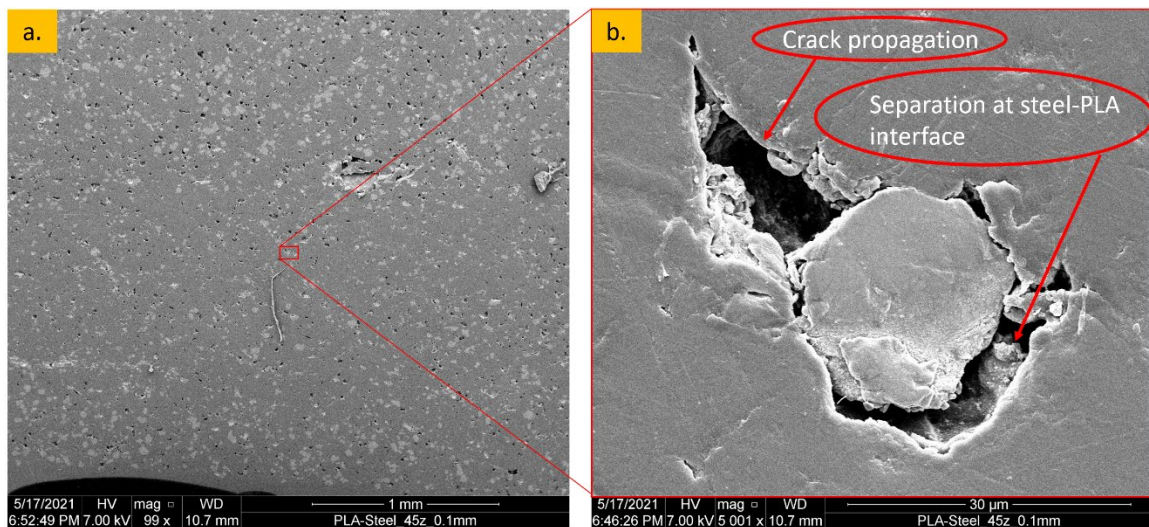


Figure 49. Stainless steel PLA composite printed with $\pm 45^\circ$ line infill pattern in the ZXY direction and a layer height of 0.1mm. (a) 100x magnification showing inconsistent porosity. (b) higher mag image of particle separation and crack propagation due to a difference in thermal conductivity.

The concentric infill pattern of the stainless steel PLA composite was also imaged using the SEM to determine if the correlation between porosity and layer height was pattern

specific. In the $\pm 45^\circ$ pattern, the interface between print beads is indistinguishable except in some outer wall areas. The interface between beads can be made out across nearly the entire surface with the concentric infill pattern. In Figure 50a, the 0.2mm layer height concentric pattern showing the bead interface is displayed. The high magnification image in Figure 50b shows good adhesion between print beads with minimal separation or porosity.

As the layer height was decreased to 0.1mm, the concentric pattern was also found to have increased porosity. Unlike the $\pm 45^\circ$ pattern, where the porosity was due to the particle to substrate separation, the concentric pattern experienced separation between print beads. In Figure 51a significant inter-bead separation is observed. In the detailed view of Figure 51b, the separation is due to PLA contraction during cooling, evidenced by the PLA pulling apart.

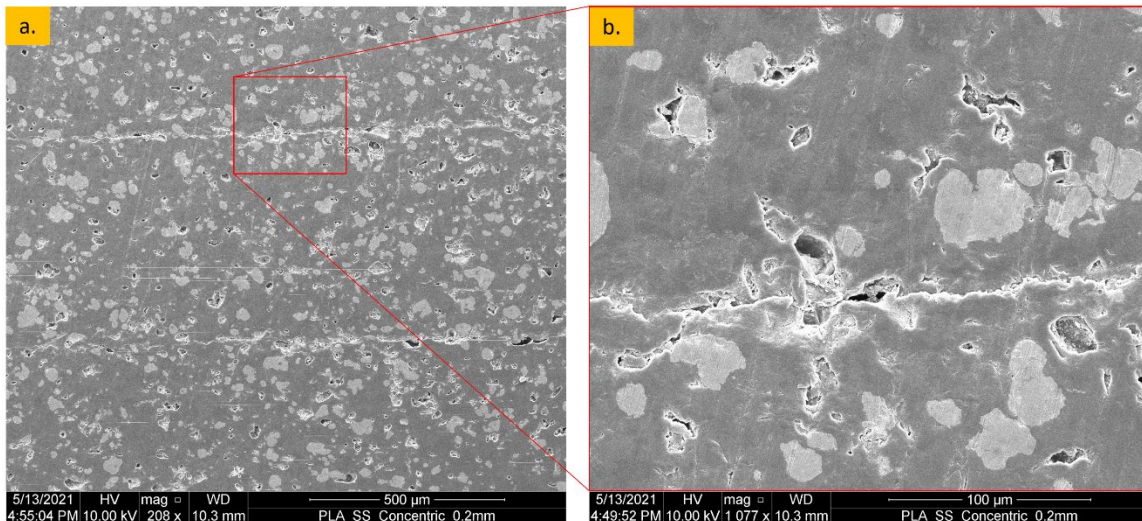


Figure 50. Stainless steel PLA composite printed with concentric infill pattern in the ZXY direction and a layer height of 0.2mm. (a) 200x magnification showing good inter-bead adhesion. (b) 1000x detail of an area of porosity near print bead interface.

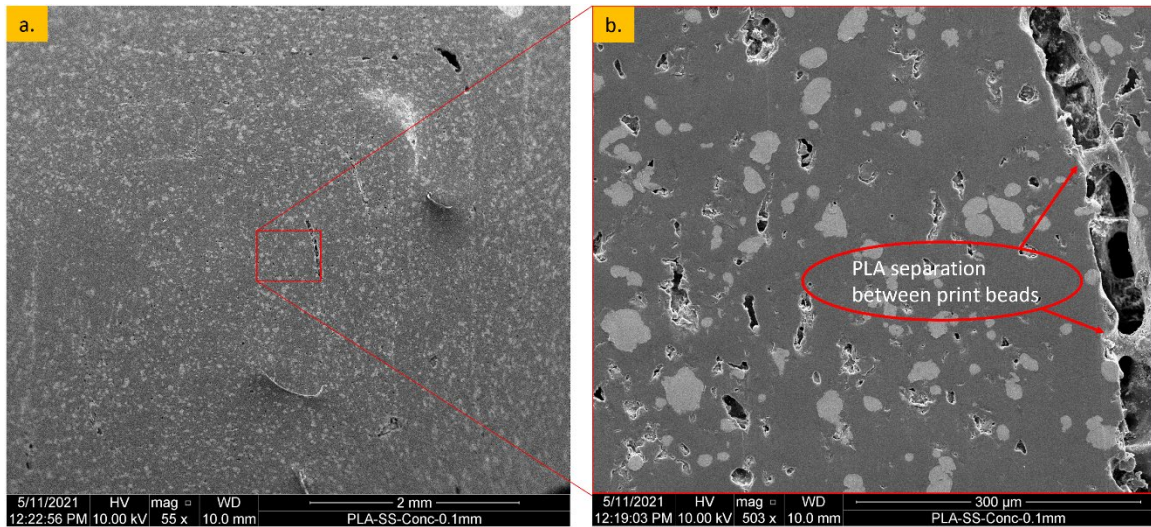


Figure 51. Stainless steel PLA composite printed with concentric infill pattern in the ZXY direction and a layer height of 0.1mm. (a) low magnification showing separation between print beads. (b) detail showing PLA separation at print bead interface.

Samples of bronze reinforced PLA printed with a concentric pattern in the ZXY direction were evaluated to compare with the steel samples. It was found in Figure 52 that the bronze particles did not have the same phenomena of separation between print beads. Instead, the polished surface of the sample had a uniform distribution of particles and porosity, and the interface between print beads was indistinguishable.

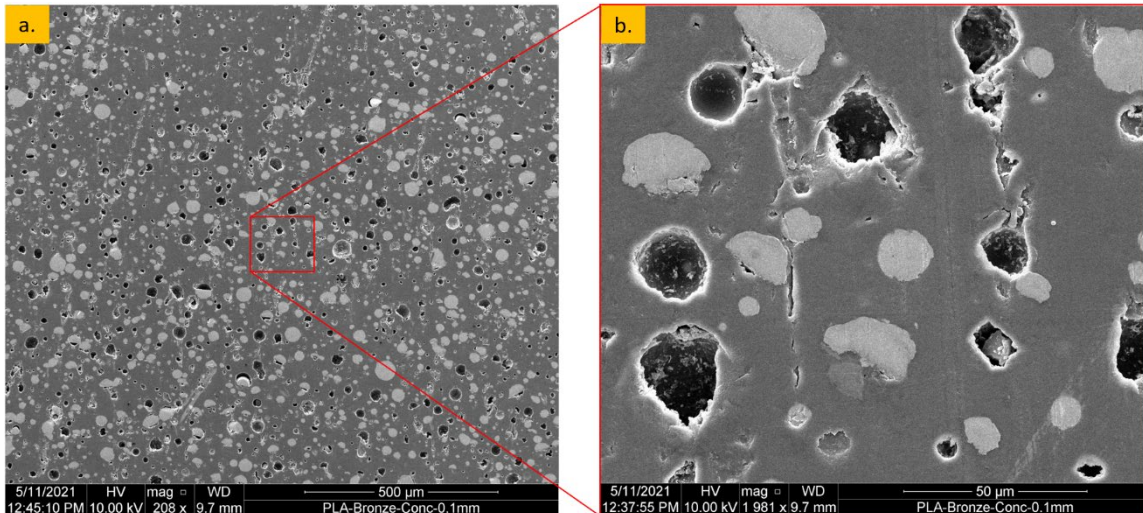


Figure 52. Bronze PLA composite printed with concentric infill pattern in the ZXY direction and a layer height of 0.1mm. (a) low magnification showing the homogeneous distribution of particles and porosity. (b) detail showing porosity and particles with good adhesion with PLA matrix.

It was seen in the compression testing that the majority of the failures occurred between print layers. SEM images were taken of the printed samples without polishing to examine the inter-layer bonding. Figure 53a shows the bronze PLA composite printed with a 0.1mm layer height. There is a significant increase in porosity, inter-bead gaps, and particle agglomeration in this sample compared to the 0.2mm layer bronze sample seen in Figure 53b.

The inter-layer bonding of the stainless steel PLA composite was compared between two different layer heights. Figure 53c displays the 0.1mm layer height, while the 0.2mm height is shown in Figure 53d. While not as severe as the bronze sample, Figure 53c also has inconsistent layer bonding due to layer gaps and voids compared to Figure 53d.

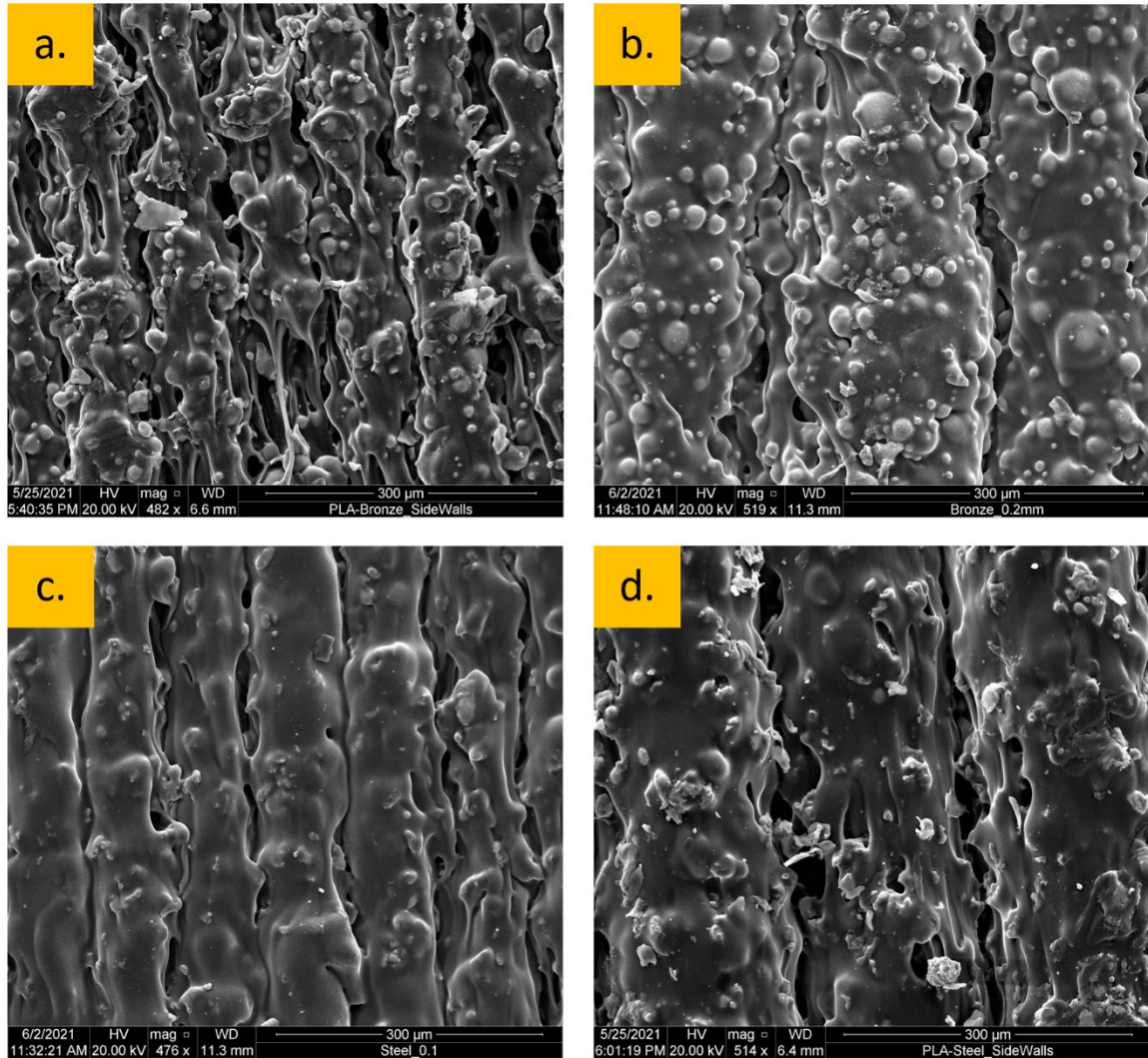


Figure 53. Side images of samples printed in the ZXY direction with concentric infill pattern. (a) bronze PLA with 0.1mm layer height. (b) bronze PLA with 0.2mm layer height. (c) stainless steel PLA with 0.1mm layer height. (d) stainless steel PLA with 0.2mm layer height.

D. ACCELERATED WEATHERING

In shipboard environments, degradation due to both moisture and ultraviolet (UV) exposure can be factors that may be overlooked for material selection. Therefore, to help determine the applicability of 3D printed bronze and stainless steel PLA composites for shipboard applications, they were subjected to 500 hours of accelerated weathering testing and compared to pure PLA samples according to ASTM standards.

Initial dimensional measurements and weights were documented before testing. After 200 hours and finally, after 500 hours, the samples were again weighed. Due to physical deformation, accurate dimensional measurements could not be consistently measured after the initial measurements. Throughout the test, there was neither a gain nor loss in mass. As seen in Figure 54, the purely PLA samples experienced the most significant deformation, followed by the bronze sample. The stainless-steel PLA sample experienced shrinkage but not the same warpage as the other two material types.

While the stainless steel sample appeared resistant to physical deformation, a chalky white appearance was developed on the exposed surface. This appearance was rather subtle after 200 hours and became more prominent by the 500-hour mark, as seen in Figure 55. Intuition would lead one to believe this would be due to the exposure of the stainless steel particles to moisture during the test leading to oxidation of the steel particles. However, the bronze PLA and pure PLA specimens did not experience this development of a chalky white surface. To further investigate the cause of this phenomenon, the samples were examined using a Nikon Epiphot 200 optical microscope.

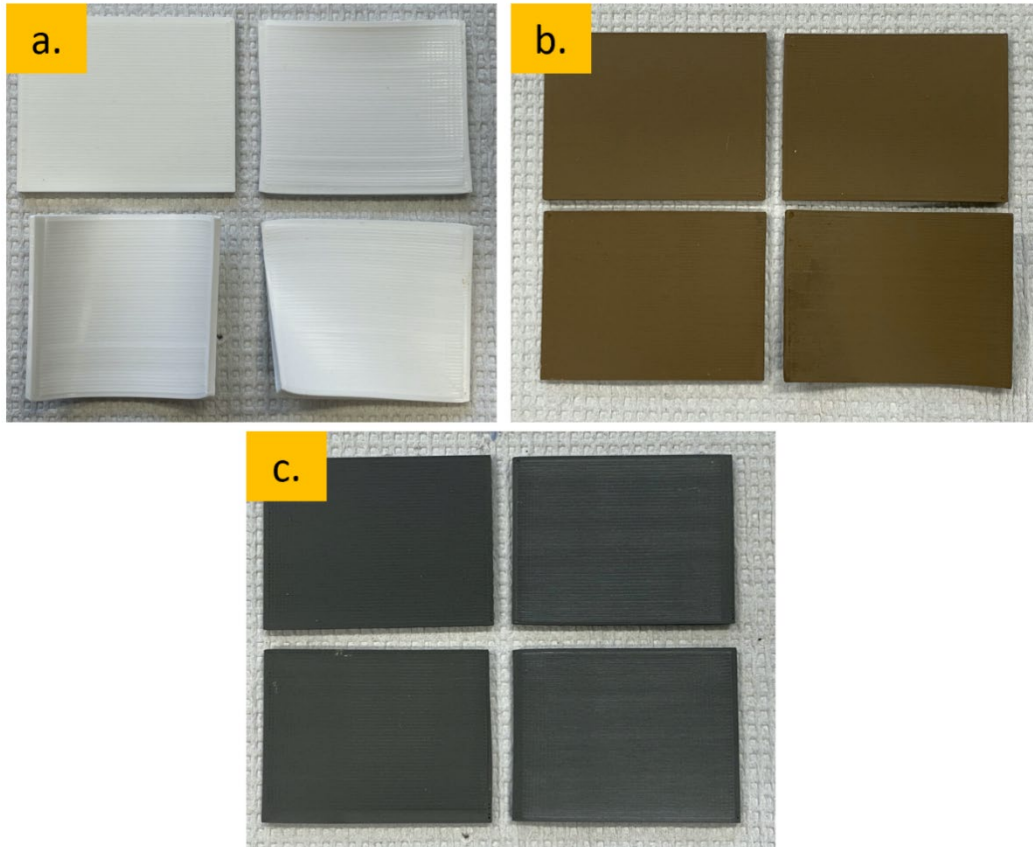


Figure 54. Specimens subjected to 200 hours accelerated weathering. Control sample is the upper left image in each figure: (a) Neat PLA, (b) Bronze PLA, (c) Stainless steel PLA.

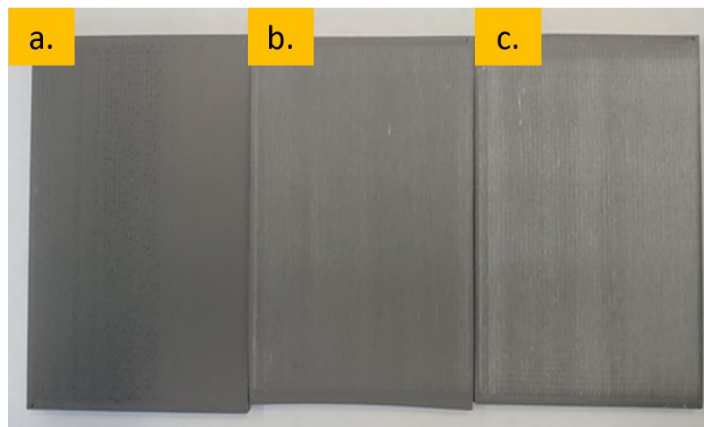


Figure 55. Visual comparison of white chalky surface on stainless steel PLA samples at different stages of accelerated weathering: (a) control, (b) 200 hours and (c) 500 hours.

1. Optical Imaging

Optical microscopy was used to analyze the samples to investigate a chalky white appearance on the stainless steel reinforced samples. It was first suspected that this could be due to moisture exposure of the stainless steel reinforcements during the accelerated weathering test. However, as seen in Figure 56, it appears that the stainless steel particles were not affected but rather the PLA substrate. In the bronze PLA composite samples, there is no appreciable difference between the control sample and the 200-hour sample. It is unknown why the bronze PLA substrate did not undergo the same visible changes.

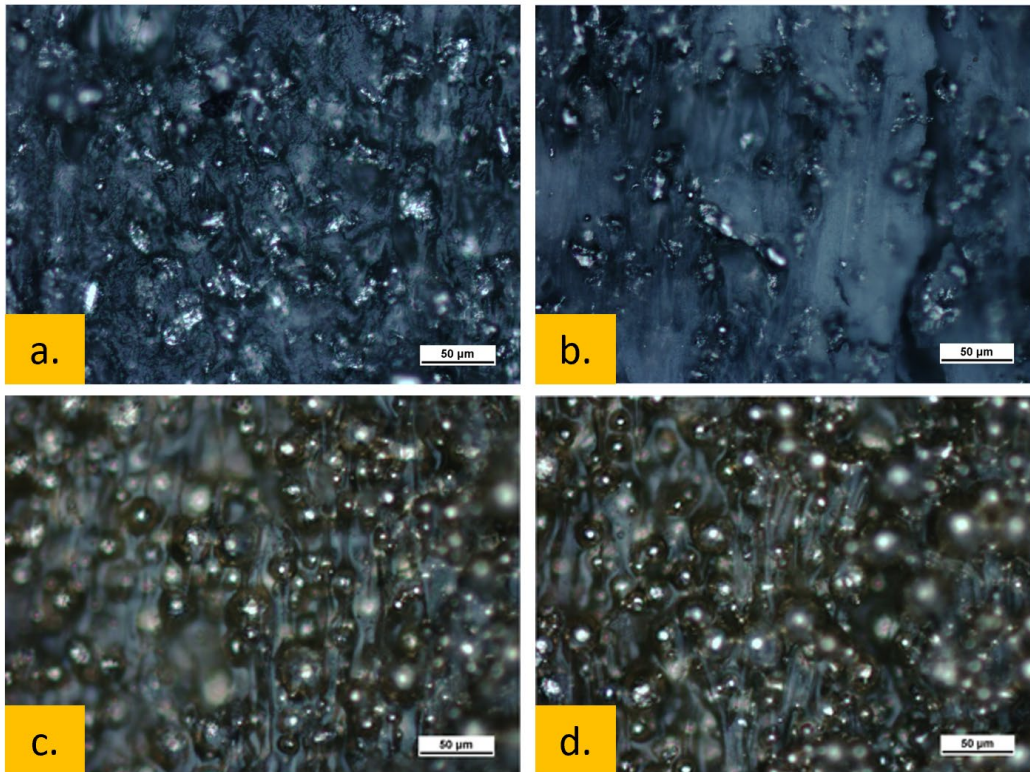


Figure 56. Stainless steel reinforced PLA surface of control (a) and after 200 hours (b). Bronze reinforced PLA control (c) and after 200 hours (d). Optical images were taken at 20x magnification.

2. XRD

X-ray diffraction was also utilized to observe if the accelerated weathering testing caused any changes in the crystallinity of the materials or if corrosion byproducts were

present. For each material tested, bulk sections were removed from the control, a sample that was exposed for 200 hours, and a sample exposed for 500 hours. These sections were individually mounted on Rigaku 24mm open trays (Figure 57).



Figure 57. PLA specimen mounted in 24mm open tray and Rigaku Miniflex 600 XRD (inset)

Initial XRD data for the controls, seen in Figure 58, showed the neat-PLA with a broad curve, typical of an amorphous polymer. However, some crystalline peaks were also present, which are inherent to the various structural phases within neat-PLA, which is semi-crystalline by nature [27]. The predominant peaks observed in the stainless-steel PLA data correlated well with existing XRD data for stainless steel (Iron and Chromium). The principal peaks in the initial bronze PLA data also correlated well with current XRD data for bronze (Copper and Tin). In both stainless steel and bronze, the amorphous curve inherent to neat-PLA is generally suppressed due to the intensity of the metallic reinforcements present in those polymer matrices.

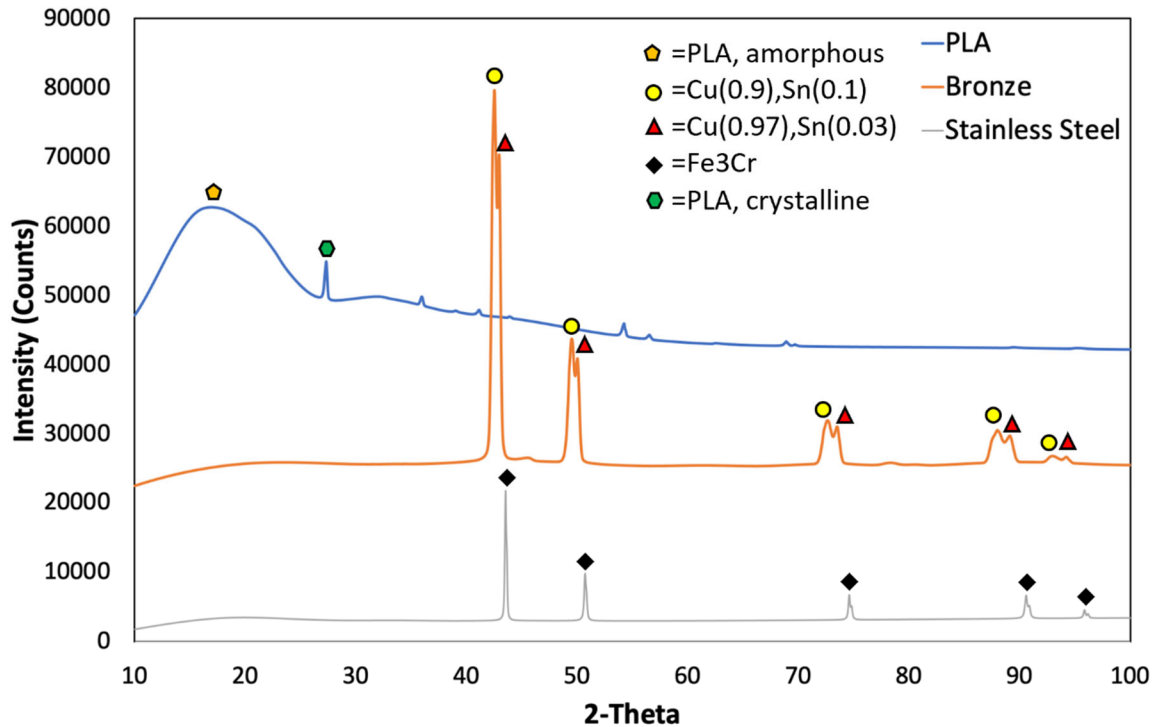


Figure 58. XRD data overlay for control samples.

Following 500 hours of exposure, the samples were re-examined with the XRD. The data for these samples, seen in Figure 59, shows the addition of crystalline peaks correlating to 2θ 's of approximately 16.3 and 18.6 degrees. The presence of these peaks is significantly larger in the neat-PLA. Crystallinity in the PLA is formed by the hydrolytic degradation and cleavage of polymer chains caused by UV and humidity exposure. This phenomenon occurs preferentially in the amorphous region of PLA, which is why the intensity is more significant in the neat-PLA versus the other PLA polymers with metallic reinforcements in their polymer matrices [28].

Based on similar XRD results indicating crystallization of the PLA substrate in both composite samples, it would follow a logic that the bronze reinforced PLA would exhibit similar results as seen in the stainless steel specimen discussed above. The white, powder-like substance is not a powder at all but rather a coloration byproduct of the crystallization of the PLA due to the hydrolytic degradation of the polymer chains [29]. Upon further research, it was found that the presence of transitional metals increases the rate of PLA

photooxidation [9]. It is suspected that while the significant constituent of bronze is the transitional metal Cu, the presence of Sn may offset the effect of transitional metal presence on PLA photodegradation.

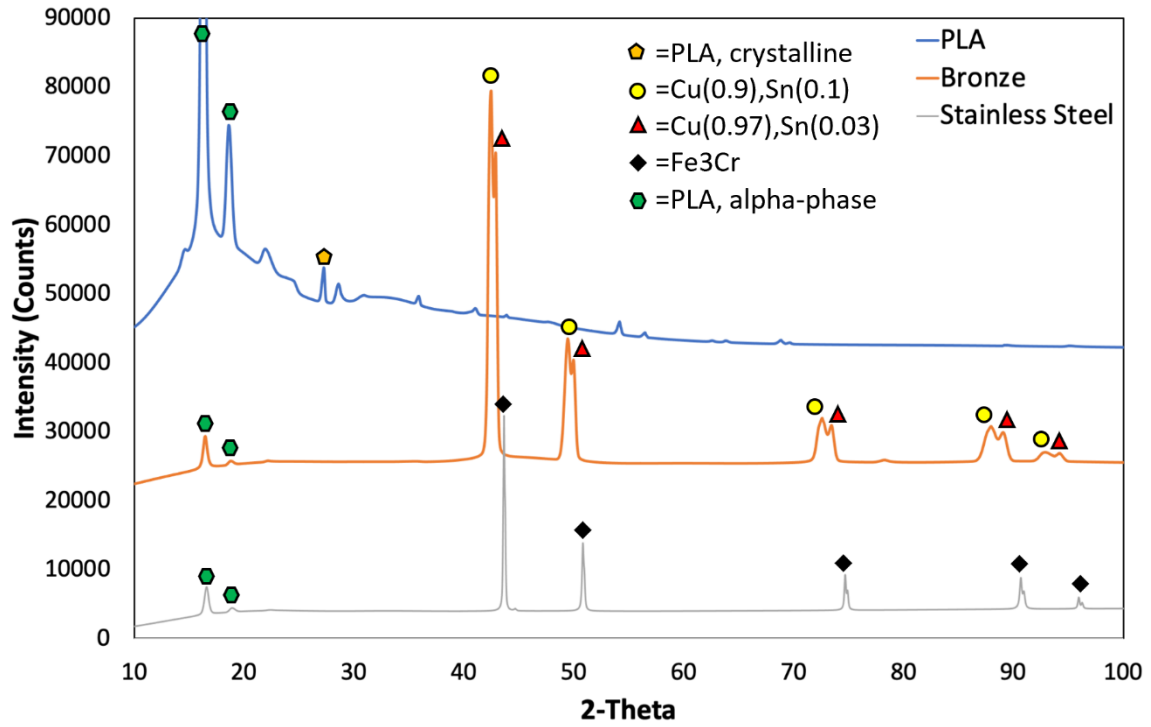


Figure 59. XRD data for 500-hour samples.

IV. CONCLUSIONS

This study delved into the applicability of 3D printed metallic composite materials in load-bearing applications. A detailed literary review was conducted in order to obtain a baseline knowledge of the state-of-the-art in the study of 3DP composites. This literary review was also helpful in guiding the direction of this study. It was found that the study of the mechanical characteristics of 3DP composites and, more specifically, bronze and stainless steel reinforced PLA is in the earliest stages of research.

Many user-defined parameters can be modified when 3D printing a part. Three areas were focused on for this research: infill pattern, layer height, and build direction. Collectively, 120 samples were tested in compression and 20 in tension. For each material, four infill patterns were studied in compression and two in tension. Layer heights of 0.1mm and 0.2mm were tested in compression, while only 0.1mm was tested in tension. Compression samples consisted of flat and vertical build directions. Under tension, only the flat build direction was considered. The results showed that there is no perfect answer for the best recipe in regard to the variables studied. Depending on the intended application and associated loading, careful consideration must be taken in both material selection and print parameters. For example, under tension, stainless steel had a high UTS at the expense of low ductility; however, the material had good strength and ductility in compression.

The theoretical elastic modulus was calculated based upon the particle concentration of each composite. The known elastic modulus values for each material were used in the Halpin-Tsai and Rule of Mixtures models to calculate the overall theoretical values of the composite. Optical microscope images were processed with ImageJ to determine the concentrations of reinforcement particles and porosity due to voids. Theoretical modulus was compared with measured values found during compression testing with good agreement.

Microstructural analysis was conducted to understand the impact the parameters of interest had on the strength of each material. It was seen that an increase in porosity was directly proportional to and the most significant contributing factor to a decrease in

mechanical characteristics. The porosity consists of voids generally similar in size to the reinforcement particles. It is believed that in cases where porosity increases, it is due to the dislodging of the metallic reinforcement particles. One factor to particle dislodgment is from grinding and polishing during sample preparation. The other way particles are dislodged due to the process of 3D printing. With metallic and PLA composites, there are significant differences in thermal conductivity, meaning that the two materials will transfer heat at different rates and thus thermally expand at different rates. As the material is heated during the initial deposition and re-heated during subsequent passes, cyclic thermal stresses are imposed. This cyclic heating and cooling will weaken the bond between the metallic particle and the surrounding PLA matrix, as SEM imaging shows. This study investigated very small layer heights (0.1mm) approaching the same order of magnitude of the reinforcement particles themselves (0.02-0.05mm). Such small layer heights coupled with the weakened bonds from the thermal stress can cause particles to be pulled out with subsequent passes, leaving voids and increased porosity.

Accelerated weathering testing was conducted to expose the 3DP composites of interest to environments with UV and moisture exposure similar to shipboard applications. It was found that the stainless steel reinforcements provided good resistance to deformation due to UV exposure. XRD analysis was conducted to determine the presence of corrosion products or changes in crystallinity. An increase in PLA crystallinity was noticed due to UV and humidity exposure causing hydrolytic degradation and cleavage of the polymer chains. The stainless steel PLA developed a chalky white appearance that was due not to corrosion but rather PLA photooxidation accelerated by the presence of transitional metals found in stainless steel [9].

V. POTENTIAL DIRECTIONS FOR FUTURE WORK

- This study focused solely on static load testing in compression and tension. However, dynamic load testing such as wear testing, impact testing, fatigue testing would provide valuable data for deciding on the application of composites for real-world applications.
- Synthesize filaments of different particle sizes and concentrations to investigate the impact on mechanical characteristics.
- Study composites comprised of different types of particles such as ceramics or nano-particles. Known advantages such as lightweight, good mechanical properties, and inert nature of ceramics can be used to tailor the overall properties.
- Addressing porosity by using a smaller size nozzle, adjusting the temperature, or other novel ideas such as microwave treatment could minimize porosity.
- Explore the functional properties such as thermal and electrical conductivity for use in damage sensing applications. Conductive materials can be candidates for structural health monitoring and non-destructive testing.
- Conduct follow-on accelerated weathering testing to determine the impact of UV and moisture exposure poses on mechanical characteristics.
- Create real-world parts for testing and compare with already used materials. Printing lightweight composite materials with complex geometries on the spot would be beneficial in maintaining mission readiness. Potential applications include heat exchanger parts, propellers, and airfoils for UAVs.

THIS PAGE INTENTIONALLY LEFT BLANK

LIST OF REFERENCES

- [1] J. R. C. Dizon, A. H. Espera, Q. Chen, and R. C. Advincula, “Mechanical characterization of 3D-printed polymers,” *Additive Manufacturing*, vol. 20, pp. 44–67, Mar. 2018, doi: [10.1016/j.addma.2017.12.002](https://doi.org/10.1016/j.addma.2017.12.002).
- [2] K. R. Balasubramanian and V. Senthilkumar, Eds., *Additive Manufacturing Applications for Metals and Composites*: IGI Global, 2020.
- [3] C. Hohimer, J. Christ, N. Aliheidari, C. Mo, and A. Ameli, “3D printed thermoplastic polyurethane with isotropic material properties,” in *Behavior and Mechanics of Multifunctional Materials and Composites 2017*, Apr. 2017, vol. 10165, p. 1016511, doi: [10.1117/12.2259810](https://doi.org/10.1117/12.2259810).
- [4] J. Torres, M. Cole, A. Owji, Z. DeMastry, and A. P. Gordon, “An approach for mechanical property optimization of fused deposition modeling with polylactic acid via design of experiments,” *Rapid Prototyping Journal*, vol. 22, no. 2, pp. 387–404, Jan. 2016, doi: [10.1108/RPJ-07-2014-0083](https://doi.org/10.1108/RPJ-07-2014-0083).
- [5] S. S. Crump, “Apparatus and Method for Creating Three-Dimensional Objects,” U.S. Patent 5121329, Jun. 9, 1992
- [6] A. Lanzotti, M. Grasso, G. Staiano, and M. Martorelli, “The impact of process parameters on mechanical properties of parts fabricated in PLA with an open-source 3-D printer,” *Rapid prototyping journal*, vol. 21, no. 5, pp. 604–617, 2015, doi: [10.1108/RPJ-09-2014-0135](https://doi.org/10.1108/RPJ-09-2014-0135).
- [7] V. Mazzanti, L. Malagutti, and F. Mollica, “FDM 3D printing of polymers containing natural fillers: A review of their mechanical properties,” *Polymers*, vol. 11, no. 7, Art. no. 7, Jul. 2019, doi: [10.3390/polym11071094](https://doi.org/10.3390/polym11071094).
- [8] “FDM vs SLA 3D Printing Technology: A Direct Comparison Guide.” Accessed Mar. 28, 2021. [Online.] Available: <https://apm-designs.com/fdm-vs-sla-3d-printer-tech-comparison/>.
- [9] S. Bocchini, K. Fukushima, A. D. Blasio, A. Fina, A. Frache, and F. Geobaldo, “Polylactic acid and polylactic acid-based nanocomposite photooxidation,” *Biomacromolecules*, vol. 11, no. 11, pp. 2919–2926, Nov. 2010, doi: [10.1021/bm1006773](https://doi.org/10.1021/bm1006773).
- [10] N. Elmrabet and P. Siegkas, “Dimensional considerations on the mechanical properties of 3D printed polymer parts,” *Polymer Testing*, vol. 90, p. 106656, Oct. 2020, doi: [10.1016/j.polymertesting.2020.106656](https://doi.org/10.1016/j.polymertesting.2020.106656).

- [11] J. Bustillos, D. Montero, P. Nautiyal, A. Loganathan, B. Boesl, and A. Agarwal, “Integration of graphene in poly(lactic) acid by 3D printing to develop creep and wear-resistant hierarchical nanocomposites,” *Polym. Compos.*, vol. 39, no. 11, pp. 3877–3888, Nov. 2018, doi: [10.1002/pc.24422](https://doi.org/10.1002/pc.24422).
- [12] D. Jiang and F. Ning, “Fused filament fabrication of biodegradable PLA/316L composite scaffolds: Effects of metal particle content,” *Procedia Manufacturing*, vol. 48, pp. 755–762, Jan. 2020, doi: [10.1016/j.promfg.2020.05.110](https://doi.org/10.1016/j.promfg.2020.05.110).
- [13] “LulzBot Mini,” *LulzBot*, 13-Jan-2021. [Online]. Available: <https://www.lulzbot.com/store/printers/lulzbot-mini#&gid=2&pid=2>. [Accessed: 05-May-2021].
- [14] *Standard Test Method for Compressive Properties of Rigid Plastics*. ASTM Standard D695, 2010.
- [15] *Standard Test Method for Tensile Properties of Plastics*. ASTM Standard D638, 2014.
- [16] B. Rankouhi, S. Javadpour, F. Delfanian, and T. Letcher, “Failure analysis and mechanical characterization of 3D printed ABS with respect to layer thickness and orientation,” *Journal of Failure Analysis and Prevention*, vol. 16, no. 3, pp. 467–481, Jun. 2016, doi: <http://dx.doi.org.libproxy.nps.edu/10.1007/s11668-016-0113-2>.
- [17] *Standard Practice for Operating Fluorescent Ultraviolet (UV) Lamp Apparatus for Exposure of Nonmetallic Materials*. ASTM Standard G154, 2016.
- [18] B.D. Cullity and S.R. Stock, *Elements of X-Ray Diffraction*, 3rd ed. Harlow, Essex, United Kingdom: Pearson Education Limited, 2014.
- [19] “The applications and practical uses of scanning electron microscopes,” *ATA Scientific*, Aug. 01, 2019. <https://www.atascientific.com.au/sem-imaging-applications-practical-uses-scanning-electron-microscopes/> [accessed May 05, 2021].
- [20] S. Ebnesajjad and C. Ebnesajjad, *Surface Treatment of Materials for Adhesive Bonding*. Norwich, UNITED STATES: Elsevier Science & Technology Books, 2013.
- [21] R. E. Smallman and A. W. Ngan, *Modern Physical Metallurgy*, 8th ed. Amsterdam: Elsevier Science & Technology, 2014. [Online]. Available: <https://www-sciencedirect-com.libproxy.nps.edu/topics/engineering/oliver-pharr-method>. [Accessed: 02-May-2021].

- [22] S. Y. Lee, E.-W. Huang, W. Woo, C. Yoon, H. Chae, and S.-G. Yoon, “Dynamic strain evolution around a crack tip under steady-and overloaded-fatigue conditions,” *Metals - Open Access Metallurgy Journal*, vol. 2015, pp. 2109–2118, Nov. 2015, doi: [10.3390/met5042109](https://doi.org/10.3390/met5042109).
- [23] S. Farah, D. G. Anderson, and R. Langer, “Physical and mechanical properties of PLA, and their functions in widespread applications—A comprehensive review,” *Advanced Drug Delivery Reviews*, vol. 107, pp. 367–392, Dec. 2016, doi: [10.1016/j.addr.2016.06.012](https://doi.org/10.1016/j.addr.2016.06.012).
- [24] “Bearing Bronze – (UNS C93200),” *AZoM.com*, Jul. 31, 2012. Accessed May 06, 2021. [Online]. Available: <https://www.azom.com/article.aspx?ArticleID=6294>.
- [25] Z. Luo, X. Li, J. Shang, H. Zhu, and D. Fang, “Modified rule of mixtures and Halpin–Tsai model for prediction of tensile strength of micron-sized reinforced composites and Young’s modulus of multiscale reinforced composites for direct extrusion fabrication,” *Advances in Mechanical Engineering*, vol. 10, no. 7, p. 1687814018785286, Jul. 2018, doi: [10.1177/1687814018785286](https://doi.org/10.1177/1687814018785286).
- [26] “Stainless Steel - Grade 316L - Properties, Fabrication and Applications (UNS S31603),” *AZoM.com*, Feb. 18, 2004. <https://www.azom.com/article.aspx?ArticleID=2382> (accessed May 06, 2021).
- [27] K. Wasanasuk and K. Tashiro, “Crystal structure and disorder in Poly(l-lactic acid) δ form (α' form) and the phase transition mechanism to the ordered α form,” *Polymer*, vol. 52, no. 26, pp. 6097–6109, Dec. 2011, doi: [10.1016/j.polymer.2011.10.046](https://doi.org/10.1016/j.polymer.2011.10.046)
- [28] M. A. Elsayy, K.-H. Kim, J.-W. Park, and A. Deep, “Hydrolytic degradation of polylactic acid (PLA) and its composites,” *Renewable and Sustainable Energy Reviews*, vol. 79, pp. 1346–1352, Nov. 2017, doi: [10.1016/j.rser.2017.05.143](https://doi.org/10.1016/j.rser.2017.05.143).
- [29] M. Ahmad Sawpan, M. R. Islam, M. D. H. Beg, and K. Pickering, “Effect of accelerated weathering on physico-mechanical properties of polylactide bio-composites,” *J Polym Environ*, vol. 27, no. 5, pp. 942–955, May 2019, doi: [10.1007/s10924-019-01405-2](https://doi.org/10.1007/s10924-019-01405-2).

THIS PAGE INTENTIONALLY LEFT BLANK

INITIAL DISTRIBUTION LIST

1. Defense Technical Information Center
Ft. Belvoir, Virginia
2. Dudley Knox Library
Naval Postgraduate School
Monterey, California